https://theses.gla.ac.uk/

Theses Digitisation:

https://www.gla.ac.uk/myglasgow/research/enlighten/theses/digitisation/

This is a digitised version of the original print thesis.

Copyright and moral rights for this work are retained by the author

A copy can be downloaded for personal non-commercial research or study, without prior permission or charge

This work cannot be reproduced or quoted extensively from without first obtaining permission in writing from the author

The content must not be changed in any way or sold commercially in any format or medium without the formal permission of the author

When referring to this work, full bibliographic details including the author, title, awarding institution and date of the thesis must be given

Enlighten: Theses
https://theses.gla.ac.uk/
research-enlighten@glasgow.ac.uk

NUMERICAL SIMULATION OF 3D HYPERSONIC FLOW USING HIGH RESOLUTION SCHEMES

ZHI JIAN WANG, B.Sc.

A thesis submitted to the Faculty of Engineering,

the University of Glasgow for the degree of Doctor of Philosophy

July 1990

© Z.J. WANG, 1990

ProQuest Number: 10983547

All rights reserved

INFORMATION TO ALL USERS
The quality of this reproduction is dependent upon the quality of the copy submitted.

In the unlikely event that the author did not send a complete manuscript
and there are missing pages, these will be noted. Also, if material had to be removed,
a note will indicate the deletion.

ProQuest 10983547

Published by ProQuest LLC (2018). Copyright of the Dissertation is held by the Author.

All rights reserved.
This work is protected against unauthorized copying under Title 17, United States Code
Microform Edition © ProQuest LLC.

ProQuest LLC.
789 East Eisenhower Parkway
P.O. Box 1346
Ann Arbor, MI 48106 – 1346

ACKNOWLEDGEMENTS

The author wishes to express his sincere gratitude to his supervisor, Professor Bryan E. Richards, for his guidance in this research and especially for his help in the writing of this thesis.

The author would like to thank Professor Henry Y. Wong for his help in many aspects , Dr. Jiang Dachun, Dr. Qin Ning and Mr. Shu Chang for their inspiring discussions and encouragement in the period of this research. Thanks are also due to the staff of Glasgow University Computing Centre, especially to Mr. Paul Rosenberg, for their fruitful service, to Miss Margaret Simpson, secretary of the department, for her effective help.

The author is indebted to many friends in Glasgow. Especially the author would like to express his appreciation to Z. Li, W. Qian, C. Hu, X. Chen, J. Cheng and Bob, Rhona, Betty who have either helped him in the research or made the life easier.

The author gratefully acknowledges the support by the SBFSS.

Finally, the author is grateful to his wife for her understanding and support, to his family for their encouragement during this period.

The work included in Chapter 3 has been submitted to and accepted by the Journal of Computational Physics for publication. Part of it has been published in the Proceedings of the International Conference on Numerical Methods in Engineering: Theory and Applications, Swansea, 1990. Part of the work in Chapter 5 has been published in the Proceedings, Workshop on Hypersonic Flows for Reentry Problems, Antibes, 1990.

CONTENTS

CHAPTER 4

AN EFFICIENT EXPLICIT SCHEME

FOR MULTI-DIMENSIONAL STEADY FLOW CALCULATION

SUMMARY

The theme of this research is to simulate laminar three-dimensional hypersonic flow by an appropriate numerical procedure. Naturally two main topics are covered: 1) the development and evaluation of the numerical algorithms, and 2) the simulation of the associated flow and the presentation of the numerical results.

The recently emerging high resolution Total Variation Diminishing (TVD) schemes are chosen to serve that purpose. The Osher-Chakravarthy and Yee TVD are particularly prominent in steady-state calculations. These schemes have an excellent shock-capturing ability when used to solve inviscid flow problems. However, it is still unclear whether they retain their high resolution properties for predicting viscous shear layers. Therefore detailed investigation has been conducted to evaluate their capacities to resolve shear layers and boundary layers occurring in viscous flow at high Reynolds number. During the study, it has been found, through both numerical analysis and experiment, that the Osher-Chakravarthy scheme possesses much lower numerical dissipation than the Yee scheme and thus is favoured in the simulation of viscous flows. Remedies to reduce numerical dissipation for the Yee scheme have been suggested. Excellent results have been obtained using the modified schemes.

Confidence gained with these high resolution schemes has led to their applications in the simulation of three-dimensional hypersonic flow. The resultant code has been tested on two simple cases, one inviscid and one viscous. Excellent agreement with the well-documented nume-

rical results has been found. Then the code is employed to solve a hypersonic flow around a double ellipsoid at a high angle of attack representing the forebody of a space vehicle including a canopy. Experimentation on this case has been carried out to validate results of numerical analysts. There are found excellent agreements between numerical and experimental results on almost every aspect including the Stanton number in the separation domain on the leeside direction. This case has fully demonstrated how successful a numerical simulation can be.

In parallel to the work stated above, much effort has been devoted to numerical flow visualization techniques which constitute an extremely important ingredient in the simulation of three-dimensional flow. Numerical algorithms are discussed on the plot of iso-contours and the tracking of the streamlines or the oil-flow pattern on a body surface. These techniques have been successfully used to display the numerically-simulated flow pictures.

In the applications of the high resolution schemes to the simulation of three-dimensional flow, it has been found they are still quite time-consuming. Therefore, an effort has been made to seek more efficient schemes which have almost the same level of resolution. This effort has resulted in the so-called X scheme developed by the author. A different grid pattern is employed to build up the X scheme so that it can be four times as fast as the conventional scheme while maintaining the some accuracy. The scheme has been tested on several cases. It has shown great promise for wider applications.

CHAPTER 1

INTRODUCTION

1.1 Demands of Three-Dimensional Hypersonic Flow Simulation

In recent years the understanding of flows at high Mach numbers and large angles of attack, occurring during the atmospheric reentry of spacecraft, has regained considerable attention because of the development of new space vehicles and planning of future supersonic and hypersonic airplanes [2,13]. The extreme physical conditions during this critical phase are prohibitively difficult to realize in wind tunnel experiments if at all possible, because of the rarefied atmosphere, the very high temperatures, and possible chemical reactions. If some relatively feasible experiments can be done, they tend to be very costly. Numerical simulation of the associated flow, therefore, will play a major role in the process of the project validation leaving experiments mainly to serve as a validation procedure for numerical methods.

In order to model realistic and hence very complex flow conditions, the solution of the full three-dimensional fluid motion is demanded. This is due to the fact that many fluid dynamic phenomena such as cross flow separation and cross flow shock waves etc. can only be resolved by such a solution. With the increased capacities of the present supercomputers and the development of more robust and more efficient numerical algorithms, this has become entirely feasible. In fact, some usefully accurate three-dimensional hypersonic viscous flow simulations have emerged in the literature [26,27]. However, they all demonstrated deficiencies in one respect or another. For example, some are too expensive

to be used routinely, and some others are not sufficiently robust to tackle difficult flow problems. Because of that, much research effort is directed towards seeking of even more efficient and/or more accurate numerical techniques. This effort will advance the knowledge of even more complicated flow phenomena.

1.2 Challenges Provided by This Task

The numerical simulation of three-dimensional hypersonic flow is a considerable challenge for a variety of reasons. In addition to the well known difficulties associated with the determination of transition and with the modelling of turbulence in compressible flows at high Reynolds number, problems are encountered associated with the special features of hypersonic aerodynamics, which are discussed in detail as follows:

a. The effect of high Mach number

The most striking difference between flow at subsonic and supersonic speeds is the formation of a shock wave ahead of vehicle shapes. The strength of the shock is decided by the free stream Mach number and the angle between the vehicle and the free stream direction. The flow behind the shock is usually a mixture of subsonic and supersonic fluids. There are large differences in the entropy rise of the fluid crossing the shock at different angles. This results in the generation of the so-called entropy layer, which plays an important part in determining the flow field.

The numerical modelling of the shock wave has been one of the most

difficult problems encountered during the development of CFD. In theory, a shock is a discontinuity existing in the solution. In practice, it is either fitted by applying the Rankine-Hugoniot conditions or is captured as a steep gradient by adding numerical dissipation. Because of the difficulty in applying the shock-fitting technique to some complex flow situations, the shock-capturing procedure has gained favour in the CFD community during the past few years. Research in high-resolution shock capturing schemes [8,10,16,17,46-49] has attracted considerable attention. So far many excellent results have been achieved. On the other hand, the quality of the resolution of shock waves comes at a comparatively high cost because of the quite complicated features of the high resolution schemes used. Hence, research into more efficient schemes while maintaining their high accuracy is still under way.

b. Real gas effects

At the high temperatures which exist behind the shock for hypersonic flight, the temperature energy of the gas becomes comparable with the energies associated with various molecular and atomic processes, such as excitation of the vibrational modes of the molecules, dissociation and ionisation. Under these conditions the gas no longer behaves as a perfect gas having a constant value of the ratio of specific heats, and the energy which is involved in these processes must be taken into account when calculating the flow field.

As a first stage of the modelling of real gas effects, many approaches are based on the use of a small constant value of γ (the ratio of specific heats). This is an approximation for real gas effects which

can hold for a wide range of hypersonic flight conditions. More accurate simulations require more accurate physical models to be built up.

c. Non-equilibrium effects

Thus far in the discussion of real gas effects, the assumption has been made that the gas is in thermodynamic equilibrium at all points in the flow field. However, the transfer of energy to vibration models, and the process of dissociation and ionisation, together with the recombination which occurs in regions where the temperature is falling all require a finite time, the so-called "relaxation time", before equilibrium is reached. If the rate processes are happening very rapidly, there may not be time for thermodynamic equilibrium to be established. These processes will cause the non-equilibrium effects.

Numerical simulation of non-equilibrium flows has been explored recently. Generally speaking, it suffers from the lack of availability of accurate physical models. Much work is to be done on this aspect rather than the relevant numerical methods.

d. Viscous effects

At high Mach numbers very high temperatures will be developed in regions where flow is decelerated, such as in boundary layers close to surfaces. Very steep changes are thus expected in the temperature profile, resulting in very strong kinetic heating processes within the viscous layer. Separation effects, too, may become important in hypersonic flows, because of the prevalence of thick laminar boundary layers which

do not readily withstand adverse pressure gradients.

The successful simulation of a hypersonic flow is largely decided by the accuracy of the simulated heat transfer rate on the surfaces since the heating process is the key interest of aerodynamic designers. This requirement demands accurate resolution of the viscous layers, another one of the most difficult problems in CFD. In a viscous flow simulation, the approach hinges on the control of the numerical dissipation which is required to stabilize the numerical scheme. In principle, numerical dissipation should be well below the physical dissipation for a successful simulation to be carried out. However, the complexity and the nonlinearity of the employed mathematical models make it impossible to accurately analyze the embedded numerical dissipation. Hence the accurate solution of the viscous boundary layer is still far from complete.

e. Rarefied gas effects

At normal altitudes and velocities the air flowing past a vehicles can be treated as if it were continuum. At high altitudes, the air becomes less dense, and the motion of the individual gas particles becomes important. The parameter which determines the onset of rarefied gas effects is the Knudsen number, Kn, which is the ratio of the mean free path to a typical body dimension. The continuum flow model starts to break down when Kn is of the order unity.

The governing equations to be solved for rarefied gas flow are the Boltzmann equations. The problem is out of the range of this research. It will not be considered further.

1.3 Overview of Numerical Methods for High Speed Flow Simulations

As pointed out in the last section, one of the most distinguishing features of a high speed flow is the strong shock wave, which represents a discontinuity in the solution. Since the very early days of the appearance of CFD, great effort has been devoted to the numerical simulation of discontinuities. A brief survey on shock-modelling techniques is now given.

The first natural idea to model a shock wave is to treat the shock as an internal boundary of discontinuity. The evolution of the shock wave is governed by the Rankine-Hugoniot conditions. The technique embracing these conditions is called the shocking fitting method (e.g. [22]). The advantage of shock-fitting is obvious. It gives an accurate resolution of the discontinuity. The difficulty is that the structure of the discontinuities and their interaction must be known or easily anticipated. Special sensors must track each discontinuity and the programming logic becomes complicated.

Another possibility is to abandon the exact resolution of the shock wave and to allow the discontinuity to develop as a continuous steep gradient in the solution. This shock capturing idea is now the most common in engineering practice. The method is simple to program since a formula with the same structure is used over all the computational domain. No knowledge of the type and location of the discontinuity is needed.

A practical shock-capturing scheme should satisfy three criteria.

First, the scheme should be dissipative. For some non-dissipative numerical schemes, artificial viscosity should be introduced. Second, the scheme should be in conservation form. This is a necessary condition for correct positioning and strength assessment of the shock wave. Third, the scheme should satisfy an entropy condition to ensure the captured shock to be the physically relevant one.

The shock-capturing schemes can be divided into two main categories — according to space differencing — central difference and upwind schemes. Examples of central difference schemes are the Lax-Wendroff, MacCormack [21], Beam-Warming [3] schemes and the Jameson centered multi-stage Runge-Kutta method [19], etc. The central difference schemes all suffer from a lack of dissipation. Therefore, the success of these schemes depends largely on the detailed construction of the model for artificial viscosity. The amount of viscosity added to the scheme is usually problem-dependent, thus tending to make the scheme non-universal. On the other hand, upwind schemes follow the characteristic direction of the wavefield and reflect the physical interaction of the waves in the flow. They are essentially dissipative. These schemes include the Godunov scheme [14] which has been extended to second order accuracy by van Leer [39], the Boris and Book Flux-Corrected Transport method [4,5], the Steger-Warming [32] and van Leer [40] flux vector splitting, the Osher [24] and Roe [28] flux difference splitting and the high-resolution Total Variation Diminishing (TVD) [16] and Essentially Non-Oscillatory (ENO) schemes [11,17]. In the past decade, these schemes have achieved great success in the modelling of shock waves. Particularly the TVD and ENO schemes represent the state-of-the-art techniques for the modelling of discontinuous problems of the hyperbonic conservation

laws.

1.4 The Scope of This Study

The current research represents the first step towards the accurate simulation of three-dimensional hypersonic flow. Because of that, the flow simulation is based on the following assumptions:

a. The flow is thermally and calorically perfect without any chemical reactions. As mentioned earlier, accurate universal models accounting for the real gas effects are yet to be found. Furthermore, a perfect gas assumption will allow the numerical results to be readily compared with the well-documented experimental data so that the numerical technique can be easily validated.

b. The flow is in the continuum regime. The reason for this are two fold. First, hypersonic flight occurs mostly in this regime. Secondly, rarefied gas flow simulation leads to a different problem from the one the author is interested in, i.e., the solution of the Navier-Stokes equations.

c. The flow is laminar. It was estimated that accurate simulation of turbulence is beyond the reach of modern supercomputers, while the solution of the Reynolds averaged Navier-Stokes equations is largely restricted by the quality of turbulence models available.

The success of such a flow simulation lies in the accurate information of both pressure loading and particularly kinetic heating on body

surfaces. This again necessitates the high resolution of the strong shock wave and the viscous boundary layer — two key features of hypersonic flows. Both are concerned with very steep changes in the flow variables. It is well known that the associated numerical scheme plays the most important role in the whole simulation. Its accuracy, efficiency and robustness greatly affect the quality of the solution. Because of that, considerable attention is paid to the evaluation of the numerical algorithms.

The successful application of the high-resolution TVD schemes in the solution of supersonic inviscid flow [34,42] tempted many people to use them directly to the solution of the Navier-Stokes equations. Although some good results are achieved, it has been found that the dissipation pattern within each TVD scheme is quite different [43,44]. Blind applications of TVD schemes to solutions of viscous flow can cause unrepresentative results. In some cases, the dissipation embedded in a TVD scheme may be more than required to resolve the boundary layer and may overwhelm the physical dissipation. This phenomenon is studied and a new approach is suggested which has been proven to be superior to the original technique. Confidence gained in the numerical schemes has resulted in their applications to three-dimensional flow simulations. It is, however, found that they are still too costly to be put into routine calculations. The work has therefore started to search for more efficient numerical schemes while not compromising their robustness and accuracy. This work has resulted in the new high-order X scheme developed by the author. The X scheme is far more efficient than TVD schemes. It also demonstrated very good resolution for shock waves. Further work is to be done to extend its application to hypersonic flow

simulation though it has already shown great promise.

1.5 Layout of the Thesis

The main topics of this research are the development of robust, accurate and efficient numerical algorithms and the simulation of three-dimensional hypersonic flows. Accordingly, the thesis is naturally divided into six chapters. In Chapter 1, we have already given a brief introduction to this study. The mathematical models of fluid motion are discussed in Chapter 2. Then detailed investigation into the discretization of hyperbolic conservation laws is conducted in Chapter 3, and Chapter 4 is devoted to an efficient explicit scheme for multi-dimensional flow problems. Later the simulation of hypersonic flows and the flow visualization techniques are presented in Chapter 5. Finally, conclusions from the research and recommendations to future work are given in Chapter 6.

CHAPTER 2

MATHEMATICAL MODELS OF FLUID MOTION

2.1 Formulation of Conservation Laws in Integral Form

The movement of matter in nature is governed by three universal principles, which are conservation of mass, conservation of momentum, and conservation of energy. Fluid motion is no exception. Let the position vector **r** of a point and time t be defined with respect to an inertial reference frame represented by the Cartesian coordinates x,y,z. If the flow region is divided into small subregions called cells, the general form of a conservation law for a given cell is then [41]

$$\int_{V(t_2)} H dv = \int_{V(t_1)} H dV - \int_{t_1}^{t_2} \oint_{S(t)} \mathbf{n}\cdot\mathbf{f} dS dt + \int_{t_1}^{t_2} \int_{V(t)} P dV dt \qquad (2.1)$$

where V(t) is the cell volume, **n**dS is a vector element of surface area with outward normal **n**, H is a conservative variable per unit volume, **f** is the flux of H per unit area per unit time, and P is the rate of production of H per unit volume per unit time. The cells are assumed to be fixed in space and time. The conservative variable H can be both scalar and vector. Examples are density ρ, total energy per unit volume E_t, and the momentum per unit volume $\mathbf{m}=\rho\mathbf{v}$. If H is a scalar, then **f** is a vector; while if H is a vector, **f** is a tensor. If we assume all variables are continuous in time, then Eq.(2.1) reduces to

$$\frac{d}{dt}\int_V H dV + \oint_S \mathbf{n}\cdot\mathbf{f} dS = \int_V P dV \qquad (2.2)$$

This is the usual statement of a conservation law. If it is assumed that there is no mass and energy production and there is no body force in the fluid flow (P=0), the following conservation laws can be obtained by substituting the corresponding conservative variables into Eq.(2.2),

$$\frac{d}{dt}\int_V \rho dV+\oint_S \mathbf{n}\cdot\rho\mathbf{v}dS=0 \tag{2.3}$$

$$\frac{d}{dt}\int_V \rho\mathbf{v}dV+\oint_S \mathbf{n}\cdot(\rho\mathbf{v}\mathbf{v}-\Pi)dS=0 \tag{2.4}$$

$$\frac{d}{dt}\int_V E_t dV+\oint_S \mathbf{n}\cdot(E_t\mathbf{v}+\mathbf{q}-\Pi\cdot\mathbf{v})dS=0 \tag{2.5}$$

where Π is a tensor representing the stress subject to the surfaces of the cell, and $\mathbf{q}$ is a vector indicating the rate of heat lost per unit area by conduction through the cell surface. Let u, v, w be the velocities in the x, y, z directions respectively, and if the fluid is Newtonian, the stress takes the form

$$\Pi_{ij}=-p\delta_{ij}+\mu\left(\frac{\partial u_i}{\partial x_j}+\frac{\partial u_j}{\partial x_i}\right)+\mu'\delta_{ij}\frac{\partial u_k}{\partial x_k} \qquad (i,j,k=1,2,3) \tag{2.6}$$

where δ_{ij} is the Kronecker delta function; u_1, u_2, u_3 and x_1, x_2, x_3 stand for u, v, w and x, y, z correspondingly; p is the pressure and μ is the coefficient of viscosity and μ' is the second coefficient of viscosity. Usually, it is assumed that

$$\mu' = -\frac{2}{3}\mu$$

The stress tensor is frequently separated in the following manner

$$\Pi_{ij}=-p\delta_{ij}+\tau_{ij} \tag{2.7}$$

where

$$\tau_{ij}=\mu\left[\left(\frac{\partial u_i}{\partial x_j}+\frac{\partial u_j}{\partial x_i}\right)-\frac{2}{3}\delta_{ij}\frac{\partial u_k}{\partial x_k}\right] \quad (i,j,k=1,2,3) \tag{2.8}$$

Fourier's law for heat transfer by conduction will be assumed so that the heat transfer **q** can be expressed as

$$\mathbf{q}=-k\nabla T \tag{2.9}$$

where k is the coefficient of the thermal conductivity and T is the temperature. Generally speaking, the integral formulation is convenient for finite volume discretisation.

2.2 Formulation of Conservation Laws in Differential Form

The differential formulation is obtained by applying Eq.(2.2) to a differential cell in physical space dxdydz. Let **i**, **j**, **k** be unit vectors in the x,y,z direction respectively. Eq.(2.2) then takes the form

$$\frac{\partial(H dxdydz)}{\partial t}+\frac{\partial(\mathbf{i}\cdot\mathbf{f}dydz)}{\partial x}dx+\frac{\partial(\mathbf{j}\cdot\mathbf{f}dxdz)}{\partial y}dy+\frac{\partial(\mathbf{k}\cdot\mathbf{f}dxdy)}{\partial z}dz=Pdxdydz \tag{2.10}$$

or simplified further (assuming P=0)

$$\frac{\partial H}{\partial t}+\frac{\partial(\mathbf{i}\cdot\mathbf{f})}{\partial x}+\frac{\partial(\mathbf{j}\cdot\mathbf{f})}{\partial y}+\frac{\partial(\mathbf{k}\cdot\mathbf{f})}{\partial z}=0. \tag{2.11}$$

The differential form of the conservation laws of mass, momentum, and energy can then be expressed as

$$\frac{\partial \rho}{\partial t} + \frac{\partial \rho u}{\partial x} + \frac{\partial \rho v}{\partial y} + \frac{\partial \rho w}{\partial z} = 0 \tag{2.12}$$

$$\frac{\partial \rho u}{\partial t} + \frac{\partial}{\partial x}(\rho u^2 + p - \tau_{xx}) + \frac{\partial}{\partial y}(\rho uv - \tau_{xy}) + \frac{\partial}{\partial z}(\rho uw - \tau_{xz}) = 0 \tag{2.13}$$

$$\frac{\partial \rho v}{\partial t} + \frac{\partial}{\partial x}(\rho uv - \tau_{xy}) + \frac{\partial}{\partial y}(\rho v^2 + p - \tau_{yy}) + \frac{\partial}{\partial z}(\rho vw - \tau_{yz}) = 0 \tag{2.14}$$

$$\frac{\partial \rho w}{\partial t} + \frac{\partial}{\partial x}(\rho uw - \tau_{xz}) + \frac{\partial}{\partial y}(\rho wv - \tau_{zy}) + \frac{\partial}{\partial z}(\rho w^2 + p - \tau_{zz}) = 0 \tag{2.15}$$

$$\frac{\partial E_t}{\partial t} + \frac{\partial}{\partial x}(E_t u + pu - u\tau_{xx} - v\tau_{xy} - w\tau_{xz} + q_x) +$$

$$\frac{\partial}{\partial y}(E_t v + pv - u\tau_{xy} - v\tau_{yy} - w\tau_{yz} + q_y) + \frac{\partial}{\partial z}(E_t w + pw - u\tau_{xz} - v\tau_{yz} - w\tau_{zz} + q_z) = 0 \tag{2.16}$$

where the components of the viscous stress are given by Eqs.(2.8). This form of equations is particularly useful for finite difference discretization.

2.3 Equation of State

In order to close the system of fluid dynamic equations it is necessary to establish relationships between the thermodynamic variables (p, ρ, T) as well as to relate the transport properties (μ, k) to the thermodynamic variables. Since a perfect gas assumption is used in this research, we can easily establish the following relations. The perfect gas equation of state is

$$p = \rho RT \tag{2.17}$$

where R is the gas constant. For air at standard conditions,

$R=287 m^2/s^2K$. Also for a perfect gas, the following relationships exist:

$$e=c_v T \quad h=c_p T \quad \gamma=\frac{c_p}{c_v} \quad c_v=\frac{R}{\gamma-1} \quad c_p=\frac{\gamma R}{\gamma-1} \tag{2.18}$$

Here e is the internal energy per unit mass; h is the enthalpy per unit mass; c_v is the specific heat at constant volume; c_p is the specific heat at constant pressure and γ is the ratio of specific heats. Further equations can be derived from Eqs.(2.17)-(2.18). For example

$$p=(\gamma-1)\rho e \quad T=\frac{(\gamma-1)e}{R} \tag{2.19}$$

The coefficients of viscosity and thermal conductivity have been related to the thermodynamic variables using kinetic theory. For example, Sutherland's formula for viscosity is given by

$$\mu=C_1\frac{T^{3/2}}{T+C_2} \tag{2.20}$$

where C_1 and C_2 are constant. For air at moderate temperature, $C_1=1.458\times10^{-6}$ kg/(m s $\sqrt{K}$) and $C_2=110$ K. The Prandtl number

$$Pr=\frac{c_p\mu}{k} \tag{2.21}$$

is a constant (Pr=0.72 assumed) for air at standard conditions. This equation can be used to get the value for k once μ is decided from Eq.(2.20).

2.4 Non-Dimensional Form of Equations

To obtain the flow behavior around bodies of similar shape with minimum computational effort, it is desirable to put the governing equations into nondimensional form. Many nondimensionalizing procedures are available. The following procedure is adopted here

$$x^*=\frac{x}{L} \qquad y^*=\frac{y}{L} \qquad z^*=\frac{z}{L} \qquad t^*=\frac{t}{L/V_\infty}$$

$$u^*=\frac{u}{V_\infty} \qquad v^*=\frac{v}{V_\infty} \qquad w^*=\frac{w}{V_\infty} \qquad \mu^*=\frac{\mu}{\mu_\infty}$$

$$\rho^*=\frac{\rho}{\rho_\infty} \qquad p^*=\frac{p}{\rho_\infty V_\infty^2} \qquad T^*=\frac{T}{T_\infty} \qquad e^*=\frac{e}{V_\infty^2}$$

where the nondimensional variables are denoted by an asterisk, free-stream conditions are denoted by ∞ and L is the reference length used in the Reynolds number

$$Re=\frac{\rho_\infty V_\infty L}{\mu_\infty}$$

If the nondimensionalizing procedure is applied to Eqs.(2.12)-(2.16) and if the equations are given in a vector form, the following nondimensional equations are obtained

$$\frac{\partial \mathbf{U}^*}{\partial t^*}+\frac{\partial \mathbf{E}^*}{\partial x^*}+\frac{\partial \mathbf{F}^*}{\partial y^*}+\frac{\partial \mathbf{G}^*}{\partial z^*}=\frac{\partial \mathbf{E}_v^*}{\partial x^*}+\frac{\partial \mathbf{F}_v^*}{\partial y^*}+\frac{\partial \mathbf{G}_v^*}{\partial z^*} \qquad (2.22)$$

where $\mathbf{U}^*$ is the vector of conservation variables; $\mathbf{E}^*$, $\mathbf{F}^*$ and $\mathbf{G}^*$ are the inviscid flux vectors and $\mathbf{E}_v^*$, $\mathbf{F}_v^*$, $\mathbf{G}_v^*$ are the viscous flux vectors

$$\mathbf{U}^* = \begin{bmatrix} \rho^* \\ \rho^* u^* \\ \rho^* v^* \\ \rho^* w^* \\ E_t^* \end{bmatrix}$$

$$\mathbf{E}^* = \begin{bmatrix} \rho^* u^* \\ \rho^* u^{*2} + p \\ \rho^* u^* v^* \\ \rho^* u^* w^* \\ (E_t^* + p^*) u^* \end{bmatrix} \qquad \mathbf{E}_v^* = \begin{bmatrix} 0 \\ \tau_{xx}^* \\ \tau_{xy}^* \\ \tau_{xz}^* \\ u^* \tau_{xx}^* + v^* \tau_{xy}^* + w^* \tau_{xz}^* - q_x^* \end{bmatrix}$$

$$\mathbf{F}^* = \begin{bmatrix} \rho^* v^* \\ \rho^* u^* v^* \\ \rho^* v^{*2} + p^* \\ \rho^* v^* w^* \\ (E_t^* + p^*) v^* \end{bmatrix} \qquad \mathbf{F}_v^* = \begin{bmatrix} 0 \\ \tau_{xy}^* \\ \tau_{yy}^* \\ \tau_{yz}^* \\ u^* \tau_{xy}^* + v^* \tau_{yy}^* + w^* \tau_{yz}^* - q_y^* \end{bmatrix}$$

$$\mathbf{G}^* = \begin{bmatrix} \rho^* w^* \\ \rho^* u^* w^* \\ \rho^* v^* w \\ \rho^* w^{*2} + p^* \\ (E_t^* + p^*) w^* \end{bmatrix} \qquad \mathbf{G}_v^* = \begin{bmatrix} 0 \\ \tau_{xz}^* \\ \tau_{yz}^* \\ \tau_{zz}^* \\ u^* \tau_{xz}^* + v^* \tau_{yz}^* + w^* \tau_{zz}^* - q_z^* \end{bmatrix}$$

and

$$E_t^* = \rho^* \left[e^* + \frac{u^{*2} + v^{*2} + w^{*2}}{2} \right] \tag{2.23}$$

The components of the shear-stress tensor and the heat-flux vector in nondimensional form are given by

$$\tau_{xx}^* = \frac{2\mu^*}{3Re}\left[2\frac{\partial u^*}{\partial x^*} - \frac{\partial v^*}{\partial y^*} - \frac{\partial w^*}{\partial z^*}\right]$$

$$\tau_{yy}^* = \frac{2\mu^*}{3Re}\left[2\frac{\partial v^*}{\partial y^*} - \frac{\partial u^*}{\partial x^*} - \frac{\partial w^*}{\partial z^*}\right]$$

$$\tau_{zz}^* = \frac{2\mu^*}{3Re}\left[2\frac{\partial w^*}{\partial z^*} - \frac{\partial u^*}{\partial x^*} - \frac{\partial v^*}{\partial y^*}\right]$$

$$\tau_{xy} = \frac{\mu^*}{Re}\left[\frac{\partial u^*}{\partial y^*} + \frac{\partial v^*}{\partial x^*}\right]$$

$$\tau_{xz} = \frac{\mu^*}{Re}\left[\frac{\partial u^*}{\partial z^*} + \frac{\partial w^*}{\partial x^*}\right]$$

$$\tau_{yz} = \frac{\mu^*}{Re}\left[\frac{\partial w^*}{\partial y^*} + \frac{\partial v^*}{\partial z^*}\right]$$

$$q_x^* = \frac{\mu^*}{(\gamma-1)M_\infty^2 \, Re \, Pr}\frac{\partial T^*}{\partial x^*}$$

$$q_y^* = \frac{\mu^*}{(\gamma-1)M_\infty^2 \, Re \, Pr}\frac{\partial T^*}{\partial y^*}$$

$$q_z^* = \frac{\mu^*}{(\gamma-1)M_\infty^2 \, Re \, Pr}\frac{\partial T^*}{\partial z^*}$$

where M_∞ is the freestream Mach number

$$M_\infty = \frac{V_\infty}{\sqrt{\gamma R T_\infty}}$$

and the perfect gas equations of state become

$$p^*=(\gamma-1)\rho^* e^* \tag{2.24a}$$

$$T^*=\frac{\gamma M_\infty^2 p^*}{\rho^*} \tag{2.24b}$$

If Re⇒∞, Eq.(2.22) returns to the Euler equations

$$\frac{\partial U^*}{\partial t^*}+\frac{\partial E^*}{\partial x^*}+\frac{\partial F^*}{\partial y^*}+\frac{\partial G^*}{\partial z^*}=0 \tag{2.25}$$

For convenience, the asterisk will be dropped from the nondimensional equations from now on.

2.5 Generalized Coordinate System

When realistic problems are solved, the geometries concerned are usually very complex. It would be extremely difficult to enforce boundary conditions if the Cartesian coordinate system is used. Therefore a body-fitted grid is highly desired. This kind of grid can be generated by means of an algebraic method or the solution of partial differential equations. Appendix B gives some information on this topic. If it is supposed that the computational space (ξ,η,ζ) has the following unique, single-valued transformation relation with the physical space (x,y,z)

$$\begin{aligned}\xi&=\xi(x,y,z)\\ \eta&=\eta(x,y,z)\\ \zeta&=\zeta(x,y,z)\end{aligned} \tag{2.26}$$

and by implication then

$$J=\frac{\partial(\xi,\eta,\zeta)}{\partial(x,y,z)}=\begin{vmatrix}\xi_x & \xi_y & \xi_z\\ \eta_x & \eta_y & \eta_z\\ \zeta_x & \zeta_y & \zeta_z\end{vmatrix}\neq 0$$

Under this condition, the transformation is able to be inverted, i.e.,

$$\begin{aligned} x&=x(\xi,\eta,\zeta)\\ y&=y(\xi,\eta,\zeta)\\ z&=z(\xi,\eta,\zeta)\end{aligned} \qquad (2.27)$$

and

$$J^{-1}=\frac{\partial(x,y,z)}{\partial(\xi,\eta,\zeta)}=\begin{vmatrix}x_\xi & x_\eta & x_\zeta\\ y_\xi & y_\eta & y_\zeta\\ z_\xi & z_\eta & z_\zeta\end{vmatrix}\neq 0$$

It is much easier to evaluate the Jacobian matrix numerically in the following manner

$$J=1/J^{-1}=1/[x_\xi(y_\eta z_\zeta-y_\zeta z_\eta)-x_\eta(y_\xi z_\zeta-y_\zeta z_\xi)+x_\zeta(y_\xi z_\eta-y_\eta z_\xi)] \qquad (2.28)$$

where

$$x_\xi = [x(i+1,j,k)-x(i-1,j,k)]/2$$

$$x_\eta = [x(i,j+1,k)-x(i,j-1,k)]/2$$

$$x_\zeta = [x(i,j,k+1)-x(i,j,k-1)]/2$$

etc. Here i,j,k denote indices in the ξ, η, ζ direction respectively and $\Delta\xi=\Delta\eta=\Delta\zeta=1$ is implied. Other geometry parameters can be calculated according to the following formulae

$$\xi_x = J(y_\eta z_\zeta - y_\zeta z_\eta)$$

$$\xi_y = J(x_\zeta z_\eta - x_\eta z_\zeta)$$

$$\xi_z = J(x_\eta y_\zeta - x_\zeta y_\eta)$$

$$\eta_x = J(y_\zeta z_\xi - y_\xi z_\zeta)$$

$$\eta_y = J(x_\xi z_\zeta - x_\zeta z_\xi)$$

$$\eta_z = J(x_\zeta y_\xi - x_\xi y_\zeta)$$

$$\zeta_x = J(y_\xi z_\eta - y_\eta z_\xi)$$

$$\zeta_y = J(x_\eta z_\xi - x_\xi z_\eta)$$

$$\zeta_z = J(y_\xi z_\eta - y_\eta z_\xi)$$

If we apply the generalized transformation to the compressible Navier-Stokes equations written in vector form [Eq.(2.22)], the following transformed equation is obtained

$$\frac{\partial \bar{U}}{\partial t} + \frac{\partial \bar{E}}{\partial \xi} + \frac{\partial \bar{F}}{\partial \eta} + \frac{\partial \bar{G}}{\partial \zeta} = \frac{\partial \bar{E}_v}{\partial \xi} + \frac{\partial \bar{F}_v}{\partial \eta} + \frac{\partial \bar{G}_v}{\partial \zeta} \qquad (2.29)$$

where

$$\bar{U} = U/J$$

$$\begin{aligned}
\bar{E} &= \frac{1}{J}(E\xi_x+F\xi_y+G\xi_z) \qquad \bar{E}_v = \frac{1}{J}(E_v\xi_x+F_v\xi_y+G_v\xi_z) \\
\bar{F} &= \frac{1}{J}(E\eta_x+F\eta_y+G\eta_z) \qquad \bar{F}_v = \frac{1}{J}(E_v\eta_x+F_v\eta_y+G_v\eta_z) \\
\bar{G} &= \frac{1}{J}(E\zeta_x+F\zeta_y+G\zeta_z) \qquad \bar{G}_v = \frac{1}{J}(E_v\zeta_x+F_v\zeta_y+G_v\zeta_z)
\end{aligned} \tag{2.30}$$

In many numerical schemes, the inviscid flux is split according to the characteristic direction. This is fulfilled by dividing the Jacobian matrix of the inviscid flux into two sub-matrices, which correspond to two different characteristic directions, either positive or negative. Let A,B,C denote the Jacobian matrix of **E,F,G** with respect to **U** respectively, i.e.,

$$A = \frac{\partial E}{\partial U} \qquad B = \frac{\partial F}{\partial U} \qquad C = \frac{\partial G}{\partial U}$$

then the Jacobian matrices $\bar{A}$, $\bar{B}$, $\bar{C}$ of $\bar{E}$, $\bar{F}$, $\bar{G}$ with respect to $\bar{U}$ are determined from

$$\bar{A} = \xi_x A + \xi_y B + \xi_z C \tag{2.31a}$$

$$\bar{B} = \eta_x A + \eta_y B + \eta_z C \tag{2.31b}$$

$$\bar{C} = \zeta_x A + \zeta_y B + \zeta_z C \tag{2.31c}$$

It is apparent that the matrices of (2.31) can be cast into the following matrix

$$M = k_1 A + k_2 B + k_3 C \tag{2.32}$$

It can be shown that M has real eigenvalues a^l and a complete set of right eigenvectors r^l, $l=1,\cdots,5$. Hence the matrix

$$R = \{r^1,\cdots,r^5\}$$

is invertible. The rows $l^1,\cdots,l^5$ of R^{-1} constitute an orthonormal set of left eigenvectors of M; thus

$$R^{-1}MR = \Lambda \qquad \text{or} \qquad M=R\Lambda R^{-1} \tag{2.33}$$

where Λ is a diagonal matrix

$$\Lambda = \begin{vmatrix} a^1 & & & & \\ & a^2 & & 0 & \\ & & a^3 & & \\ & & & a^4 & \\ & 0 & & & a^5 \end{vmatrix}$$

Any eigenvalue a^l can be expressed as

$$a^l = a^{l+} + a^{l-}$$

where

$$a^{l+} = \frac{a^l+|a^l|}{2} \qquad a^{l-} = \frac{a^l-|a^l|}{2}$$

Using the above formula, the diagonal matrix Λ can be split as

$$\Lambda = \Lambda^+ + \Lambda^-$$

where Λ^+ and Λ^- have diagonal elements a^{1+} and a^{1-} respectively. M is now divided in the following manner

$$M = M^+ + M^-$$

with

$$M^+ = R\Lambda^+R^{-1} \quad \text{and} \quad M^- = R\Lambda^-R^{-1}$$

The specific expressions of M, R, R^{-1} and Λ can be found in appendix A.

CHAPTER 3

DISCRETIZATION OF HYPERBOLIC CONSERVATION LAWS

3.1 Introduction to Hyperbolic Conservation Laws

Consider the following equation written in conservation form

$$\frac{\partial \mathbf{U}}{\partial t} + \frac{\partial \mathbf{F}}{\partial x} = 0 \qquad (3.1a)$$

where **U** is an m-vector of unknowns, and the flux function, **F(U)**, is vector valued, having m components. Let A denote the Jacobian of **F**, that is

$$A = \frac{\partial \mathbf{F}}{\partial \mathbf{U}}$$

The system is hyperbolic if A has real distinct eigenvalues, a^1, a^2, $\cdots$, a^m. For each eigenvalue a^l, there is a corresponding right eigenvector r^l and a left eigenvector l^l, that satisfies

$$Ar^l = a^l r^l \qquad l^l A = l^l a^l \qquad (l=1,\cdots,m)$$

When m=1, (3.1a) reduces to the scalar hyperbolic conservation laws, i.e.,

$$\frac{\partial u}{\partial t} + \frac{\partial f}{\partial x} = \frac{\partial u}{\partial t} + a(u)\frac{\partial u}{\partial x} = 0 \qquad (3.1b)$$

where $a(u)=\partial f/\partial u$, and u and f are scalars. It is well-known that the solution of (3.1) may develop discontinuities in finite time, even when

the initial data are smooth. In this case, (3.1) ceases to be valid. A different kind of solution of (3.1) has to be sought. For simplicity of discussion, we only consider scalar hyperbonic conservation laws (3.1b). Let $\pi(x,t)$ be a smooth scalar function that vanishes for $|x|$ sufficiently large, then

$$\int_0^{\infty} \int_{-\infty}^{+\infty} \pi\left(\frac{\partial u}{\partial t} + \frac{\partial f}{\partial x}\right) dxdt = 0$$

Using the divergence theorem

$$\int_0^{\infty} \int_{-\infty}^{+\infty} \left(u\frac{\partial \pi}{\partial t} + f\frac{\partial \pi}{\partial x}\right) dxdt + \int_{-\infty}^{+\infty} \pi(x,0) f dx = 0 \qquad (3.2)$$

If u and f are smooth, the steps can be reversed. Eq. (3.2) is called the weak form of the conservation laws. Any function u that satisfies (3.2) is called a weak solution of the conservation laws. If u is smooth, then it is also called a strong solution of the conservation laws.

It is important to note that equation (3.2) remains valid even if u is not smooth because u can still be integrated. Consider a discontinuous weak solution u of (3.1b), which has a finite jump $u_R - u_L$ at a certain time and position. Here u_L and u_R are the states on the left and right of the discontinuity. Then the Rankine-Hugoniot condition must be satisfied, i.e.,

$$|V|(u_R - u_L) = f(u_R) - f(u_L) \qquad (3.3)$$

where $|V|$ is the speed of the propagation of the discontinuity.

The class of weak solutions of the weak form of the conservation laws (3.2) is too large in the sense that there is no uniqueness in general. An additional principle is needed for determining the physically relevant solution. There is a variety of conditions for this purpose. Here the following condition is given: for every u between u_L and u_R, the entropy condition

$$\frac{f(u)-f(u_L)}{u-u_L} \geq |V| \geq \frac{f(u)-f(u_R)}{u-u_R} \tag{3.4}$$

must be satisfied. The weak solution satisfying the entropy condition (3.4) is uniquely determined by the initial data.

Consider the equation (3.1b) with initial conditions given by the step function

$$u(x,0)=\begin{cases} u_L & x<0 \\ u_R & x>0 \end{cases} \tag{3.5}$$

Such a problem is called a Riemann problem. The Riemann problem plays an important part in the derivation of some numerical algorithms. For a system of hyperbolic conservation laws, see appropriate reference (e.g. *Numerical Methods in Fluid Dynamics* by Sod) for more detailed information.

3.2 High Resolution Schemes for Hyperbolic Conservation Laws

3.2.1 Introduction

The concept of TVD schemes introduced by Harten [16] has provided a unifying framework for the study of shock capturing methods originating from the discretization of the hyperbolic conservation laws. TVD schemes preserve the monotonicity of an initially monotone profile, because the total variation would increase if the profile ceases to be monotone. Consequently, they prevent the formation of spurious oscillations. This is a very valuable property of a successful shock-capturing scheme because all classical high-order schemes demonstrated deficiencies in the vicinity of a shock wave because of severe numerical oscillations.

TVD schemes were originally designed for transient applications. However, the theory has also been successfully employed to construct schemes for steady flow calculations. It is well known that even if explicit schemes are easy to implement, they suffer severe restrictions in the choice of time step and thus are less efficient than their implicit counterparts. It is also true that it is inappropriate to extend the second-order Lax-Wendroff method to implicit schemes because the steady state solution is found to depend on size of the time step. This research addresses only steady state calculations, so only acceptable implicit schemes are considered.

Osher and Chakravarthy derived a family of high order upwind TVD schemes which can be third order accurate [8]. More recently, Yee [47] generalized the works of Davis [12] and Roe [29] and introduced the concept of the symmetric TVD scheme, which in some cases is easier to implement than the Osher-Chakravarthy family. Both schemes are more suitable for steady state flow simulation than Harten's second-order TVD scheme. Numerical experiments choosing the one dimensional inviscid flow

problem have demonstrated that these schemes have the capacity to give high resolution for shock waves and have the advantage of giving satisfactory solutions on even coarse grids. A straightforward extension of this approach of applying the one-dimensional scheme for each direction in multi-dimensional problems has also given quite satisfactory results. Comparisons have been made between a variety of the different TVD schemes [33,34]. The conclusion is that they are almost identical in their shock capturing abilities when applied to inviscid flow computations.

The high level of success of TVD schemes in the simulation of inviscid flow with shock waves has inspired their applications in viscous flow calculations. They are very attractive due to the fact that no coefficient of artificial numerical viscosity needs to be decided. However, blind use of these schemes can sometimes cause unrepresentative results. Therefore much has to be done to evaluate their capacities of resolving the viscous shear layer before they can be fully applied to the solution of viscous flows. For that purpose, efforts are made to unify both the Osher-Chakravarthy and the Yee TVD schemes, to identify their differences and features and to make modifications if necessary. This remains the main topic of the next sections.

3.2.2 TVD Concept and Its Sufficient Conditions

In this section we begin the discussion of the numerical solution of the hyperbolic conservation laws (3.1b) with appropriate initial condition

$$\frac{\partial u}{\partial t} + \frac{\partial f}{\partial x}=0 \qquad u(x,0) = u_0(x) \tag{3.6}$$

where $u_0(x)$ is assumed to have bounded variation. The total variation of the solution is defined as

$$TV(t) = \int_{-\infty}^{\infty} \left|\frac{\partial u(x,t)}{\partial x}\right| dx \tag{3.7}$$

It is well-known that any weak solution of (3.6) has a non-increasing total variation provided that any discontinuity in the solution satisfies an entropy condition, i.e.,

$$\frac{\partial TV(t)}{\partial t} \leq 0$$

Let u_j^n be the numerical solution of (3.6) at $x=j\Delta x$ and $t=n\Delta t$, with Δx the spatial mesh size and Δt the time step. Consider a general explicit and implicit scheme in conservative form

$$u_j^{n+1} + \lambda\vartheta(h_{j+1/2}^{n+1} - h_{j-1/2}^{n+1}) = u_j^n - \lambda(1-\vartheta)(h_{j+1/2}^n - h_{j-1/2}^n) \tag{3.8}$$

where $0\leq\vartheta\leq1$, $\lambda=\Delta t/\Delta x$, $h_{i+1/2}=h(u_{j-1}, u_j, u_{j+1}, u_{j+2})$, and h is a numerical flux function consistent with the conservation law in the following sense:

$$h(u_j, u_j, u_j, u_j) = f(u_j). \tag{3.9}$$

These general schemes contain explicit as well as implicit schemes. When $\vartheta=0$, (3.8) reduces to an explicit scheme. When $\vartheta\neq0$, (3.8) is an implicit scheme. For example: if $\vartheta=1/2$, the time differencing is the trapezoidal formula, and if $\vartheta=1$, the time differencing is the backward Euler method.

In analogy with the definition of the total variation of continuous solution in (3.7), the total variation of the discrete solution is defined as

$$TV(u^n) = \sum_{j=-\infty}^{\infty} \left| u_{j+1}^n - u_j^n \right| \tag{3.10}$$

When a numerical solution is sought, it is also required that the variation of the discretised solution is non-increasing or diminishing. That is

$$TV(u^{n+1}) \leq TV(u^n) \tag{3.11}$$

If the numerical flux h in (3.8) is Lipschitz continuous and (3.8) can be written as

$$u_j^{n+1} - \lambda\vartheta(C_{j+1/2}\Delta u_{j+1/2} - D_{j-1/2}\Delta u_{j-1/2})^{n+1} =$$

$$u_j^n + \lambda(1-\vartheta)(C_{j+1/2}\Delta u_{j+1/2} - D_{j-1/2}\Delta u_{j-1/2})^n \tag{3.12}$$

where $\Delta u_{j+1/2} = u_{j+1} - u_j$ and $C_{j+1/2}$, $D_{j-1/2}$ are some bounded function of $\{u_j\}$. Then Harten further showed that sufficient conditions for (3.11) are

(a) if for all j

$$\lambda(1-\vartheta)C_{j+1/2} \geq 0 \quad \text{and} \quad \lambda(1-\vartheta)D_{j+1/2} \geq 0$$

$$\lambda(1-\vartheta)(C_{j+1/2} + D_{j+1/2}) \leq 1 \tag{3.13}$$

and

(b) if for all j

$$-\infty < C \le -\lambda\vartheta C_{j+1/2} \le 0 \quad \text{and} \quad -\infty < C \le -\lambda\vartheta D_{j+1/2} \le 0 \tag{3.14}$$

for some finite C. Conditions (3.13) and (3.14) are very useful in guiding the construction of second-order accurate TVD schemes which do not exhibit the spurious oscillation associated with the more classical second-order schemes. In the next section, we will employ these sufficient conditions to build up a high-order general TVD scheme which is particularly useful for steady state problem solutions.

3.2.3 A General Form TVD Scheme

3.2.3.1 The Scheme for Linear Scalar Conservation Laws

For simplicity of discussion, first we consider $a=\partial f/\partial u$=constant, i.e., the linear wave equation

$$\frac{\partial u}{\partial t} + a\frac{\partial u}{\partial x} = 0, \quad a>0 \tag{3.15}$$

For steady state computation, the following numerical flux function is considered.

$$h_{j+1/2} = \frac{1}{2}a(u_j+u_{j+1}) - \frac{1}{2}a[1-q(r_{j+1/2})]\Delta u_{j+1/2} \tag{3.16}$$

with

$$r_{j+1/2} = \frac{\Delta u_{j-1/2}}{\Delta u_{j+1/2}} \tag{3.17}$$

and q is some function of r called a limiter. Several special schemes included in (3.16) are noted as follows.

If q(r)=0, the resultant scheme is a first order upwind scheme. We call this limiter q^1.

If q(r)=1, the resultant scheme is a central difference second order scheme (in space). Let this limiter be called q^c.

If q(r)=r, the resultant scheme is an upwind second-order scheme. Let this limiter be called q^u.

If q(r)=2/3+r/3 , the resultant scheme is third order accurate. Let this limiter be called q^t.

According to the physics of wave propagation, only the upwind stream affects the current position. Upwind schemes, therefore, are highly desirable in wave modelling. In fact, any upwind-biased second order scheme utilizing $u_{j-2}, u_{j-1}, u_j, u_{j+1}$ is a weighted average of the central difference and upwind second order scheme. Thus for any upwind-biased second order scheme, the limiter should satisfy

$$q(r)=\chi(r)q^c(r)+[1-\chi(r)]q^u(r)$$

$$=\chi(r)+[1-\chi(r)]r=r+\chi(r)(1-r) \tag{3.18}$$

with $0 \le \chi(r) \le 1$ i.e., interpolation. Numerical experiments have shown that extrapolation causes over-compression and/or instability.

This family contains implicit as well as explicit schemes and also first as well as second-order schemes. As a result of the fact that time differences and space differences are discretised separately, they also have the advantage that the solution is independent of the time step and that the order of accuracy in space is solely decided by the numerical flux functions when the steady state is achieved. Now we further look into the numerical flux function (3.16). When (3.16) is substituted into (3.8), the first term contributes to the discretization of $a\Delta x\partial u/\partial x$ to second-order accuracy without any numerical dissipation. The second term acts as a numerical dissipation term. When $q(r)<0$, the scheme would be more dissipative than the first-order scheme. When $q(r)>1$, the added numerical dissipation term is negative. Hence waves are usually compressed by the scheme. Possible non-physical solutions would result. It is noticed that when $q(r)=1$ no numerical dissipation is embedded in the scheme. This is a very desirable property when it is used to model a viscous flow at high Reynolds number, where the physical dissipation is very low. In fact, equation (3.8) with numerical flux function (3.16) can be rewritten in the form as (3.12) with

$$C_{j+1/2} = 0 \qquad D_{j-1/2} = a\left[1 + \frac{1}{2}q(r_{j+1/2})/r_{j+1/2} - \frac{1}{2}q(r_{j-1/2})\right]$$

Now sufficient conditions for this scheme to be TVD are

$$1 + \frac{1}{2}q(r_{j+1/2})/r_{j+1/2} - \frac{1}{2}q(r_{j-1/2}) \ge 0 \qquad (3.19a)$$

and

$$a\lambda(1-\vartheta)[1 + \frac{1}{2}q(r_{j+1/2})/r_{j+1/2} - \frac{1}{2}q(r_{j-1/2})] \le 1 \qquad (3.19b)$$

If we assume

$$\begin{cases} q(r) = 0 & r \le 0 \\ q(r) > 0 & r > 0 \end{cases}$$

Then we always have

$$q(r)/r \ge 0$$

Under these conditions, the following sufficient conditions are obtained

$$\begin{cases} 0 \le q(r_{j+1/2}) \le 2 \\ 0 \le q(r_{j+1/2})/r_{j+1/2} \le \dfrac{2}{\lambda a(1-\vartheta)} - 2 \end{cases} \qquad (3.20)$$

Denoting

$$\frac{2}{\lambda a(1-\vartheta)} - 2 = k,$$

it is always required that

$$k \ge 0 \qquad \text{i.e.,} \qquad \lambda \le \frac{1}{a(1-\vartheta)} \qquad (3.21)$$

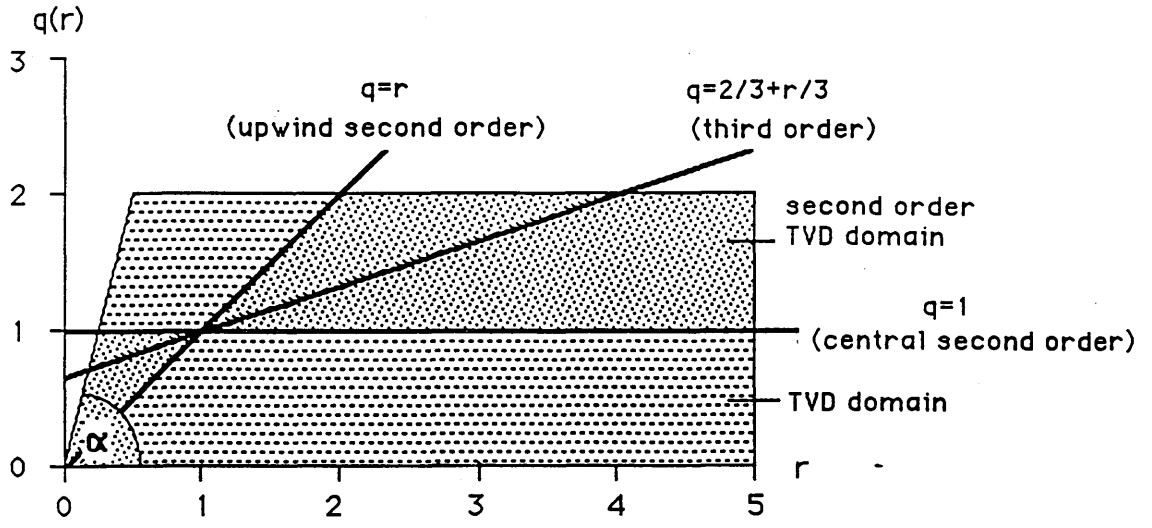

Fig. 3.1 TVD domain

Fig. 3.1 shows the TVD region with $\alpha=\tan^{-1}(k)$. Also displayed are the q functions needed to give the central difference and upwind second-order schemes, and the third order scheme. It is clear that for any upwind-biased second-order schemes, their limiters should lie between the two lines q=1 and q=r. The intersection of the second-order domain and TVD domain would give the second-order TVD domain, which has been specified in the figure. It is noticed that the upper boundary of the second-order TVD domain results in the most compressive second-order TVD scheme, i.e.,

$$\begin{cases} 0 & r \le 0 \\ kr & 0 \le r \le 1/k \\ 1 & 1/k \le r \le 1 \\ r & 1 \le r \le 2 \\ 2 & r > 2 \end{cases} \qquad (3.22)$$

In fact, this limiter is an analogue of Roe's Superbee in his Lax-Wendroff TVD scheme [29,30]. We also call this limiter Superbee, indicated by q^s.

In Fig. 3.1, it is obvious that the most compressive TVD-satisfying limiter function is

$$\begin{cases} 0 & r \le 0 \\ kr & 0 \le r \le 2/k \\ 2 & r > 2/k \end{cases} \tag{3.23}$$

Usually this limiter is too compressive. It will turn the sine wave into a square wave when it is applied to the linear wave equation (see section 5). This limiter is thus named "Supercompressive", denoted by q^p. Another limiter which is of particular interest in this paper is the following one

$$\begin{cases} 0 & r \le 0 \\ kr & 0 \le r \le 1/k \\ 1 & r > 1/k \end{cases} \tag{3.24}$$

When fully implicit schemes are employed, $k \to \infty$. In that case, the resultant scheme would possess no dissipation away from local extrema when limiter (3.24) is utilized.

3.2.3.2 The Scheme for Nonlinear Scalar Conservation Laws

To extend the scheme to the nonlinear scalar problem (3.6), one has to define the local characteristic speed first. This is done simply by

$$a_{j+1/2} = \begin{cases} (f_{j+1}-f_j)/\Delta u_{j+1/2} & \Delta u_{j+1/2} \neq 0 \\ \partial f(u_j)/\partial u & \Delta u_{j+1/2} = 0 \end{cases} \tag{3.25}$$

Following the sign of the characteristic speed, the parameter r is now redefined as

$$r_{j+1/2} = \frac{\Delta u_{j-\sigma+1/2}}{\Delta u_{j+1/2}} \quad \text{and} \quad \sigma = \text{sign}(a_{j+1/2}) \tag{3.26}$$

The numerical flux function for the nonlinear case is now

$$h_{j+1/2} = \frac{1}{2}(f_j+f_{j+1}) - \frac{1}{2}|a_{j+1/2}|[1-q(r_{j+1/2})]\Delta u_{j+1/2} \tag{3.27}$$

Modification has to be made concerning the conditions (3.20) due to the fact that $a_{j+1/2}$ is not always the same sign as $a_{j-1/2}$ or $a_{j+3/2}$. The new set of conditions are now found to be

$$\begin{cases} q(r_{j+1/2}) < 2 \\ q(r_{j+1/2})/r_{j+1/2} < \left[\dfrac{2}{\lambda(1-\vartheta)|a_{j-1/2}|} - 2\right]\left|\dfrac{a_{j-1/2}}{a_{j+1/2}}\right| \\ q(r_{j+1/2})/r_{j+1/2} < \left[\dfrac{2}{\lambda(1-\vartheta)|a_{j+3/2}|} - 2\right]\left|\dfrac{a_{j+3/2}}{a_{j+1/2}}\right| \\ |a_{j+1/2}| < \dfrac{1}{(1-\vartheta)\lambda} \end{cases} \tag{3.28}$$

It is clear that if and only if the scheme is fully implicit, the TVD scheme is unconditionally stable.

Notice that when $a_{j+1/2}=0$, the scheme has zero dissipation. This can sometimes cause entropy-violating solutions. One way to modify the scheme is to add a small dissipation to the flux function. For example,

instead of using (3.27), the following flux function

$$h_{j+1/2}= \frac{1}{2}(f_j+f_{j+1})- \frac{1}{2}\psi(a_{j+1/2})[1-q(r_{j+1/2})]\Delta u_{j+1/2} \tag{3.29}$$

can be used. Here ψ is a function of the following form

$$\psi(z) = \begin{cases} |z| & z \geq \varepsilon \\ \varepsilon & z < \varepsilon \end{cases} \tag{3.30}$$

where ε is a small positive number. This procedure is called entropy enforcement.

3.2.3.3 Linearization of the Implicit Scheme

From conditions (3.28) one sees that whenever $\vartheta \neq 1$, the scheme is conditionally stable under the CFL-like restriction. For a steady-state calculation, the fully implicit scheme is highly recommended since it is unconditionally stable. However, it should be linearized before it can possibly be used to solve any problem. The fully implicit scheme can be expressed as

$$u_j^{n+1} + \lambda(h_{j+1/2}^{n+1}-h_{j-1/2}^{n+1}) = u_j^n \tag{3.31a}$$

Substituting (3.29) into (3.31a), one obtains

$$u_j^{n+1}+ \frac{1}{2}\lambda\{f_{j+1}-\psi(a_{j+1/2})[1-q(r_{j+1/2})]\Delta u_{j+1/2}\}^{n+1}$$

$$- \frac{1}{2}\lambda\{f_{j-1}-\psi(a_{j-1/2})[1-q(r_{j-1/2})]\Delta u_{j-1/2}\}^{n+1}=u_j^n \tag{3.31b}$$

Using the Taylor expansion about time level n, we get

$$f_j^{n+1} = f_j^n + a_j^n(u_j^{n+1}-u_j^n) + O(\Delta t^2) \tag{3.32}$$

Applying the first-order approximation of (3.32) to (3.31b) and locally linearizing the coefficient of $\Delta u_{j\pm1/2}$ by changing the time level from (n+1) to n, the following equation is obtained

$$\begin{aligned} &u_j^{n+1} + \frac{1}{2}\lambda a_{j+1}^n (u_{j+1}^{n+1}-u_{j+1}^n) - \frac{1}{2}\lambda a_{j-1}^n (u_{j-1}^{n+1}-u_{j-1}^n) \\ &-\frac{1}{2}\lambda\psi(a_{j+1/2}^n)[1-q(r_{j+1/2}^n)](\Delta u_{j+1/2}^{n+1}-\Delta u_{j+1/2}^n) \\ &+\frac{1}{2}\lambda\psi(a_{j-1/2}^n)[1-q(r_{j-1/2}^n)](\Delta u_{j-1/2}^{n+1}-\Delta u_{j-1/2}^n) \\ &= u_j^n - \lambda(h_{j+1/2}^n - h_{j-1/2}^n) \end{aligned} \tag{3.33}$$

Denote $d_j = u_j^{n+1} - u_j^n$. Then Eq. (3.33) can be further written as

$$e_1 d_{j-1} + e_1 d_j + e_3 d_{j+1} = -\lambda(h_{j+1/2}^n - h_{j-1/2}^n) \tag{3.34}$$

where

$$e_1 = \frac{\lambda}{2}\{-a_{j-1} - \psi(a_{j-1/2})[1-q(r_{j-1/2})]\}^n \tag{3.35a}$$

$$e_2 = 1 + \frac{\lambda}{2}\{\psi(a_{j-1/2})[1-q(a_{j-1/2})] + \psi(a_{j+1/2})[1-q(a_{j+1/2})]\}^n \tag{3.35b}$$

$$e_3 = \frac{\lambda}{2}\{a_{j+1} - \psi(a_{j+1/2})[1-q(r_{j+1/2})]\}^n \tag{3.35c}$$

This linearized form follows Yee's conservative linearization technique [48]. When steady state is achieved, the solution is non-oscillatory because the steady solution is decided solely by the right-hand-side of

(3.34). For the same reason, the implicit operator of (3.34) can be simplified further. For example, the first-order backward Euler scheme can be used as the implicit part by letting q(r)=0; i.e., redefine (3.35) as

$$e_1 = \frac{\lambda}{2}[-a_{j-1} - \psi(a_{j-1/2})]^n \tag{3.36a}$$

$$e_2 = 1 + \frac{\lambda}{2}[\psi(a_{j-1/2}) + \psi(a_{j+1/2})]^n \tag{3.36b}$$

$$e_3 = \frac{\lambda}{2}[a_{j+1} - \psi(a_{j+1/2})]^n \tag{3.36c}$$

In fact this linearization approach is employed throughout this research.

3.2.4 Comparison of the Osher-Chakravarthy and the Yee TVD Schemes and the Modified Yee TVD Scheme

3.2.4.1 The Osher-Chakravarthy Scheme

Osher-Chakravarthy derived a family of high order TVD schemes suitable for steady state problems. For the linear scalar equation (3.15), the numerical flux function takes the form

$$h_{j+1/2} = au_j + \frac{1+\varphi}{4}[d\tilde{f}_{j+1/2}] + \frac{1-\varphi}{4}[d\bar{f}_{j-1/2}] \tag{3.37a}$$

where φ is a parameter and $-1 \le \varphi \le 1$. The symbols ~ and - shown over df denote flux-limited values of df and are computed as follows:

$$d\tilde{f}_{j+1/2} = \text{minmod}(a\Delta u_{j+1/2},\ \beta a\Delta u_{j-1/2}) \tag{3.37b}$$

$$d\bar{f}_{j-1/2} = \text{minmod}(a\Delta u_{j-1/2},\ \beta a\Delta u_{j+1/2}) \tag{3.37c}$$

where the minmod function is defined as

$$\text{minmod}(x,y) = \begin{cases} 0 & xy < 0 \\ \text{sign}(x)\min(|x|,\ |y|) & xy \geq 0 \end{cases} \tag{3.38}$$

Actually, Eq.(3.37) can be written as (3.16) with

$$q(r_{j+1/2}) = \frac{1+\varphi}{2}\Upsilon(r_{j+1/2}) + \frac{1-\varphi}{2} r_{j+1/2}\Upsilon\left[\frac{1}{r_{j+1/2}}\right] \tag{3.39a}$$

where

$$\Upsilon(r_{j+1/2}) = \text{minmod}(1,\ \beta r_{j+1/2}) \tag{3.39b}$$

It is now necessary to decide the range of β which makes the scheme TVD.

Obviously, the following can be obtained from (3.39)

$$q(r) = \begin{cases} 0 & r \leq 0 \\ \frac{1+\varphi}{2}\beta r + \frac{1-\varphi}{2} r & 0 < r \leq 1/\beta \\ \frac{1+\varphi}{2} + \frac{1-\varphi}{2} r & 1/\beta < r < \beta \\ \frac{1+\varphi}{2} + \frac{1-\varphi}{2}\beta & r \geq \beta \end{cases} \tag{3.40}$$

Hence it is quite clear that

$$\max[q(r)] = \frac{1+\varphi}{2} + \frac{1-\varphi}{2}\beta \tag{3.41a}$$

and

$$\max[q(r)/r] = \frac{1+\varphi}{2}\beta + \frac{1-\varphi}{2} \tag{3.41b}$$

But the following should be satisfied

$$\max[q(r)] \leq 2$$

and

$$\max[q(r)/r] \leq \frac{2}{\lambda c(1-\vartheta)} - 2 = k$$

Thus it is required that

$$\beta \leq \min\left[\frac{3-\varphi}{1-\varphi}, \frac{2k-1+\varphi}{1+\varphi}\right] \tag{3.42}$$

For $\vartheta = 1$, i.e., the backward Euler scheme, $k \longrightarrow \infty$, then

$$\beta_{max} = \frac{3-\varphi}{1-\varphi} \tag{3.43}$$

This is actually the condition given by Osher and Chakravarthy in their original paper [8]. For $\vartheta = 0$, i.e., the explicit scheme,

$$k=2(\frac{1}{\nu} - 1)$$

where

$$\nu = c\lambda$$

Thus, k depends on ν, and so does β_{max}. If the CFL number is fixed to,

say, 1/3, then k = 4 and

$$\beta_{max} = \min\left[\frac{3-\varphi}{1-\varphi}, \frac{7+\varphi}{1+\varphi}\right] \tag{3.44}$$

Table 3.1 shows the maximum β for different value of φ (ν=1/3). For each value of φ, the respective limiter function is plotted in Fig. 3.2. It is shown that all the limiters are within the upwind-biased second order domain.

ϕ	Underlying Scheme	β_{max}
1/3	Third-order	4
-1	Fully Upwind	2
0	Fromm's	3
1/2	Low TE Second-order	5
1	Central	4
-1/3	Un-named	5/2

Table 3.1 β_{max} for explicit Osher-Chakravarthy scheme with ν=1/3 (TE — Truncation Error)

3.2.4.2 The Yee Scheme and the Modified Yee Scheme

Yee [47] generalized the works of Davis [12] and Roe [29] more recently, and introduced the symmetric TVD scheme. Again, for the scalar wave equation, the numerical flux function of the Yee scheme is

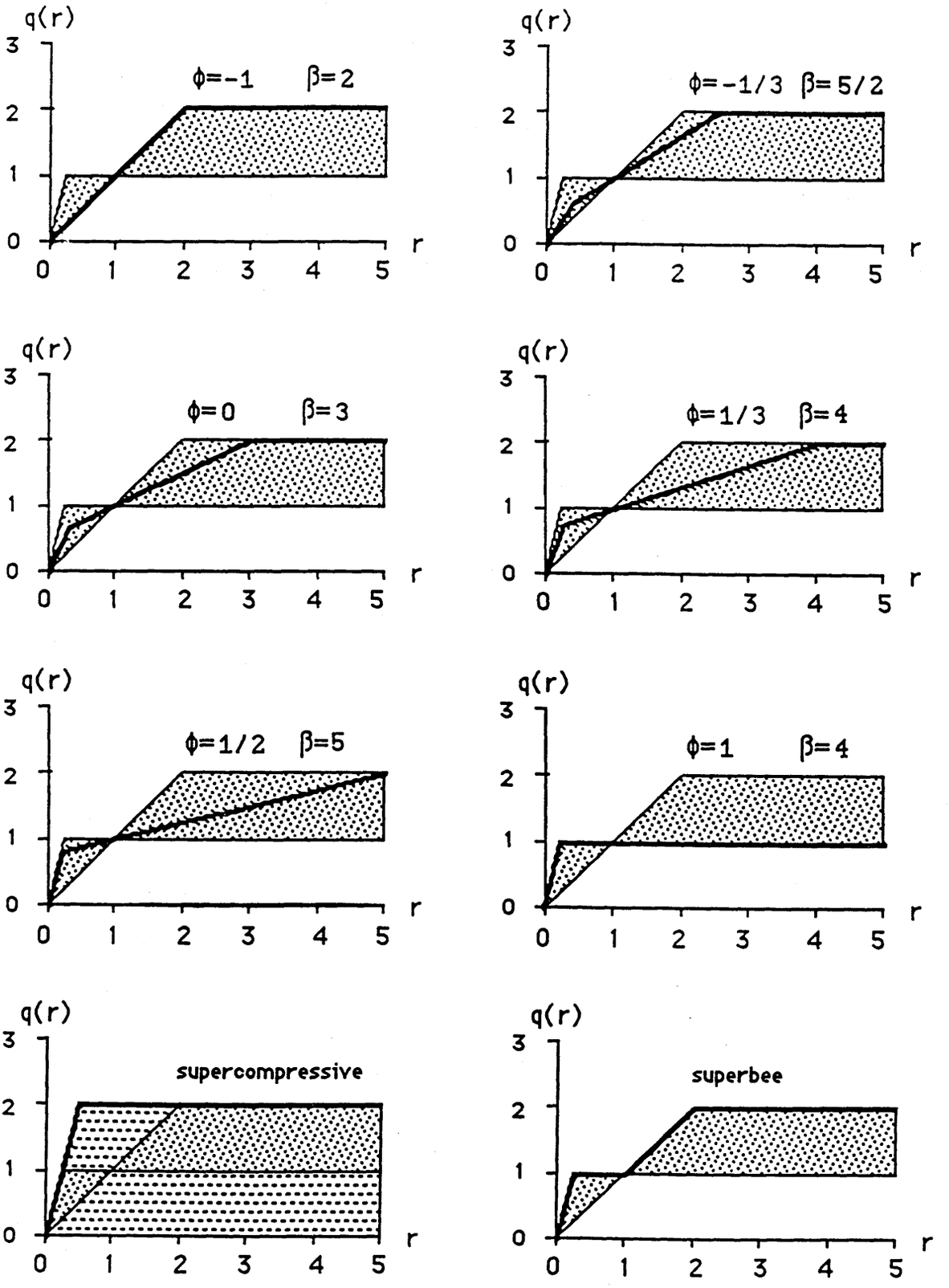

Fig. 3.2 Limiter functions

$$h_{j+1/2} = \frac{1}{2}a(u_{j+1} + u_j) - \frac{1}{2}a(1-Q)\Delta u_{j+1/2} \tag{3.45a}$$

with

$$Q=Q(r^+_{j+1/2}\ ,\ r^-_{j+1/2}) \tag{3.45b}$$

and

$$r^+_{j+1/2} = \frac{\Delta u_{j+3/2}}{\Delta u_{j+1/2}} \qquad r^-_{j+1/2} = \frac{\Delta u_{j-1/2}}{\Delta u_{j+1/2}} \tag{3.45c}$$

It is clear that $r^-_{j+1/2}$ is identical to the previously defined $r_{j+1/2}$. Yee's typical limiter functions are

$$Q(r^+ ,r^-) = \text{minmod}(r^+,\ r^-,\ 1) \tag{3.46a}$$

$$Q(r^+,\ r^-) = \text{minmod}(1,\ r^+) + \text{minmod}(1,\ r^-) - 1 \tag{3.46b}$$

$$Q(r^+,\ r^-) = \text{minmod}(2, 2r^+, 2r^-, 0.5(r^+ + r^-)) \tag{3.46c}$$

The difference in the definition of the limiter functions is obvious. Yee's limiters are equally dependent on the upwind and downwind gradients which makes the name symmetric TVD natural. Comparing (3.45) and (3.16), it is easy to see that

$$q = Q(r^+_{j+1/2},\ r^-_{j+1/2}) \tag{3.47}$$

Obviously, with a proper choice of CFL-like conditions, that is, $\lambda a \leq$ constant, these limiters satisfy the conditions (3.20). If the backward Euler scheme is used for time discretization, the Yee scheme is

unconditionally TVD. It needs to be pointed out that Q in (3.46b) can be negative. So Q should return to zero once a negative value is obtained from (3.46b). Because of the symmetric property of Yee's TVD scheme, limiter functions (3.46) introduced extra dissipation even if the solution is relatively smooth. Take limiter (3.46a) for example. If $0<r^+<r^-<1$, then Q will be equal to r^+ instead of r^-. That means

$$q < r_{j+1/2} \tag{3.48}$$

Hence this function lies outside of the upwind-biased second order TVD region. The result of this is that it includes extra dissipation because the dissipation coefficient $(1-r^+)$ is larger than $(1-r^-)$. The extra amount of dissipation the Yee scheme possesses usually does no harm to the solution of Euler equations. However when it is used to solve the Navier-Stokes equations, especially for problems at high Reynolds number, caution needs be exercised to ensure that the numerical dissipation does not exceed the physical dissipation. Otherwise, the solution would be meaningless.

Remedies to make Yee's TVD scheme less dissipative while maintaining its TVD property are now presented. The limiter functions are formulated according to the specific wave direction, i.e.,

$$Q(r+,r-)=\frac{1+\text{sign}(a)}{2}\text{minmod}(1,\ r^-)+\frac{1-\text{sign}(a)}{2}\text{minmod}(1,\ r^+) \tag{3.49a}$$

$$Q(r+,r-)=\frac{1+\text{sign}(a)}{2}\text{minmod}(1,\ \omega r^-)+\frac{1-\text{sign}(a)}{2}\text{minmod}(1,\ \omega r^+) \tag{3.49b}$$

where $1<\omega<\infty$ for fully implicit schemes. Limiters (3.49a) and (3.49b) are called MY1 and MY2 respectively. MY2 is expected to be very useful for

viscous flow calculations because of its low dissipation property. Numerical experiments as outlined in later section do show that the modified Yee schemes give better results.

3.3 Extension of TVD Schemes to System of Conservation Laws

In this section we describe how to extend our general TVD schemes to a system of conservation laws. The basic idea is to extend the scalar scheme to the system by applying it to each of the m scalar characteristic equations.

3.3.1 Formal Extension

First we consider Eq.(3.1a) with $A=\partial F/\partial U$=constant. Let R be the matrix whose columns are the right eigenvectors $\{r^l\}$ of the Jacobian matrix A. Then

$$R^{-1}AR = A = \mathrm{diag}(a^l) \tag{3.50}$$

where R^{-1} is the matrix the rows of which constitute a complete set of left eigenvectors $\{l^l\}$ of A. The characteristic variables are defined as

$$w = \{w^l\} = R^{-1}U \tag{3.51}$$

It follows from (3.50) and (3.51) that (3.1a) decouples into m scalar characteristic equations,

$$\frac{\partial w^l}{\partial t} + a^l\frac{\partial w^l}{\partial x} = 0 \qquad 1\le l\le m \tag{3.52}$$

This offers a natural way of extending a scalar scheme to a constant coefficient system by applying it in a scalar fashion to each of the m scalar characteristic variables.

Now a similar idea is exploited to extend the scalar schemes to a system of nonlinear conservation laws. Let $\mathbf{U}_{j+1/2}$ denote some symmetric average of $\mathbf{U}_j$ and $\mathbf{U}_{j+1}$. Let $a^l_{j+1/2}$, $R_{j+1/2}$, $R^{-1}_{j+1/2}$ denote the quantities a^l, R, R^{-1} evaluated at $\mathbf{U}_{j+1/2}$. Define

$$\alpha_{j+1/2} = R^{-1}_{j+1/2}\Delta\mathbf{U}_{j+1/2} \tag{3.53}$$

as the difference of the local characteristic variables. With the above notations, the general TVD schemes (3.8) in the system case can be written as

$$\mathbf{U}^{n+1}_j + \lambda\vartheta(\mathbf{H}^{n+1}_{j+1/2} - \mathbf{H}^{n+1}_{j-1/2}) = \mathbf{U}^n_j - \lambda(1-\vartheta)(\mathbf{H}^n_{j+1/2} - \mathbf{H}^n_{j-1/2}) \tag{3.54a}$$

The numerical function H can be expressed as

$$\mathbf{H}_{j+1/2} = \frac{1}{2}(\mathbf{F}_j + \mathbf{F}_{j+1} - R_{j+1/2}\Phi_{j+1/2}) \tag{3.54b}$$

where the element of Φ denoted by ϕ^l, $l=1,\cdots,m$ are

$$\phi^l_{j+1/2} = \psi(a^l_{j+1/2})[1-q(r^l_{j+1/2})]\alpha^l_{j+1/2} \tag{3.54c}$$

with $\psi(z)$ defined in (3.30) and

$$r^l_{j+1/2} = \frac{\alpha^l_{j+1-\sigma} - \alpha^l_{j-\sigma}}{\Delta\alpha^l_{j+1/2}} \qquad \sigma = \text{sign}(a^l_{j+1/2}) \tag{3.54d}$$

Here $\alpha^l_{j+1/2}$ are the elements of $\alpha_{j+1/2}$. The function q(r) can be the Yee limiters, the modified Yee limiters or the Osher-Chakravarthy limiters.

3.3.2 Linearization of the Implicit Operator

The linearization of the resultant implicit scheme is done in a similar fashion as the scalar case. Denote $\mathbf{D}_j = \mathbf{U}^{n+1}_j - \mathbf{U}^n_j$. The corresponding conservative linearized form for the system case can then be expressed as (ϑ=1 implied)

$$E_1\mathbf{D}_{j-1} + E_1\mathbf{D}_j + E_3\mathbf{D}_{j+1} = -\lambda(\mathbf{H}^n_{j+1/2} - \mathbf{H}^n_{j-1/2}) \tag{3.55}$$

where

$$E_1 = \frac{\lambda}{2}\{-A_{j-1} - K_{j-1/2}\}^n \tag{3.56a}$$

$$E_2 = I + \frac{\lambda}{2}(K_{j-1/2} + K_{j+1/2})^n \tag{3.56b}$$

$$E_3 = \frac{\lambda}{2}\{A_{j+1} - K_{j+1/2}\}^n \tag{3.56c}$$

with

$$K_{j\pm1} = (R\Omega R^{-1})_{j\pm1/2} \tag{3.57}$$

and

$$\Omega_{j\pm1/2} = \mathrm{diag}\{\psi(a^1_{j\pm1/2})[1-q(r^1_{j\pm1/2})]\} \tag{3.58a}$$

or for the first order left-hand side

$$\Omega_{j\pm1/2} = \mathrm{diag}[\psi(a^1_{j\pm1/2})] \tag{3.58b}$$

Here $\mathrm{diag}(z^1)$ denotes a diagonal matrix with diagonal elements z^1. The resultant scheme encompasses five points generally, but it forms only a block tridiagonal system.

3.4 Roe's Approximate Riemann Solver

The extension of the TVD schemes to a nonlinear system of hyperbonic conservation laws demands an averaging procedure of the two neighbouring states. This is fulfilled by Roe's approximate Riemann solver [28]. Let $\mathbf{U}^L$ and $\mathbf{U}^R$ be the right and left dependent variables of a certain interface. The Riemann solver is a mechanism to divide the flux difference between them into component parts associated with each wave field. Generally speaking, the associated waves in a nonlinear system are highly nonlinear. They require very expensive procedures in order to calculate them. Roe proposed an approximate solver which simulates these nonlinear waves by a kind of linear wave pattern. These waves have similar features to the original nonlinear waves to some extent.

Consider the nonlinear system

$$\frac{\partial \mathbf{U}}{\partial t} + \frac{\partial \mathbf{F}}{\partial x} = \frac{\partial \mathbf{U}}{\partial t} + \mathbf{A}(\mathbf{U})\frac{\partial \mathbf{U}}{\partial x} = 0 \tag{3.59a}$$

with initial condition

$$U(x,0) = \begin{cases} U_L & x < 0 \\ U_R & x > 0 \end{cases} \tag{3.59b}$$

Instead of solving (3.59), Roe suggested the following approximate problem

$$\frac{\partial U}{\partial t} + A(U^L, U^R)\frac{\partial U}{\partial x} = 0 \tag{3.60}$$

with the same initial condition. Here $A(U^L, U^R)$ is a constant matrix which satisfies

a. $F(U^R) - F(U^L) = A(U^L, U^R)(U^R - U^L) = A(\bar{U})(U^R - U^L)$

b. the eigenvectors of $A(U^L, U^R)$ being linearly independent

c. $A(U, U) = A(U)$

d. $U^R - U^L = R(\bar{U})\alpha$

where α represents the vector of the jump in the characteristic variables, and $\bar{U}$ is an average state between U^R and U^L. The most valuable property of Roe's approximate solver is that it returns the exact solution whenever U^L and U^R lie on opposite sides of a shock wave or a contact continuity. For one-dimensional Euler equation of perfect gas, Roe gave the following unique averaging values of density, velocity, and enthalpy:

$$\bar{\rho} = \frac{\rho^L + D\rho^R}{1+D} \tag{3.61a}$$

$$\bar{u} = \frac{u^L + Du^R}{1+D} \tag{3.61b}$$

$$\bar{h} = \frac{h^L + Dh^R}{1+D} \tag{3.61c}$$

$$\bar{c} = (\gamma-1)\left[\bar{h} - \frac{1}{2}\bar{u}^2\right] \tag{3.61d}$$

with

$$D = \left(\frac{\rho^R}{\rho^L}\right)^{1/2} \tag{3.61e}$$

3.5 Numerical Experiments and Discussions

To demonstrate the performance of the numerical schemes, a variety of numerical experiments have been conducted. Both linear and non-linear, inviscid and viscous problems have been solved using these high-resolution schemes. The results are presented as follows.

3.5.1 The first numerical experiment is performed on the linear wave equation (3.15). Both square waves and sine waves are chosen to represent discontinuous and smooth wave propagation. The explicit schemes (ϑ=0) are used. The limiters employed are the Osher-Chakravarthy, Yee, and the modified Yee scheme limiters. As a result, the schemes are only first-order accurate in time but second order in space. However, some of the results obtained are strikingly good. For the following calculations, a fixed CFL number of 1/3 is used throughout. For the square-wave calculation, fifty-one time steps and for sine wave calculation, twenty-

seven time-steps are propagated.

For the Yee scheme, two limiters are employed, i.e., those given by (3.46a) and (3.46c). They are called Y1 and Y2 respectively. For the Osher-Chakravarthy scheme, different values of φ are selected, and various values of β_{max} are used.

Also present are results using Superbee and Supercompressive. For the linear advection problem, the modified Yee scheme with limiter (3.49a) is identical to the Osher-Chakravarthy scheme with φ=1 and β=1.

Fig. 3.3 shows results for the square wave calculation. The solid line represents the exact solution. It can be seen that the Supercompressive limiter gives the best result and cannot be differentiated from the exact solution. The next best result comes from the solution utilizing Superbee, followed by the Osher-Chakravarthy scheme with φ=1/2, β = 5 and φ = 1/3, β = 4 respectively.

As expected, the Osher-Chakravarthy scheme with any value of φ gives better results than the Yee scheme as far as the resolution of the discontinuity is concerned. Comparing the results from Y1, Y2 and the results from the Osher-Chakravarthy schemes, it is found apparently that the Yee scheme gives the most dissipative results downstream of steep gradients. This is due to the fact that $q(r)<r$ at such places. The modified Yee schemes give superior results than the original schemes. It is also obvious that Y2 gives better results than Y1 and the Yee scheme gives better results than the first-order scheme.

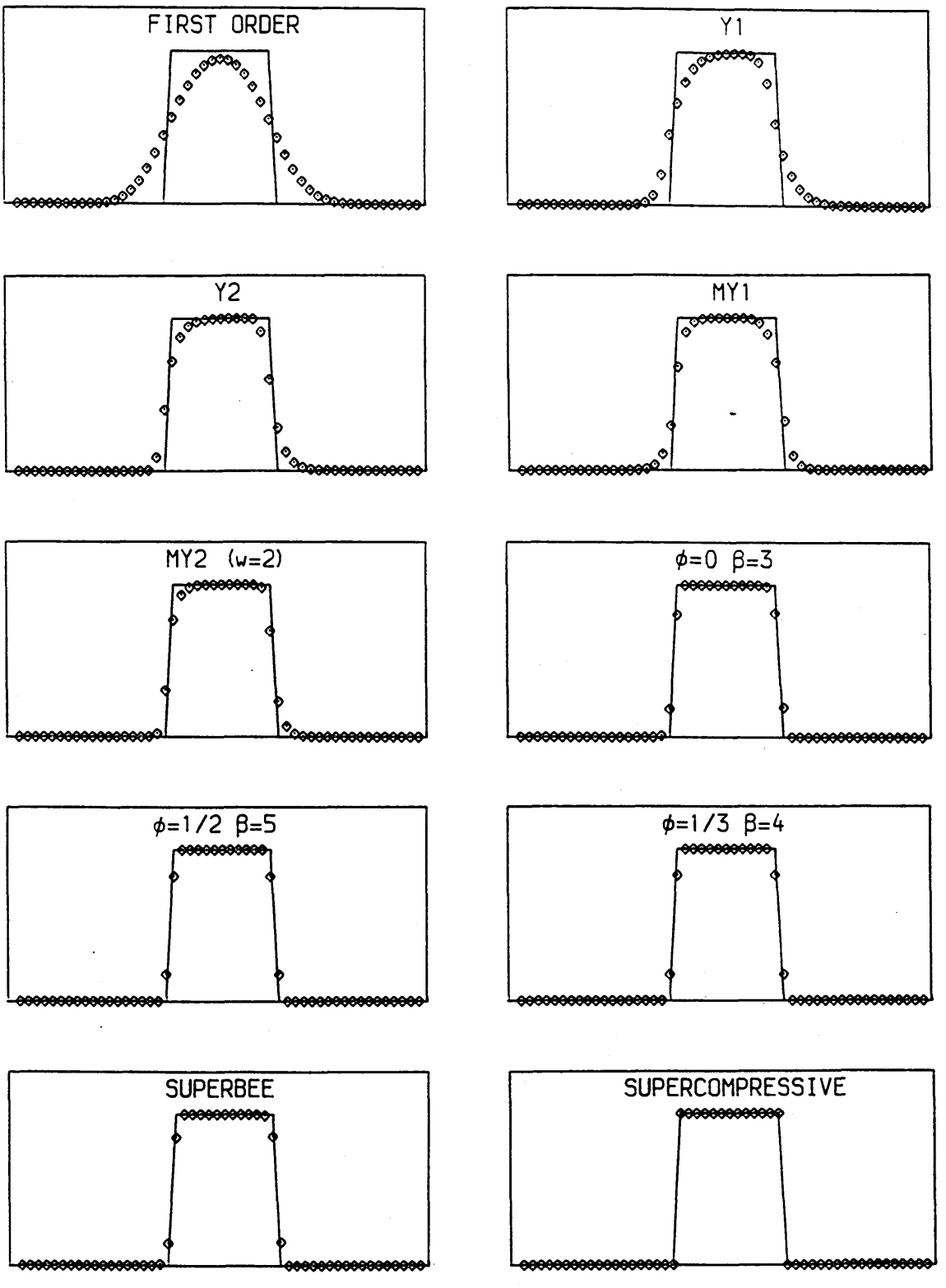

Fig. 3.3 Square wave propagation (— exact, ∘ present)

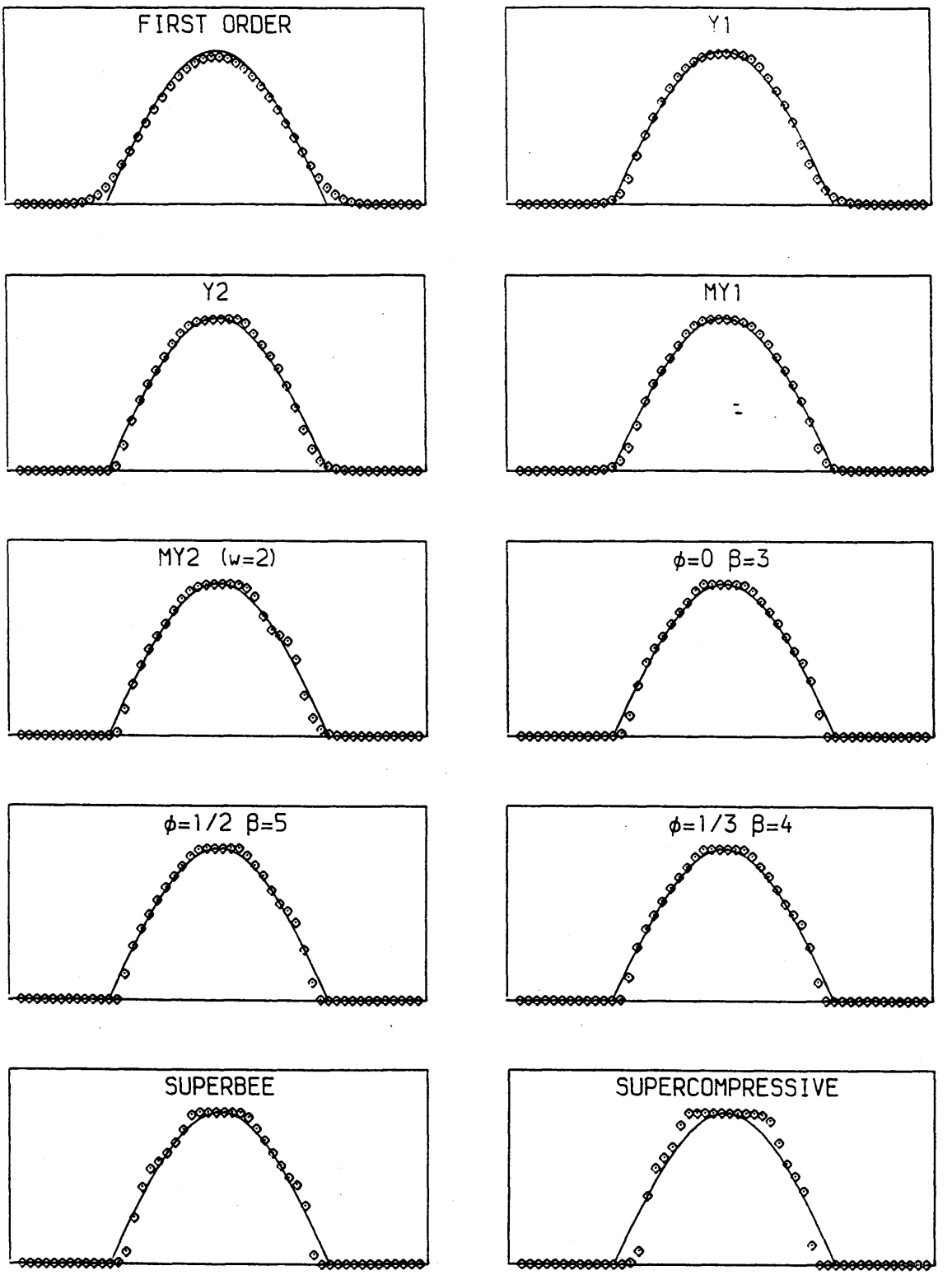

Fig. 3.4 Sine wave propagation (— exact, ∘ present)

Fig. 3.4 illustrates the results for the sine wave calculation. It is clear that both Supercompressive and Superbee are over compressive. This is due to the fact that some "negative" dissipation is built into these schemes (q>1). It is also found that for any value of φ, β_{max} results in a "squared" sine wave as can be seen in Fig. 3.4. It appears that the results given by Y1 and Y2 have a better agreement with the exact solution than those given by the Osher-Chakravarthy scheme. The reason behind this phenomenon is believed to be that the time-stepping approach is only first-order accurate so that a negative second-order dissipation term is embedded. This explains the slight "squaring" effect on top of the sine wave even in the results given by MY1 and MY2.

3.5.2 The second test problem is the inviscid quasi-one-dimensional nozzle problem. The governing equation for this problem is

$$\frac{\partial \mathbf{U}}{\partial t} + \frac{\partial \mathbf{F}(\mathbf{U})}{\partial x} - \Xi(\mathbf{U}) = 0 \tag{3.62}$$

where

$$\mathbf{U} = \kappa \begin{bmatrix} \rho \\ \rho v \\ E_t \end{bmatrix} \quad \mathbf{F} = \kappa \begin{bmatrix} \rho v \\ (p+\rho v^2) \\ (E_t+p)v \end{bmatrix} \quad \Xi = \begin{bmatrix} 0 \\ p\partial\kappa/\partial x \\ 0 \end{bmatrix} \tag{3.63}$$

with $\kappa(x)$, the cross area of the nozzle, and ρ, p, E_t and v are density, pressure, total energy and velocity respectively. The configuration considered (see Fig. 3.5) is a divergent nozzle with

$$\kappa(x)=1.398+0.347\tanh(0.8x-4) \tag{3.64}$$

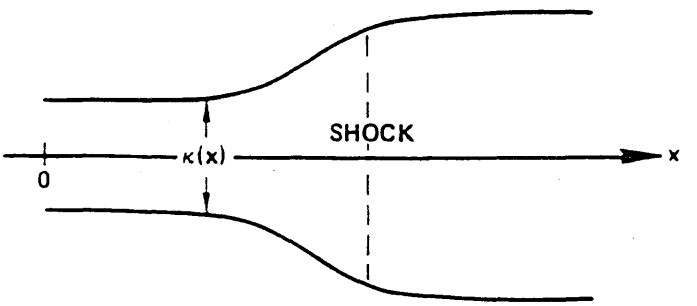

Fig. 3.5 Divergent nozzle

The flow condition is supersonic at the entrance and subsonic at the exit divided by a normal shock. The computational domain is selected to be $0 \le x \le 10$, and a very coarse evenly-spaced mesh of $\Delta x = 0.5$ is used to evaluate the resolution capacity of the scheme. The schemes are extended to system of conservation laws according to the technique in section 3.3. Roe's approximate Riemann solver is employed to define the local characteristics. For objective comparisons no entropy enforcement is applied, i.e., $\varepsilon = 0$ in (3.30).

Fig. 3.6 presents the results for the Yee, modified Yee and Osher-Chakravarthy schemes with different choices of limiter and relevant parameters. In the experiments with $\varphi = 0.5$ and $\varphi = 1/3$, it is found that β_{max} gives slightly oscillatory results. It is speculated that these schemes are over compressive with the result that instability has set in resulting in the overshoot near the shock wave. The upstream of the shock is seen to be smeared by the first-order scheme. All the rest of the schemes demonstrated almost equally good quality in their shock resolution capacities.

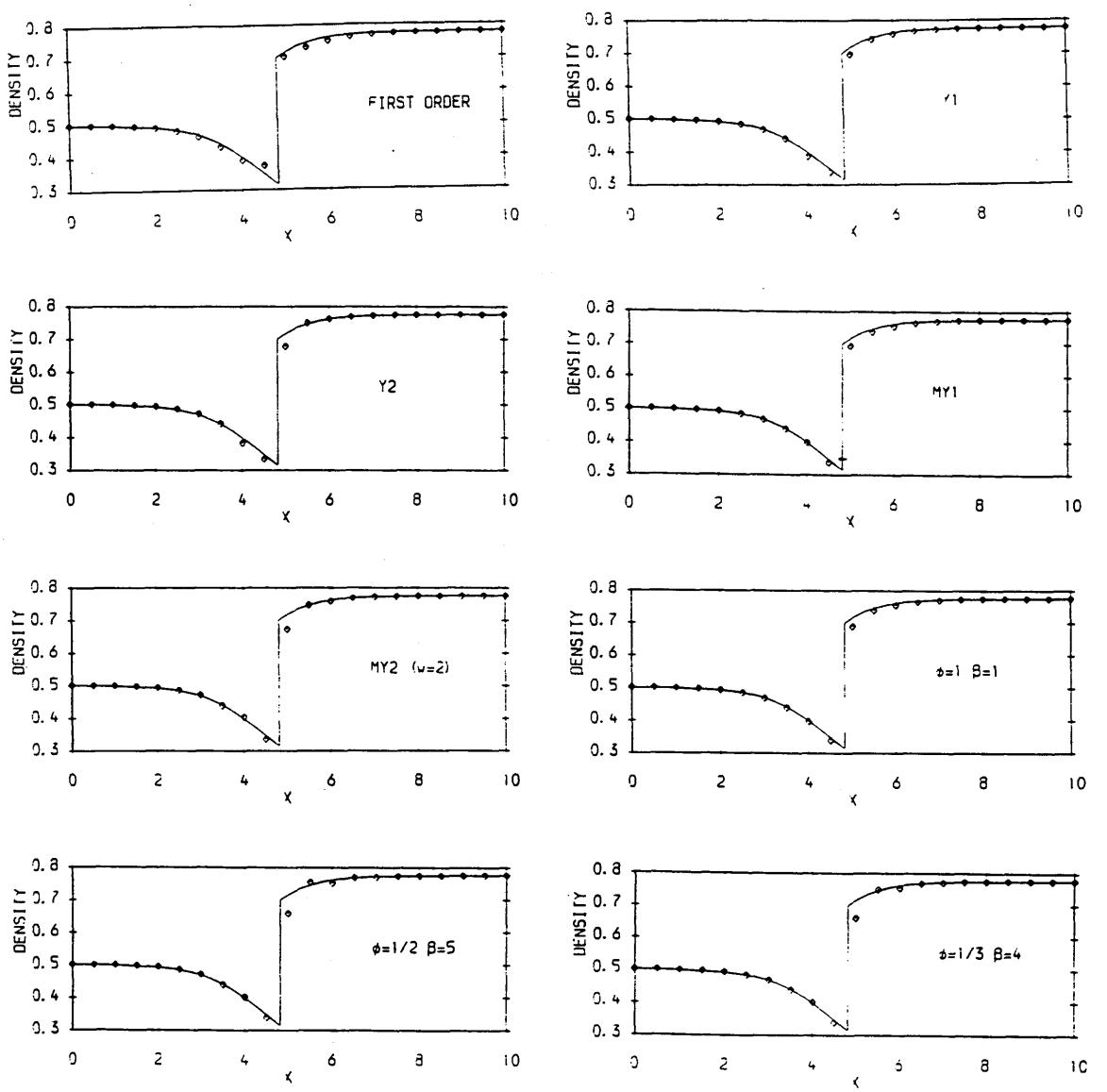

Fig. 3.6 Density distribution

3.5.3 The last experiment chosen is to test the ability of the different TVD schemes to resolve a boundary layer. For this purpose, a shock wave/boundary layer interaction problem is chosen. The flowfield representing this interaction is sketched in Fig. 3.7. An oblique shock wave is generated externally and is incident upon a boundary layer on a

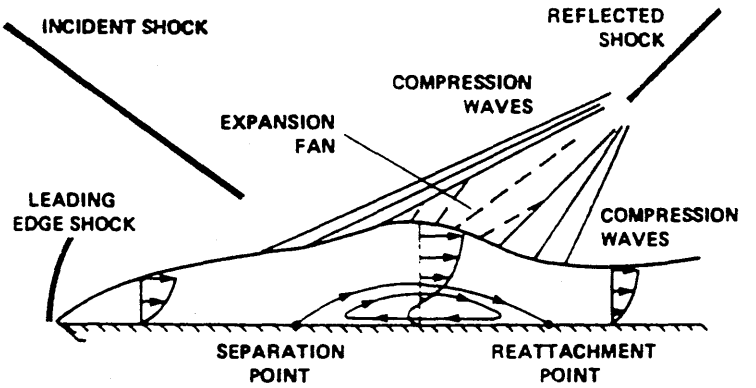

Fig. 3.7 Sketch for shock-boundary layer interaction

flat plate. If the shock is strong enough, the boundary layer would separate from the surface of the plate and reattach downstream. The separation region is a demanding one to calculate and therefore serves as a good test for a numerical method. The computational domain is chosen to be $-0.02 \le x \le 0.3$ and $0.0 \le y \le 0.1215$. The grid is composed of 33x33 points, and is clustered near the wall using the following stretch function

$$y(\eta)=y(0)+\left[1+\beta\frac{1-\left(\frac{\beta+1}{\beta-1}\right)^{1-\eta}}{1+\left(\frac{\beta+1}{\beta-1}\right)^{1-\eta}}\right][y(1)-y(0)] \qquad (3.65)$$

Here $0 \le \eta \le 1$ and $\beta=1.001$. The Reynolds number based on a reference length of 0.16 (the unit of length being foot) is taken to be 296000. The free stream Mach number is 2.0. The flat plate is introduced from x=0.03. A shock is imposed at x=0, y=0.1215 such that it slopes to the flat plate at 32.6 degrees. The governing equations are the two-dimensional Navier-Stokes equations.

In the numerical experiment, the inviscid flux vectors E and F are discretised using a TVD scheme, and the viscous terms (E_v and F_v) are discretised using central differences. Roe's approximate Riemann solver is employed to define the local characteristics. No entropy modification is employed. Then the implicit factorization method is utilized to solve the resultant system.

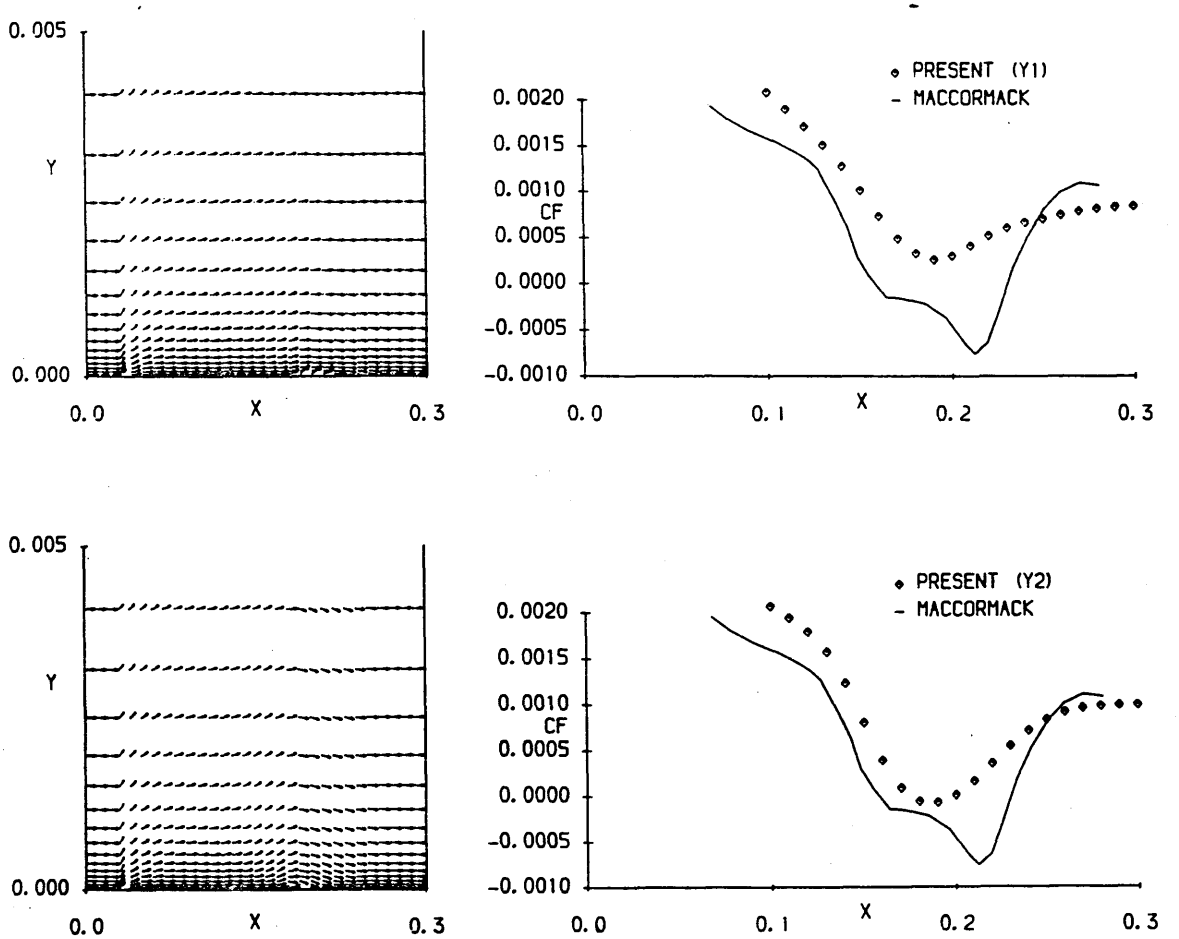

Fig. 3.8 Plots of velocity direction and skin friction coefficient of the Yee scheme

Fig. 3.8, Fig. 3.9 and Fig. 3.10 show plots of the velocity direction, and skin friction coefficient for calculations with the Yee, modified Yee and Osher-Chakravarthy schemes respectively since these two physical properties are the most distinguishing. The results are compared with the results from MacCormack [21] which appeared to agree well with experimental results. From the velocity plot, we can see clearly that both the modified Yee scheme and the Osher-Chakravarthy scheme

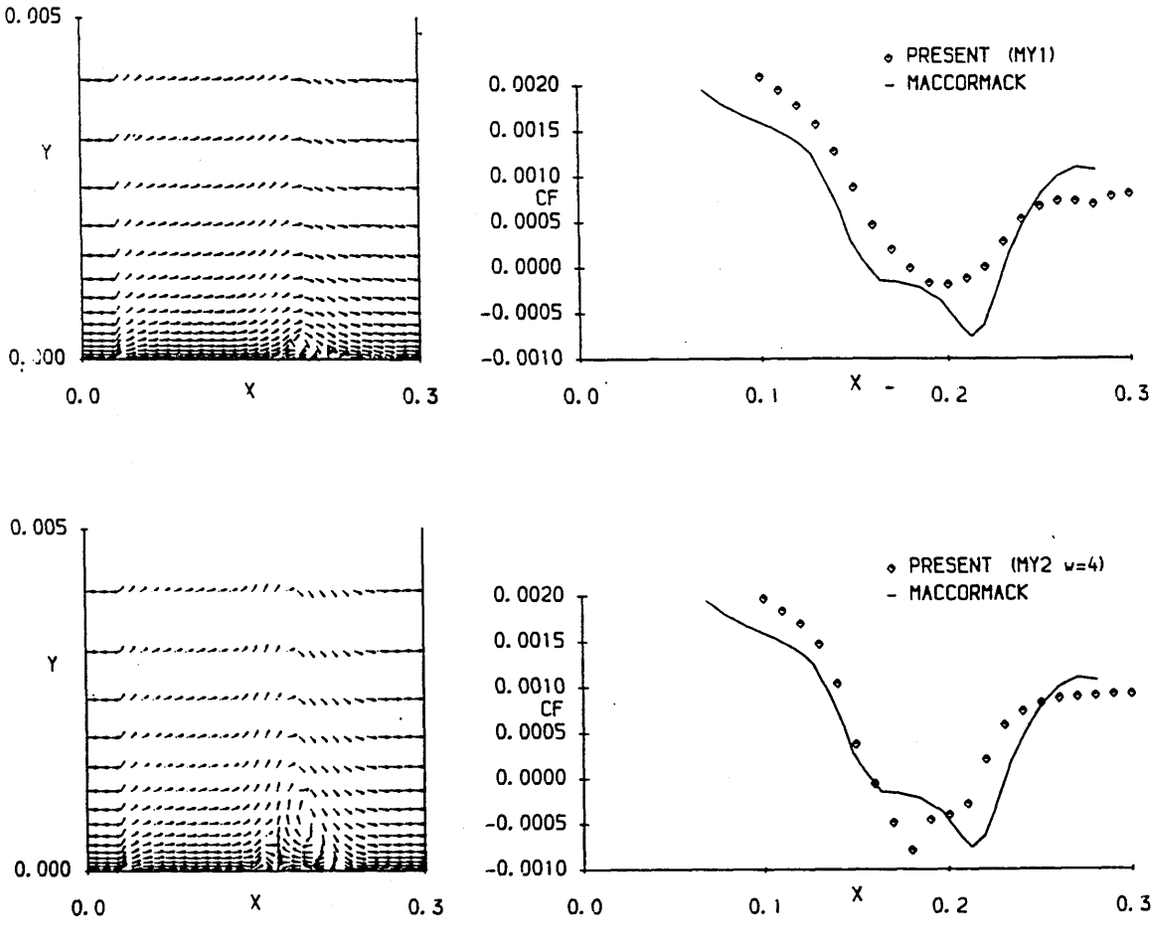

Fig. 3.9 Plots of velocity direction and skin friction coefficient of the modified Yee scheme

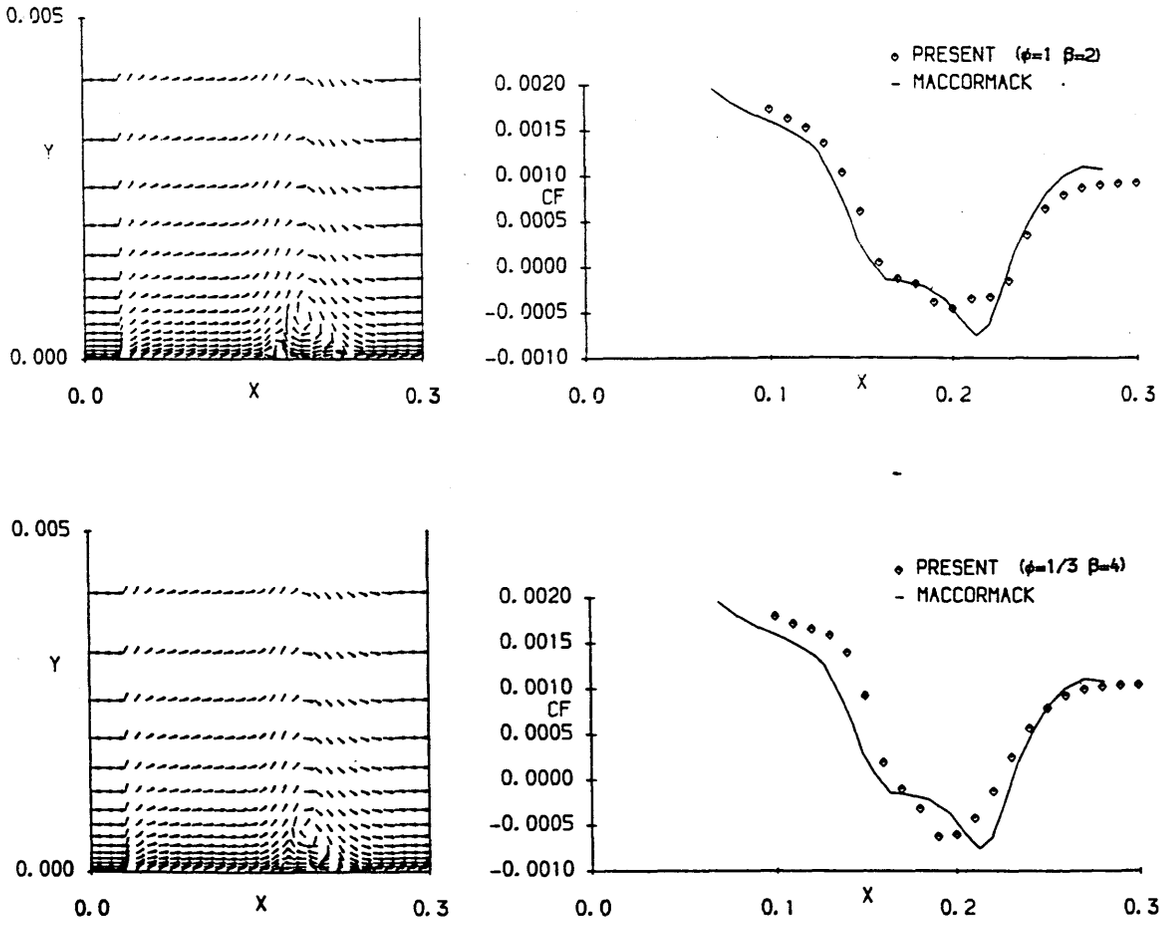

Fig. 3.10 Plots of velocity direction and skin friction coefficient of the Osher-Chakravarthy scheme

resolve the separation very well while the Yee scheme does not. The Y1 limiter gives an unseparated flow pattern. Y2 gives a slightly separated flow, but is not at all satisfactory. It is noticed that limiter MY2 is very promising to attack the viscous flow problem at high Reynolds number. It is much better than limiter MY1. In the test, the same basic computer code is used. Only the inviscid flux subroutine is changed. Thus it seems reasonable to conclude that the Yee scheme does introduce

extra numerical viscosity, and that this viscosity exceeds the physical viscosity such that an unrepresentative result is obtained.

3.6 Conclusions

Although TVD schemes have been applied in the solutions of inviscid flows very successfully, their capacity to resolve viscous shear layers is still quite unclear. By unifying and comparing two TVD schemes, namely the Osher-Chakravarthy and the Yee scheme, it can be concluded that the former is much less dissipative than the latter. Modifications are made to reduce the embedded dissipation in the Yee scheme. The differences in the dissipation pattern among these schemes may not affect the inviscid flow region very much. However, when a viscous solution at high Reynolds number is sought, they could result in dramatically different solutions. This study demonstrates that the dissipation embedded in the schemes may be the cause. When physical dissipation is overwhelmed by numerical dissipation, the solution will be unrepresentative. A 'numerical solution' in this case will be valueless. The goal then is to resolve the problem with the least numerical dissipation possible. The modified Yee scheme is therefore suggested to approach that goal.

CHAPTER 4

AN EFFICIENT EXPLICIT SCHEME FOR MULTI-DIMENSIONAL STEADY FLOW CALCULATION

4.1 Introduction

In the previous chapter, the high-resolution TVD schemes are discussed. In the application of these schemes, it has been found that they are very expensive in processor time because of the splitting of the local characteristics and the TVD mechanism. Therefore, an effort has been made to seek more efficient schemes which have almost the same resolution. This effort has resulted in the preliminary work included in this chapter.

As pointed in Chapter 1, numerical schemes for fluid flow calculations can be divided primarily into two categories, depending on space discretization— central difference schemes and upwind schemes. Generally speaking, central difference schemes are more efficient than upwind schemes due to the fact that the least possible grid points are involved. However, appropriate artificial dissipation needs to be added to achieve stability because they possess very low or even no dissipation. Upwind schemes, though, do have proper embedded dissipation. Therefore they are much more stable than the central difference schemes. However, they suffer more operational counts because more grid points are concerned. In practical applications, therefore, especially in three-dimensional flow calculations, central difference schemes are still widely used because of their low costs.

Numerical schemes contain two different types of time-stepping techniques — explicit or implicit scheme. It is well-known that explicit schemes have restrictions on time step because of the CFL condition. As a result of this fact, usually implicit schemes are preferred in steady state calculations. With the development of computer hardware, the vectorization technique can be applied to the computer-code to greatly speed up the iteration process. It is commonly known that an explicit scheme can be readily vectorized while it is difficult to vectorize an implicit algorithm, if at all possible. A question arises from a consideration of this new environment: is the implicit or explicit scheme more efficient? The answer is not straightforward. Some favour implicit schemes while some others prefer explicit schemes.

In this chapter, a new scheme suitable for steady multi-dimensional flow calculations is proposed. The new scheme is more efficient than the conventional central difference schemes. Explicit time-stepping is employed so the scheme can fully exploit the features of modern computer hardware. The scheme is second-order accurate in the smooth domain while it is first-order at local extrema to suppress oscillations. Preliminary results are shown to demonstrate its accuracy and efficiency.

4.2 Derivation of the First-Order X Scheme

Consider the linear two-dimensional wave equation

$$\frac{\partial u}{\partial t} + a\frac{\partial u}{\partial x} + b\frac{\partial u}{\partial y} = 0 \qquad (4.1)$$

where a>0, b>0. Suppose

$$\mathbf{l} = a\mathbf{i}+b\mathbf{j}=c\mathbf{l}^0=c(\cos\alpha\mathbf{i}+\sin\alpha\mathbf{j}) \tag{4.2}$$

where **i** and **j** are unit vectors in the x and y direction respectively, and $|\mathbf{l}^0|=1$, $\cos\alpha=a/c$, and $c=(a^2+b^2)^{1/2}$. Obviously

$$\text{grad}(u)=\frac{\partial u}{\partial x}\mathbf{i}+\frac{\partial u}{\partial y}\mathbf{j} \tag{4.3}$$

Then (4.1) becomes

$$\frac{\partial u}{\partial t}+c\mathbf{l}^0\cdot\text{grad}(u)=0$$

or

$$\frac{\partial u}{\partial t}+c\frac{\partial u}{\partial l}=0 \tag{4.4}$$

This equation describes a wave propagating in direction **l** with speed c. Now we use this principle to obtain the first-order scheme.

Consider a uniform grid with $\Delta x=\Delta y=h$ in Fig. 4.1. The stencil (E,W,C,N,S) is used to construct conventional schemes, whereas the stencil (NE,SE,C,NW,SW) is utilized to build our new scheme. For descriptive convenience, the new scheme will be called the X scheme, and conventional schemes will be called + schemes in the following text. It is assumed that at time t, the solution in the whole domain is known. Now the solution at time $t+\Delta t$ needs to be determined. We trace along the minus **l** direction to P, with $|CP|=c\Delta t$ and from the earlier stated principle, it is known that

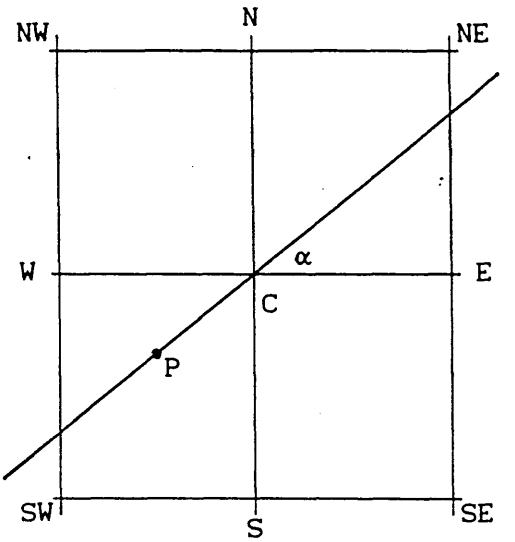

Fig. 4.1 Grid points diagram

$$u_c^{t+\Delta t}=u_P^t \tag{4.5}$$

Hence it is now required to decide u_P^t. Assuming a>b, it is obvious that $\alpha<45^\circ$. Linear interpolation is used in the triangle ΔC-NW-SW. Simple algebraic derivation leads to the following formula

$$u_p=u_c+\frac{\Delta t}{2h}\left[(a+b)(u_{SW}-u_c)+(a-b)(u_{NW}-u_c)\right] \tag{4.6}$$

If it is assumed that P must lie in ΔC-NW-SW, the following condition is obtained

$$\Delta t\le\frac{h}{a}=\frac{h}{\max(a,b)} \tag{4.7}$$

It will be shown later that this is also the stability condition for the scheme (4.6). If we are only concerned with the space difference, the following half-discretized scheme can be obtained

$$\frac{\partial u}{\partial t} = -\frac{1}{2h}[(a+b)(u_c-u_{SW})+(a-b)(u_c-u_{NW})] \tag{4.8}$$

It is found that the modified equation for (4.8) is

$$\frac{\partial u}{\partial t} = -a\frac{\partial u}{\partial x} -b\frac{\partial u}{\partial y}+\frac{1}{2}ah\frac{\partial^2 u}{\partial x^2}+\frac{1}{2}ah\frac{\partial^2 u}{\partial y^2}+bh\frac{\partial^2 u}{\partial x\partial y}+O(h^2) \tag{4.9}$$

Using exactly the same approach, the first-order + scheme is found to be

$$\frac{\partial u}{\partial t} = -\frac{1}{h}[a(u_c-u_w)+b(u_c-u_s)] \tag{4.10}$$

It is actually the well-known first-order upwind scheme. Its modified equation is

$$\frac{\partial u}{\partial t}=-a\frac{\partial u}{\partial x}-b\frac{\partial u}{\partial y}+\frac{1}{2}ah\frac{\partial^2 u}{\partial x^2}+\frac{1}{2}bh\frac{\partial^2 u}{\partial y^2}+O(h^2) \tag{4.11}$$

It is noticed that both these first-order schemes have the same order of accuracy of O(h).

4.3 Accuracy and Stability Analysis

4.3.1 Accuracy Analysis

The question arises as to which of the + scheme or the the X scheme is more accurate. From the modified equations it is known that the first-order X scheme has the same order of truncation error as the first order + scheme (that is exactly what the order of accuracy means). We need to make detailed comparison between the truncation errors of both schemes to decide which one is more accurate.

For both X and + first order schemes, when the steady state solution is obtained, it should satisfy

$$-a\frac{\partial u}{\partial x} - b\frac{\partial u}{\partial y} = 0+O(h) \tag{4.12}$$

The following formulae can be easily obtained from (4.12)

$$\frac{\partial^2 u}{\partial x \partial y} = -\frac{a}{b}\frac{\partial^2 u}{\partial x^2}+O(h) \tag{4.13}$$

$$\frac{\partial^2 u}{\partial y^2} = \frac{a^2}{b^2}\frac{\partial^2 u}{\partial x^2}+O(h) \tag{4.14}$$

Substituting (4.13) and (4.14) into (4.8), noticing that at steady-state, $\frac{\partial u}{\partial t} = 0$, we get the following modified equation for (4.8).

$$-a\frac{\partial u}{\partial x} -b\frac{\partial u}{\partial y}+\frac{1}{2}ah(\frac{a^2}{b^2} -1)\frac{\partial^2 u}{\partial x^2} = 0+O(h^2) \tag{4.15}$$

Substituting (4.13) and (4.14) into (4.11), we get the following modified equation for (4.11).

$$-a\frac{\partial u}{\partial x} -b\frac{\partial u}{\partial y}+\frac{1}{2}ah(\frac{a}{b}+1)\frac{\partial^2 u}{\partial x^2} = 0+O(h^2) \tag{4.16}$$

From (4.15) and (4.16), it is obvious that a first-order dissipation term is embedded in both the x and + schemes.

When $$1+\frac{a}{b} = \frac{a^2}{b^2} -1 \quad \text{or} \quad \frac{a}{b} = 2 \tag{4.17}$$

the X scheme has the same amount of dissipation as the + scheme. Almost

identical results would derive from (4.8) and (4.10). If $1 \le a/b \le 2$, the X scheme has less dissipation than + scheme, in other words, it is more accurate. In fact if $a/b=1$, the modified equation of the X scheme would be

$$-a\frac{\partial u}{\partial x} - b\frac{\partial u}{\partial y} = 0 \tag{4.18}$$

This is the exact differential equation and the X scheme would thus recover the exact solution of (4.1). If $a/b>2$, the X scheme has more dissipation than the + scheme, and thus it is less accurate than the + scheme.

4.3.2 Stability Analysis

Up to now we still have not explained why in the first place we want to use this X scheme, and what the advantages are of using the X scheme instead of the conventional + scheme. From the accuracy analysis, it is clear that the two first order schemes have the same order of accuracy although the amplitudes of the truncation errors are different. In some situations, the X scheme is more accurate than the + scheme, and vice versa. Now we come to the point to justify our motivation to utilize the X scheme.

Here we again consider the uniform grid in Fig. 4.2. We claim that the X scheme needs only half the points of a conventional grid in the calculation. In Fig. 4.2 grid A is required for the + scheme, while grid B is employed for the X scheme. When a steady state solution is achieved, the accuracy of the solution on grid B may be as good as that on

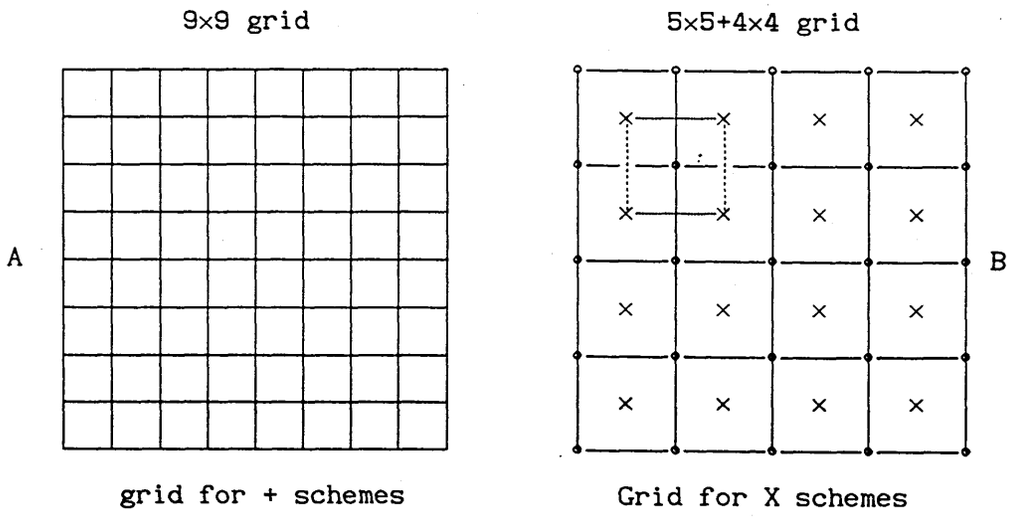

Fig. 4.2 Different grids

grid A. However, only half of the grid points are used to achieve that accuracy. This alone reduces the computational effort by half. In addition, if the solutions at points "∘" are known at time level n, only the solutions at points "×" need to be calculated at time level n+1. This cuts the amount of calculation by another half. Therefore the X scheme is expected to have far less operational counts than the + scheme. If somehow the limit $1/2 \le |a/b| \le 2$ is retained, results utilizing the first-order X scheme are at least as accurate as those using the first-order + scheme. Numerical experiments do need to compare the overall accuracy between them for the limit $0 < |a/b| < \infty$. Preliminary results appear to favour the X scheme when both accuracy and efficiency are considered.

In the following discussion, indices i, j are employed to denote grid points in the x and y direction respectively. As a result of the stencil used in the implementation of the X scheme, it is seen that at one time level only one "layer" of the solution in the whole domain is available,

either the layer "×", or the layer "∘". Hence the time stepping is a three level procedure. Since our interest is in the the steady state solution only, this approach does not at all affect the final solution. The first-order X schemes can be expressed as follows:

$$u_{i,j}^{n+1}=u_{i,j}^{n-1}-\frac{\Delta t}{h}\left[(a+b)(u_{i,j}^{n-1}-u_{i-1,j-1}^{n})+(a-b)(u_{i,j}^{n-1}-u_{i-1,j+1}^{n})\right] \tag{4.19}$$

This scheme is second order accurate in time. Assume that the numerical scheme has the solution

$$u_{i,j}^{n}=G^{n}e^{i(lx+my)} \tag{4.20}$$

where $i=\sqrt{-1}$, l and m are wave numbers and G is the amplification factor, and that at time $(n+1)\Delta t$, the solution is

$$u_{i,j}^{n+1}=Gu_{i,j}^{n} \tag{4.21}$$

Substituting (4.20) and (4.21) into (4.19), the following expression

$$G=\frac{1}{G}(1-2\lambda a)+\lambda(a+b)(\cos\alpha-i\sin\alpha)+\lambda(a-b)(\cos\beta-i\sin\beta) \tag{4.22}$$

is obtained. Where $\alpha=lh+mh$, $\beta=lh-mh$ and $\lambda=\Delta t/h$. At present it is still not possible to develop a stability condition from this formula. However, another approach is used to analyze the following two-level scheme

$$u_{i,j}^{n+1}=u_{i,j}^{n}-\frac{\Delta t}{2h}\left[(a+b)(u_{i,j}^{n}-u_{i-1,j-1}^{n})+(a-b)(u_{i,j}^{n}-u_{i-1,j+1}^{n})\right] \tag{4.23}$$

Now the amplification factor is

$$G=1+\frac{\lambda}{2}\left[(a+b)(e^{-il h-imh}-1)+(a-b)(e^{-il h+imh}-1)\right]$$

$$=1-\lambda a+\frac{\lambda}{2}\left[(a+b)\cos\alpha+(a-b)\cos\beta\right]$$

$$-\frac{\lambda}{2}i\left[(a+b)\sin\alpha+(a-b)\sin\beta\right] \qquad (4.24)$$

Then from (4.24),

$$|G|^2=1+\lambda^2a^2-2\lambda a+\frac{\lambda^2}{2}(a^2+b^2)+\frac{\lambda^2}{2}(a^2-b^2)\cos(\alpha-\beta)$$

$$+\lambda(1-\lambda a)[(a+b)\cos\alpha+(a-b)\cos\beta]$$

If it is assumed that

$$\lambda a>1 \text{ and } \alpha=\pi/2 \quad \beta=\pi/2$$

then

$$|G|^2=1+\lambda^2a^2-2\lambda a+\lambda^2a^2=1+2\lambda a(\lambda a-1)>1$$

i.e., the scheme is unstable. If we suppose $\lambda a\leq 1$, then

$$|G|^2\leq 1+\lambda^2a^2-2\lambda a+\lambda^2a^2+2a\lambda(1-\lambda a)=1$$

This means that the scheme is stable if

$$\lambda a\leq 1 \quad \text{or} \quad \Delta t\leq\frac{h}{a} \qquad (4.25)$$

Numerical tests suggested that (4.19) has the same stability condition as this two-level scheme analysis, i.e.,

$$\lambda \le \frac{1}{\max(a,b)}$$

The first-order + scheme can be put as

$$u^{n+1}_{i,j}=u^{n}_{i,j}-\frac{\Delta t}{h}a(u^{n}_{i,j}-u^{n}_{i-1,j})-\frac{\Delta t}{h}b(u^{n}_{i,j}-u^{n}_{i,j-1}) \qquad (4.26)$$

The amplification factor G is

$$G=1-\lambda a-\lambda b+\lambda a\cos(\varphi)+\lambda b\cos(\vartheta)-i[\lambda a\sin(\varphi)+\lambda b\sin(\vartheta)] \qquad (4.27)$$

where $\varphi=lh$ and $\vartheta=mh$. Supposing

$$a+b=d \qquad a-b=c \qquad (4.28a)$$

then

$$a=\frac{d+c}{2} \qquad c=\frac{d-c}{2} \qquad (4.28b)$$

Substituting (4.28) into (4.27), the following is obtained

$$G=1-\lambda d+\frac{\lambda}{2}\left[(d+c)\cos\varphi+(d-c)\cos\vartheta\right]$$

$$-\frac{\lambda}{2}i\left[(d+c)\sin\varphi+(d-c)\sin\vartheta\right] \qquad (4.29)$$

Comparing (4.29) with (4.24), it is seen that the stability condition for (4.26) is $\lambda d\le 1$, i.e.,

$$\lambda(a+b)\le 1 \qquad \text{or} \qquad \Delta t\le\frac{h}{a+b} \qquad (4.30)$$

Comparing the stability conditions of both schemes, it is easy to see that the X scheme can have larger time-steps than the + scheme for the same grid interval h.

It is interesting to include the "central difference" second-order X scheme in the discussion. The scheme can be expressed as

$$u_{i,j}^{n+1}=u_{i,j}^{n-1}-\frac{\Delta t}{2h}\Big[a(u_{i+1,j+1}^{n}+u_{i+1,j-1}^{n}-u_{i-1,j+1}^{n}-u_{i-1,j-1}^{n})+$$

$$b(u_{i+1,j+1}^{n}+u_{i-1,j+1}^{n}-u_{i+1,j-1}^{n}-u_{i-1,j-1}^{n})\Big] \qquad (4.31)$$

The amplification factor of (4.31) is

$$G=\frac{1}{G}-i\lambda[(a+b)\sin\alpha+(a-b)\sin\beta)) \qquad (4.32)$$

If we put

$$A=\lambda[(a+b)\sin\alpha+(a-b)\sin\beta]$$

then

$$G=\left[-Ai\pm\sqrt{-A^2+4}\right]/2 \qquad (4.33)$$

providing $|A|\leq 2$. That means

$$|\lambda[(a+b)\sin\alpha+(a-b)\sin\beta]|\leq 2$$

But

$$|\lambda[(a+b)\sin\alpha+(a-b)\sin\beta]|\leq\lambda|a+b|+\lambda|a-b|=2\lambda\max(|a|,|b|)$$

Thus if

$$2\lambda\max(|a|,|b|)\leq 2 \quad \text{or} \quad \lambda\leq 1/\max(|a|,|b|) \tag{4.34}$$

then formula (4.33) is correct. In this case

$$|G|=1$$

No dissipation is embedded in the scheme. However it is stable similar to the leapfrog scheme. This analysis is fully demonstrated by the central difference second-order X scheme result shown in Fig. 4.7.

4.4 Extension of the First-Order X Scheme to High Order

From the stability analysis of the second-order central difference X scheme, one sees that there is no embedded dissipation. Hence dissipation terms should be added to damp unwanted error modes. However, if the dissipation is too much, the accuracy of the solution is deteriorated. To do no damage to the accuracy while at the same time maintaining a good damping capability, only high-order dissipation terms can be added. The TVD schemes have suggested a guideline on how the numerical viscosity should be included in the scheme. At local extrema, high-order TVD schemes are only of first-order accuracy to damp the possible oscillation. In the smooth domain, the high-order accuracy is restored. In fact, the first-order X scheme can be written as a second-order scheme plus a dissipation term. If we use u_{1st} and u_{2nd} to denote the first and

second-order accurate X scheme respectively, then the following scheme is obtained.

$$\left[u_{i,j}^{n+1}\right]_{1st}=\left[u_{i,j}^{n+1}\right]_{2nd}+\frac{\Delta t}{4h}\Big[|a+b|(u_{i+1,j+1}^{n}+u_{i-1,j-1}^{n}-2u_{i,j}^{n-1}) +|a-b|(u_{i+1,j-1}^{n}+u_{i-1,j+1}^{n}-2u_{i,j}^{n-1})\Big] \tag{4.35}$$

where a and b are any real numbers. From (4.35), the following high order X scheme is suggested

$$\left[u_{i,j}^{n+1}\right]_{h}=\left[u_{i,j}^{n+1}\right]_{2nd}+\frac{\Delta t}{4h}\Big[\omega_1|a+b|(u_{i+1,j+1}^{n}+u_{i-1,j-1}^{n}-2u_{i,j}^{n-1}) +\omega_2|a-b|(u_{i+1,j-1}^{n}+u_{i-1,j+1}^{n}-2u_{i,j}^{n-1})\Big] \tag{4.36}$$

where

$$\omega_1=\omega(r_1) \qquad \omega_2=\omega(r_2)$$

and

$$\omega(r)=1-\frac{|r|+r}{1+r^2} \tag{4.37a}$$

with

$$r_1=\frac{u_{i+1,j+1}-u_{i,j}}{u_{i,j}-u_{i-1,j-1}} \qquad r_2=\frac{u_{i+1,j-1}-u_{i,j}}{u_{i,j}-u_{i-1,j+1}} \tag{4.37b}$$

It is obvious that at local extrema,

$$r_1<0 \qquad r_2<0 \qquad \text{then} \qquad \omega_1=\omega_2=1$$

Eq.(4.36) represents the exact first-order scheme. However in the smooth domain

$$r_1=\frac{u_{i+1,j+1}-u_{i,j}}{u_{i,j}-u_{i-1,j-1}}=1+\frac{u_{i+1,j+1}-2u_{i,j}+u_{i-1,j-1}}{u_{i,j}-u_{i-1,j-1}}=1+O(h)$$

$$\omega_1=1-\frac{2r_1}{1+r_1^2}=\frac{(1-r_1)^2}{(1+r_1)^2}=O(h^2) \tag{4.38a}$$

For the same reason, we have

$$\omega_2=O(h^2) \tag{4.38b}$$

From (4.38) and (4.36), it is obvious that the added dissipation is actually a fourth-order term. Scheme (4.36) is still second-order accurate in the smooth region. It is found, through numerical tests, that the new high-order X scheme has the same stability condition as the first order X scheme.

4.5 Extension of the X Scheme to System of Equations

First we consider the extension of the X scheme to a constant coefficient system, i.e.,

$$\frac{\partial \mathbf{U}}{\partial t}+\frac{\partial \mathbf{E}}{\partial x}+\frac{\partial \mathbf{F}}{\partial y}=\frac{\partial \mathbf{U}}{\partial t}+A\frac{\partial \mathbf{U}}{\partial x}+B\frac{\partial \mathbf{U}}{\partial y}=0 \tag{4.39}$$

where $\mathbf{U},\mathbf{E},\mathbf{F}$ are column vectors of m components, $A=\partial \mathbf{E}/\partial \mathbf{U}$ and $B=\partial \mathbf{F}/\partial \mathbf{U}$ are

m×m matrices and are both constant. It is assumed that A and B have real eigenvalues a^1 and b^1 and they can be expressed as

$$A = R_a \, \mathrm{diag}(a^1) \, R_a^{-1} \tag{4.40}$$

$$B = R_b \, \mathrm{diag}(b^1) \, R_b^{-1} \tag{4.41}$$

where R and R^{-1} are composed of columns of right eigenvectors and rows of left eigenvectors of the corresponding matrices. If somehow $R_a=R_b$, and $\mathbf{w}=R_a^{-1}\mathbf{U}$, then Eq.(4.39) decouples into m scalar equations for the characteristic variables

$$\frac{\partial w^1}{\partial t} + a^1\frac{\partial w^1}{\partial x} + b^1\frac{\partial w^1}{\partial y}=0 \tag{4.42}$$

In this case the X scheme can be directly applied to the scalar equations. However, usually $R_a \neq R_b$. That means Eq.(4.39) cannot decouple into (4.42). Hence other approaches have to be found. Here we present our procedure as follows. Let $\bar{a}$ and $\bar{b}$ be the average eigenvalues of A and B correspondingly. Then A and B are approximated as

$$A \simeq R_a^{-1}\mathrm{diag}(\bar{a})R_a=\mathrm{diag}(\bar{a})=\bar{a}I \qquad B \simeq R_b^{-1}\mathrm{diag}(\bar{b})R_b=\mathrm{diag}(\bar{b})=\bar{b}I \tag{4.43}$$

and the X scheme is now written as

$$U^{n+1}_{i,j}=U^{n-1}_{i,j}-\frac{\Delta t}{2h}(E^{n}_{i+1,j+1}+E^{n}_{i+1,j-1}-E^{n}_{i-1,j+1}-E^{n}_{i-1,j-1})$$

$$-\frac{\Delta t}{2h}(F^{n}_{i+1,j+1}+F^{n}_{i-1,j+1}-F^{n}_{i+1,j-1}-F^{n}_{i-1,j-1})$$

$$+\frac{\Delta t}{4h}\Big[|\bar{a}+\bar{b}|\Omega_1(U^{n}_{i+1,j+1}+U^{n}_{i-1,j-1}-2U^{n-1}_{i,j})$$

$$+|\bar{a}-\bar{b}|\Omega_2(U^{n}_{i+1,j-1}+U^{n}_{i-1,j+1}-2U^{n-1}_{i,j})\Big] \qquad (4.44)$$

where Ω_1 and Ω_2 are row vectors whose components are $\omega_1^{\,1}$ and $\omega_2^{\,1}$ respectively which are determined by

$$\omega_1^{\,1}=\omega(r_1^{\,1}) \qquad \omega_2^{\,1}=\omega(r_2^{\,1}) \qquad (4.45)$$

and

$$r_1^{\,1}=\frac{U^{1}_{i+1,j+1}-U^{1}_{i,j}}{U^{1}_{i,j}-U^{1}_{i-1,j-1}} \qquad r_2^{\,1}=\frac{U^{1}_{i+1,j-1}-U^{1}_{i,j}}{U^{1}_{i,j}-U^{1}_{i-1,j+1}} \qquad (4.46a)$$

$$\omega(r)=1-\frac{|r|+r}{1+r^2} \qquad (4.46b)$$

Extension of the X scheme to a nonlinear system of the conservation laws is implemented by the so-called "locally frozen" technique. For example, if A and B are not constant in (4.39), then $A_{i,j}$ and $B_{i,j}$ are used when the solution in point (i,j) is sought.

4.6 Numerical Results and Discussions

A variety of numerical experiments have been carried out to compare

the performance of the X and + schemes. In all of the following calculations, the initial conditions are the same. After each iteration, the L_2 norm of the residual of the solution is calculated. The work unit represents the CPU time used in the calculation. A prescribed CFL=0.9 is used throughout to enable valid comparisons. The first two cases are chosen from [31]. The numerical experimental results are presented below.

4.6.1 The first test case is the solution of (4.1) on the square $[0,1]\times[0,1]$ with $a=\cos\varphi$ and $b=\sin\varphi$, here $\varphi\in[0,\pi/4]$. The boundary conditions are as follows

$$\begin{cases} u(0,y)=0 & 0\le y\le 1 \\ u(x,0)=1 & 0\le x\le 1 \end{cases} \tag{4.47}$$

The exact solution of the steady-state problem consists of a contact discontinuity in the direction $(\cos\varphi,\sin\varphi)$. Different φ leads to a different a/b. For the first-order + scheme, a 65x65 grid is used. For the first order X schemes, a variety of different grids are tested, i.e., a. 33x33+32x32 grid. b. 47x47+46x46 grid. c. 65x65+64x64 grid. The solutions and the convergence histories are shown in Figs. 4.3-4.6. It is obvious that results using the first order X scheme are more accurate than those using the first order + scheme when a/b<2 and the X scheme is at least four times more efficient than the + scheme providing grid a is employed for the X scheme. When grid c is used, it takes almost the same amount of time to obtain a converged solution using the first order X scheme as that using the first order + scheme. This solution is more accurate than the corresponding + scheme solution up to a/b=3. The solution using the high order X scheme is displayed in the same figures. It takes much more time to achieve convergence because this scheme

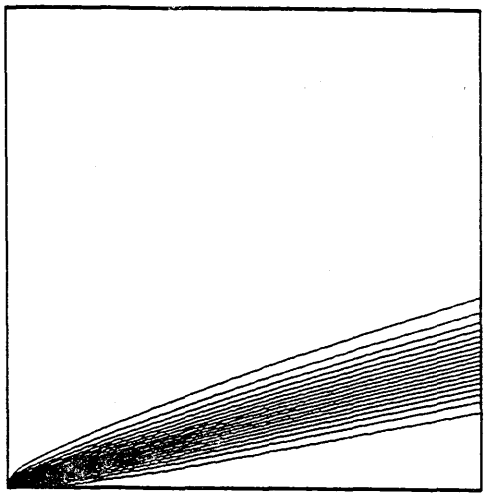

First order scheme on 65X65 grid

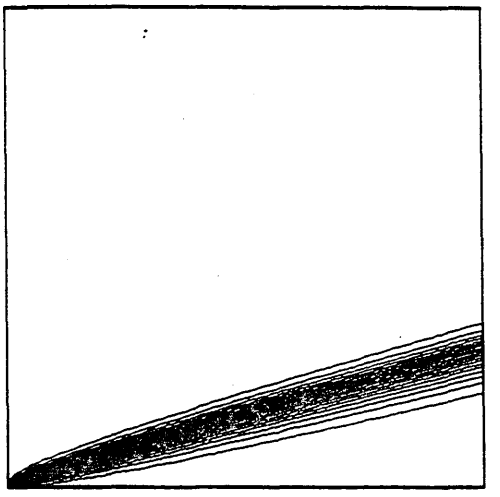

TVD scheme on 65X65 grid

Grid 33x33+32x32

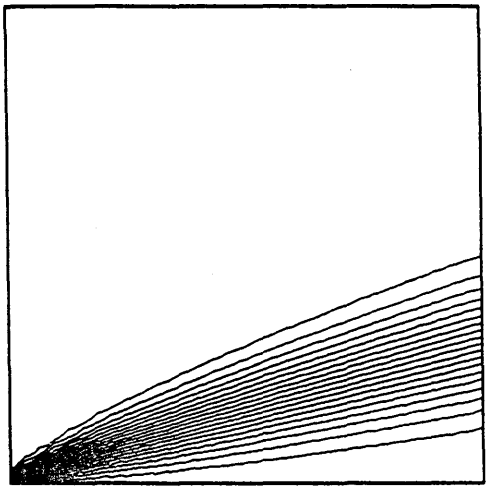

First-order X scheme

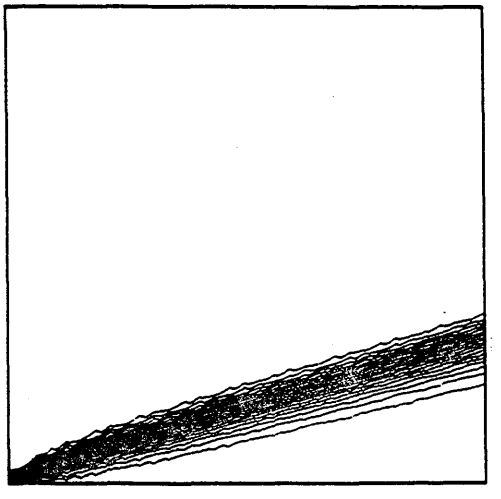

High-order X scheme

Fig. 4.3 The solutions with a/b=ctan(alf)

alf=15 degrees

Grid 65X65

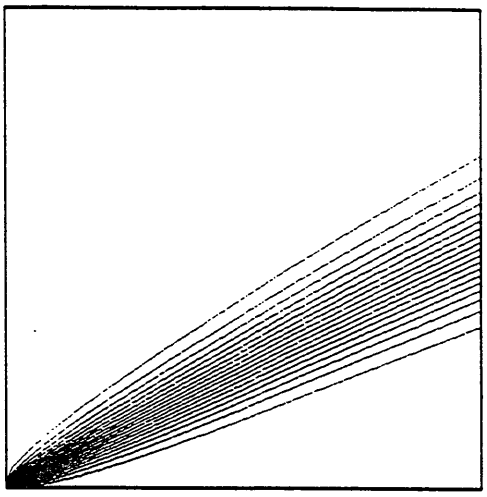

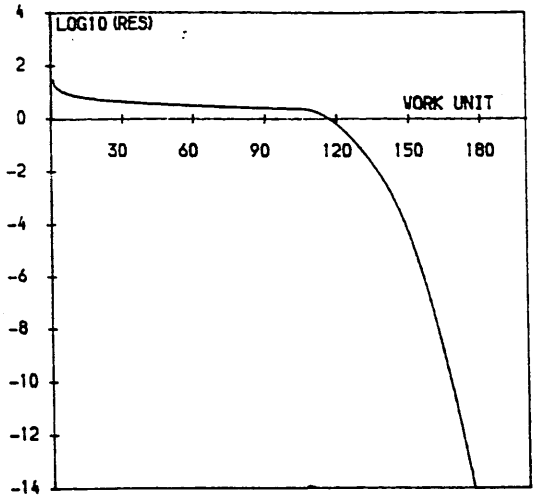

First-order + scheme

Grid 33x33+32x32

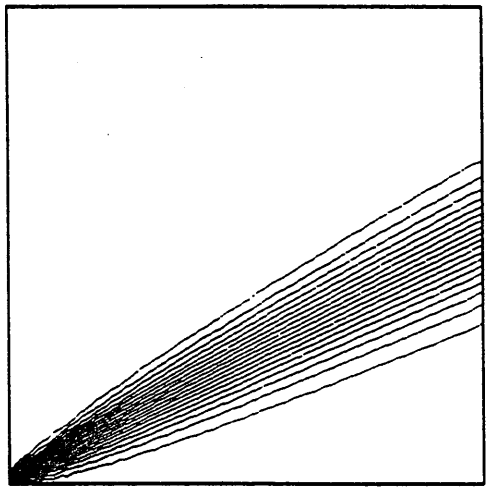

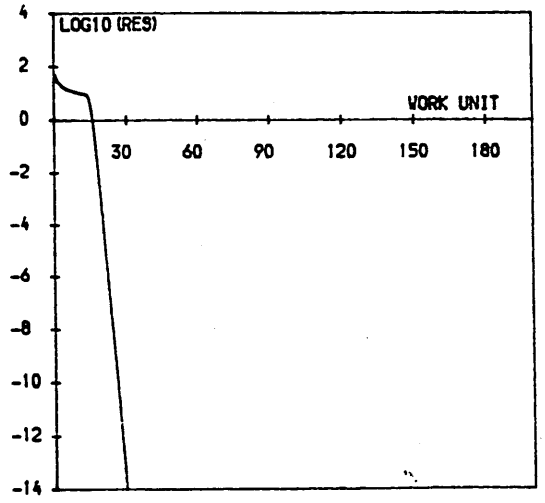

first-order X scheme

Fig. 4.4 The solutions and convergence histories with a/b=2

Grid 47x47+46x46

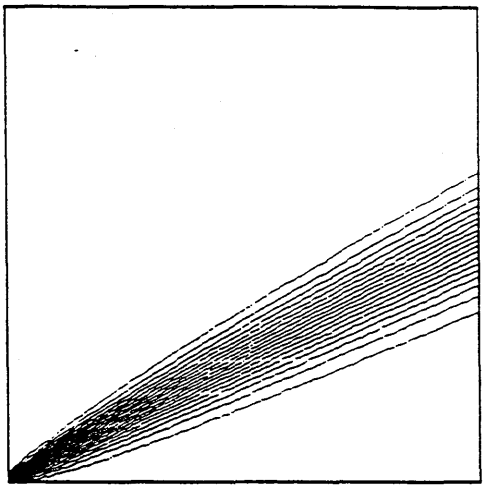

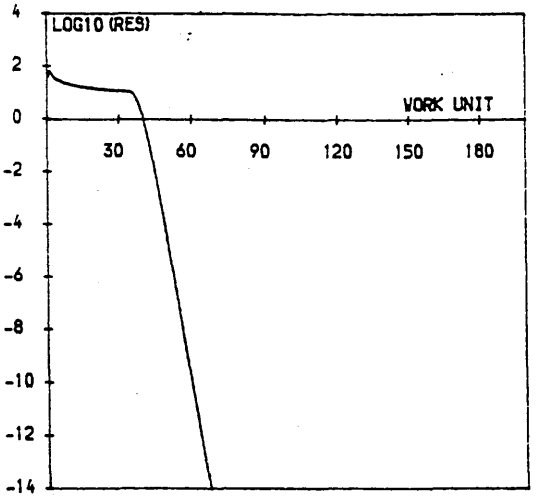

First-order X scheme

Grid 65x65+64x64

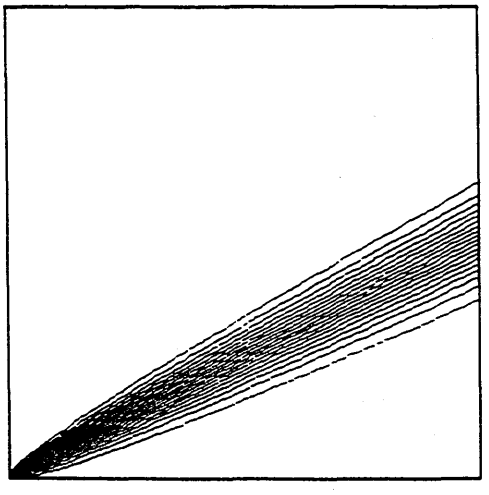

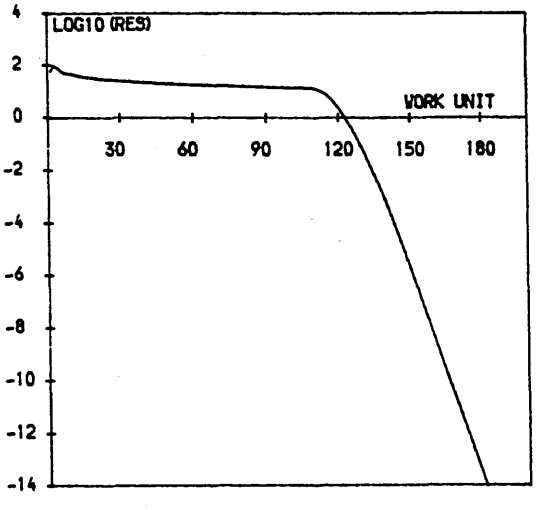

First-order X scheme

Fig. 4.4 Continued

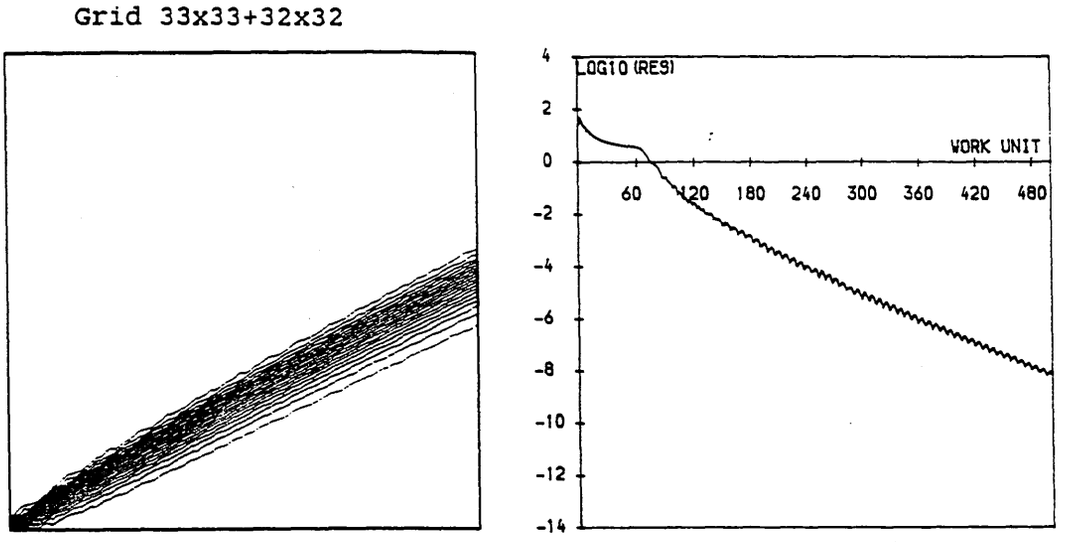

Fig. 4.4 Continued

possesses much less dissipation to damp the unwanted error modes. However, the solution is far more accurate than that of the first order scheme. An interesting phenomenon is noticed by the author. Even if the central difference second-order X scheme possesses no numerical dissipation, a "converged" solution is still possible. Fig. 4.7 shows such a solution for a/b=2. The contact discontinuity can be easily picked up. This fully verifies the stability analysis in section 4.3.2.

4.6.2 The second test case is still a linear wave equation but a and b are now functions of x and y. The governing equation is

$$\frac{\partial u}{\partial t} + y\frac{\partial u}{\partial x} - x\frac{\partial u}{\partial y} = 0 \qquad (4.48)$$

The solution domain is $[-1,1]\times[0,1]$. It is obvious that $|a/b| \in (0,\infty)$.

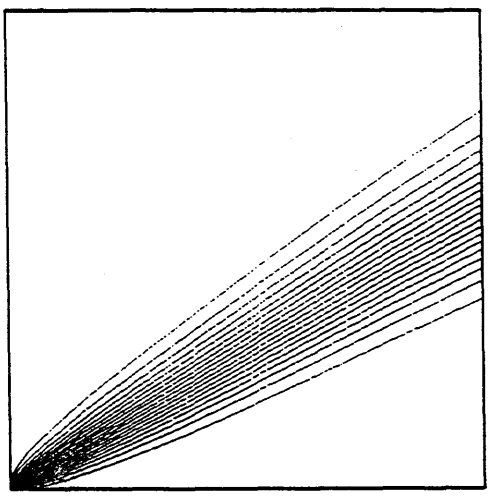

First order scheme on 65X65 grid

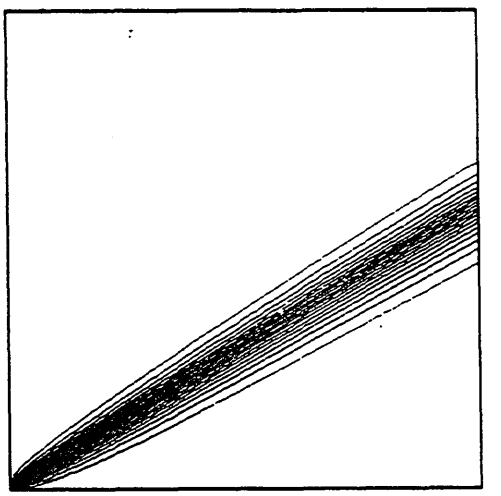

TVD scheme on 65X65 grid

Grid 33x33+32x32

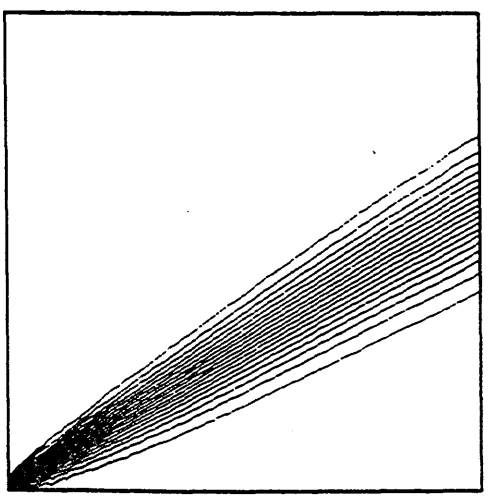

First-order X scheme

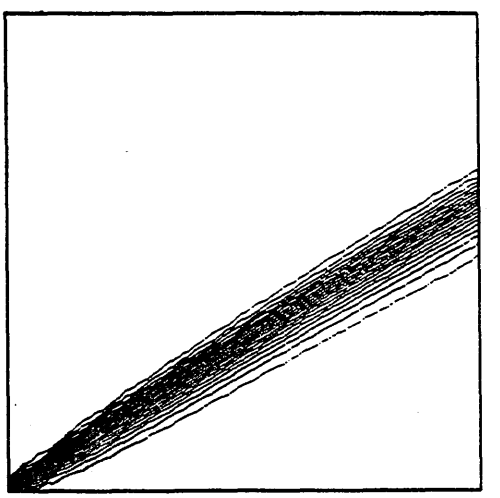

High-order X scheme

Fig. 4.5 The solutions with a/b=ctan(alf)

alf=30 degrees

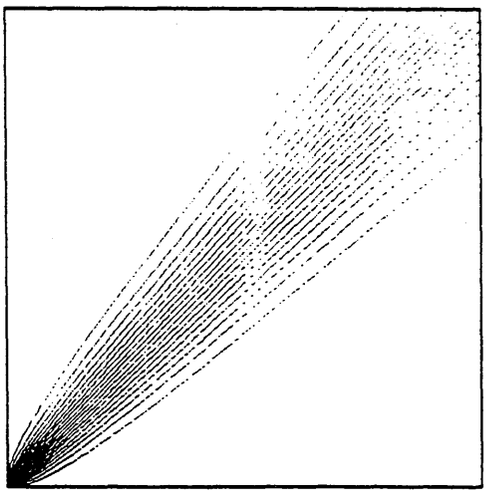

First order scheme on 65X65 grid

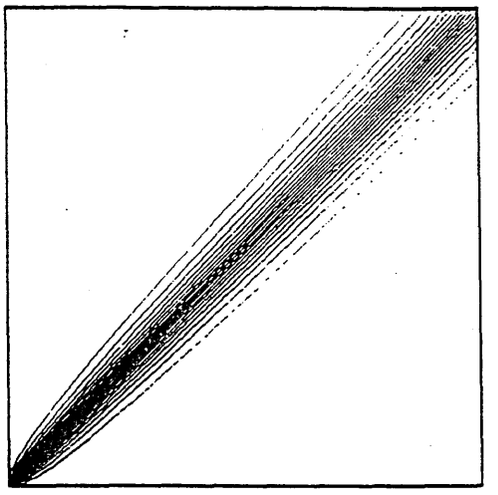

TVD scheme on 65X65 grid

Grid 33x33+32x32

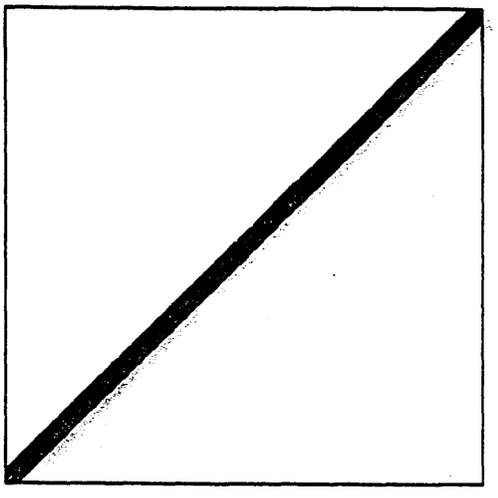

First-order X scheme

Fig. 4.6 The solutions with a/b=1

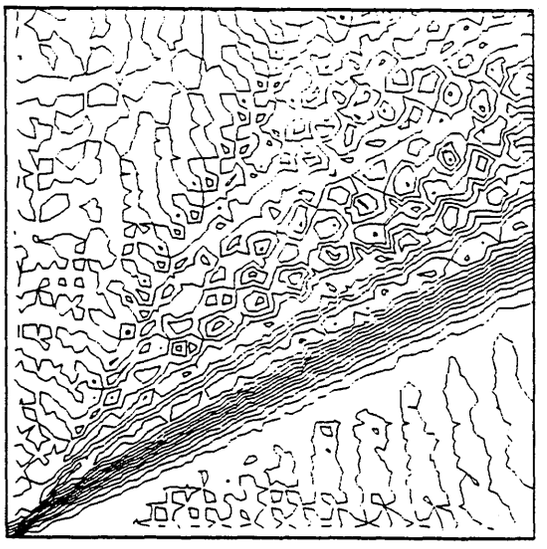

Fig. 4.7 The "steady solution" of the central difference second-order X scheme with a/b=2

Thus this problem is expected to be a good test case to compare the overall accuracy of the first-order X and + schemes. The boundary conditions for the steady state solution are as follows

$$\begin{cases} u(x,0)=0 & x<-0.65 \\ u(x,0)=1 & -0.65<x<-0.35 \\ u(x,0)=0 & -0.35<x<0 \\ u(-1,y)=0 & 0<y<1 \\ u(x,1)=0 & 0<x<1 \end{cases} \tag{4.49}$$

The exact solution is

$$\begin{cases} u(x,y)=1 & \text{if } 0.35<\sqrt{x^2+y^2}<0.65 \\ u(x,y)=0 & \text{otherwise} \end{cases} \tag{4.50}$$

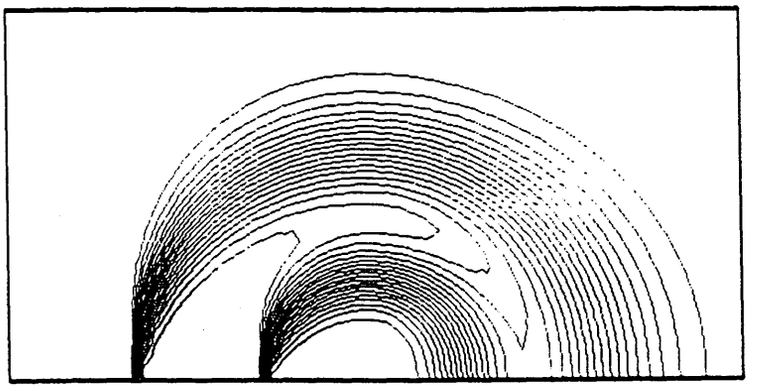

First order scheme on 65X33 grid

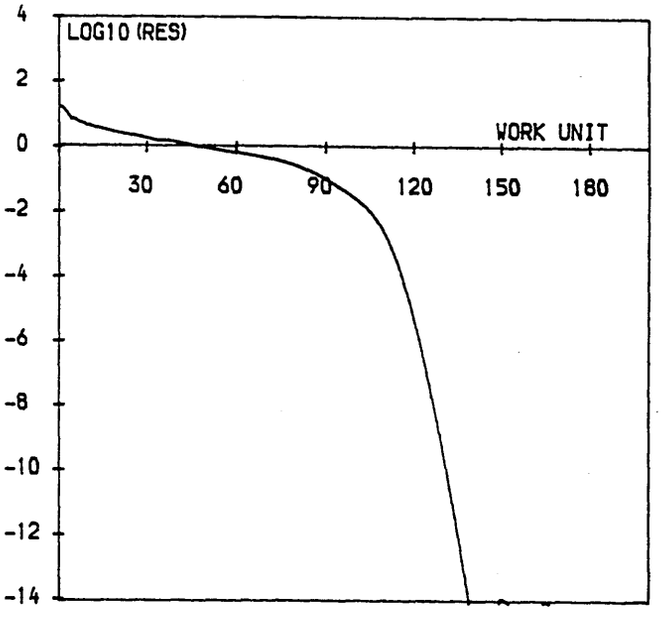

Fig. 4.8 The solution and convergence history of the first order + scheme on grid 65×33

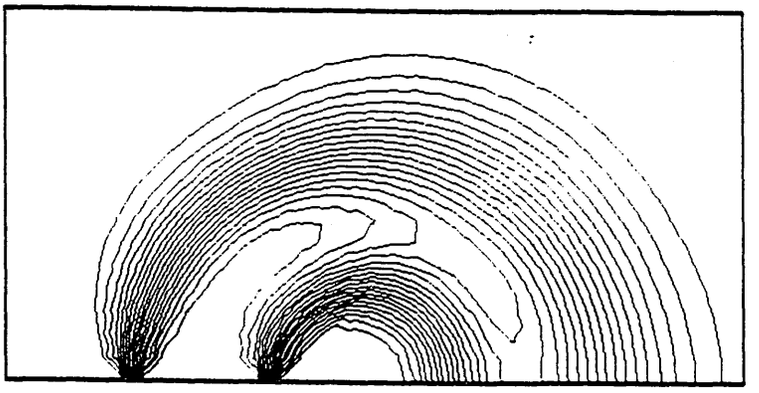

First order "X" scheme on 33x17 grid

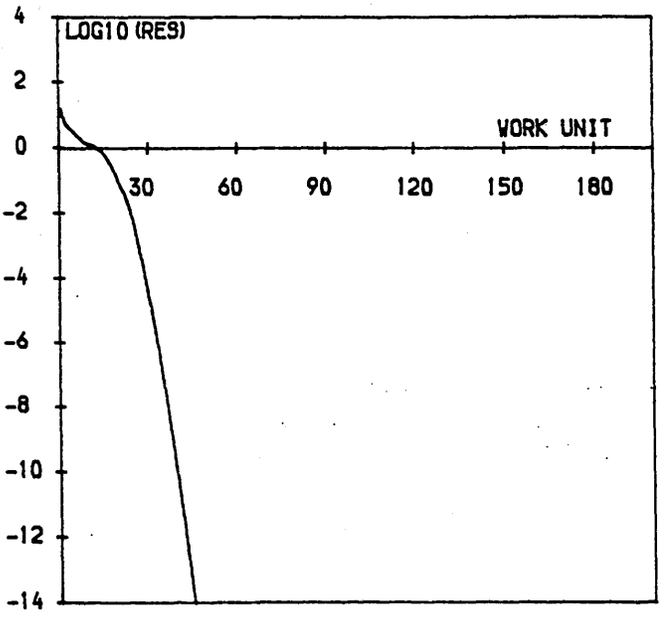

Fig. 4.9 The solution and convergence history of the first order X scheme on grid 33x17+32x16

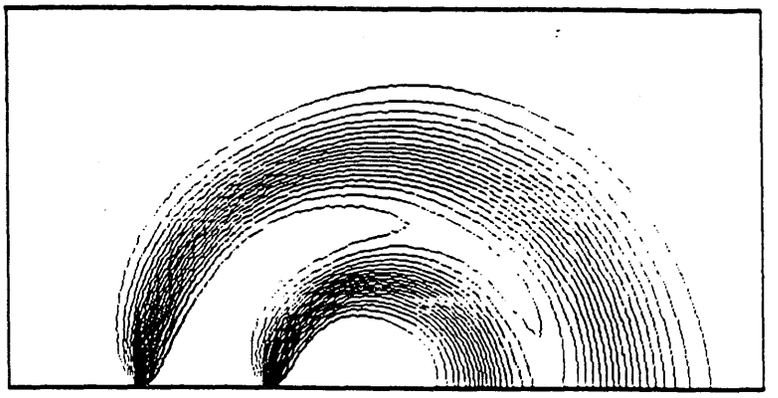

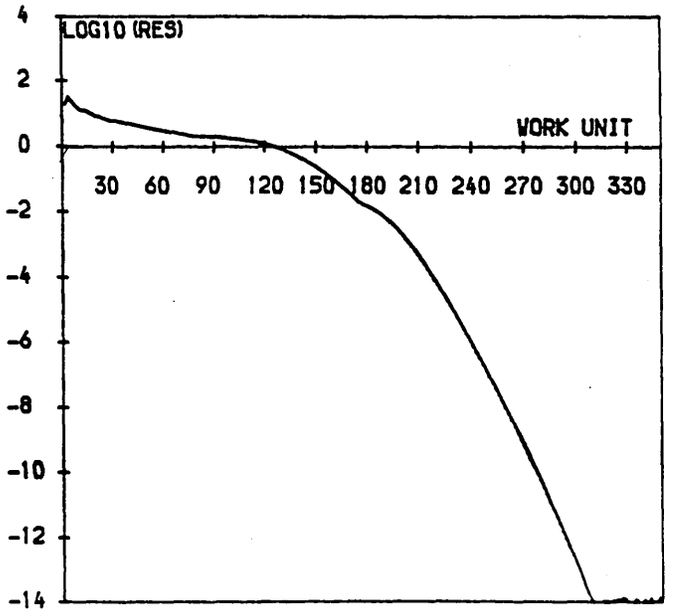

Fig. 4.10 The solution and convergence history of the first order X scheme on grid 65×33+64×32

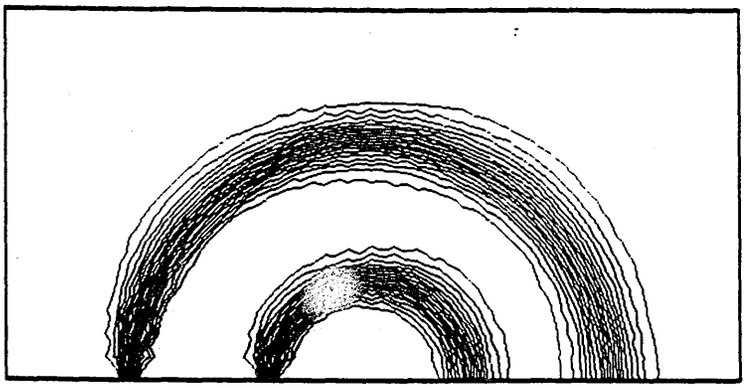

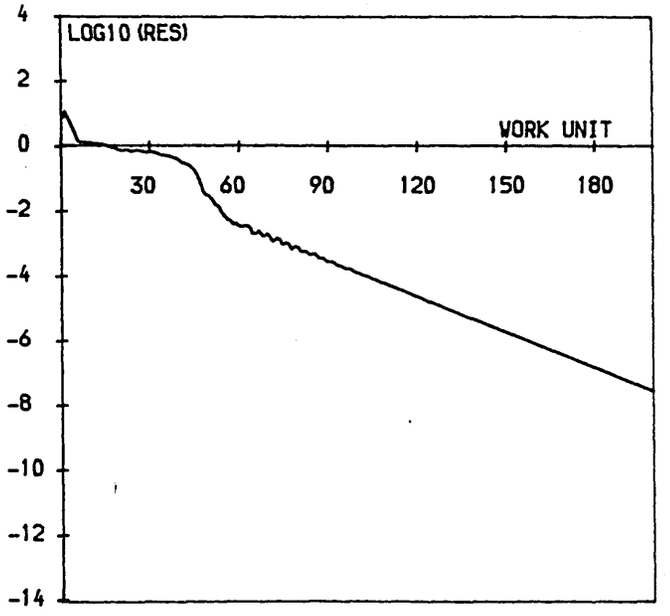

Fig. 4.11 The solution and convergence history of the high-order X scheme on grid 33×17+32×16

For the first-order + scheme, a 65x33 grid is used, and for the X scheme, two grids are tested: a. 33x17+32x16. b. 65x33+64x32. In Figs.4.8-4.11 the computed results and convergence histories are displayed. It is apparent that the first-order X scheme with grid a. leads to a solution of the same level of resolution as the first order + scheme. From the converged solution we see that at places where $|a/b|\to 0$ or ∞, the solution using the + scheme is the most accurate. On the other hand, when $|a/b|\to 1$, the solution using the X scheme is more accurate. The overall accuracy of both schemes is almost the same. Again the solution obtained using the high-order X scheme is as accurate as expected.

4.6.3 In the final test case, a transonic inviscid flow through a channel with a circular arc bump is calculated. The thickness of the bump is 4.2%. The geometry is shown in Fig. 4.12. The flow conditions are $M_{in}=0.85$, and $p_{in}=p_{out}$. Over the bump, the flow in part of the domain is supersonic, and a shock is generated. The result using the modified Yee TVD scheme with limiter MY1 is calculated for comparison. The high-order X scheme is also tested. The results are displayed in Figs. 4.13-4.14. From the solution of the X scheme it can be easily seen that the the position of the shock is a little downstream of that formed from the TVD scheme although the resolution is sufficient. This is due to the fact that the X scheme is not in conservation form. The CPU time used to obtain the X scheme solution is less than quarter of that used by the TVD scheme. Again this case not only fully demonstrated the efficiency, accuracy but also the disadvantage of the X scheme. It can be expected that the X scheme can be fully applied to the solution of supersonic and hypersonic flows with an appropriate shock-fitting technique (e.g. the approach used in [22]).

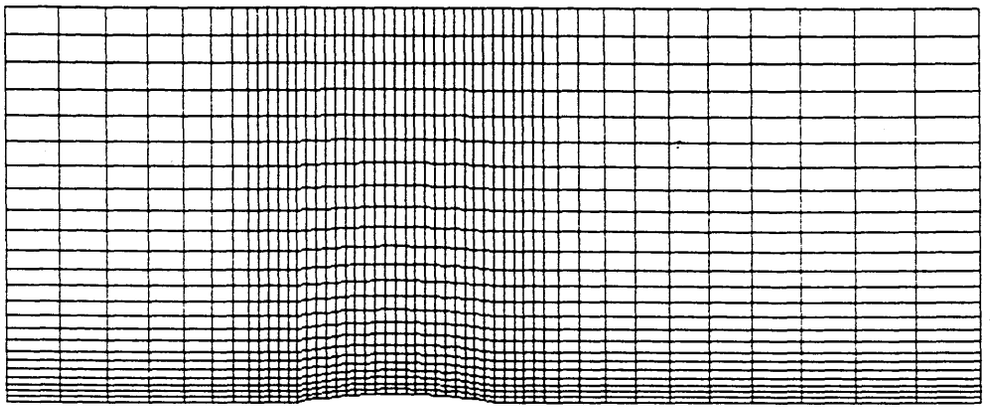

Fig. 4.12 The grid for the channel flow

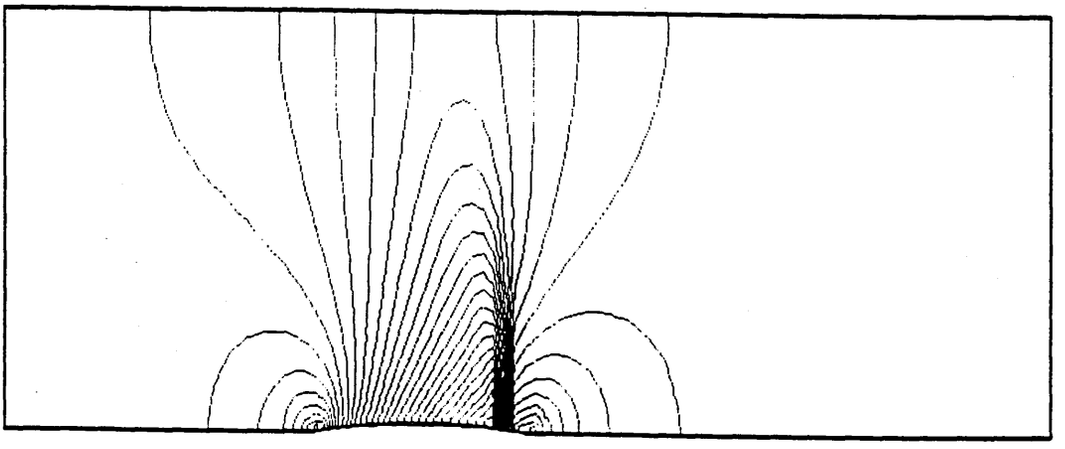

Fig. 4.13 The C_p contour of the solution using a TVD scheme

4.7 Conclusions

A new explicit scheme is suggested for multi-dimensional steady flow computations. It has some outstanding advantages over the conventional

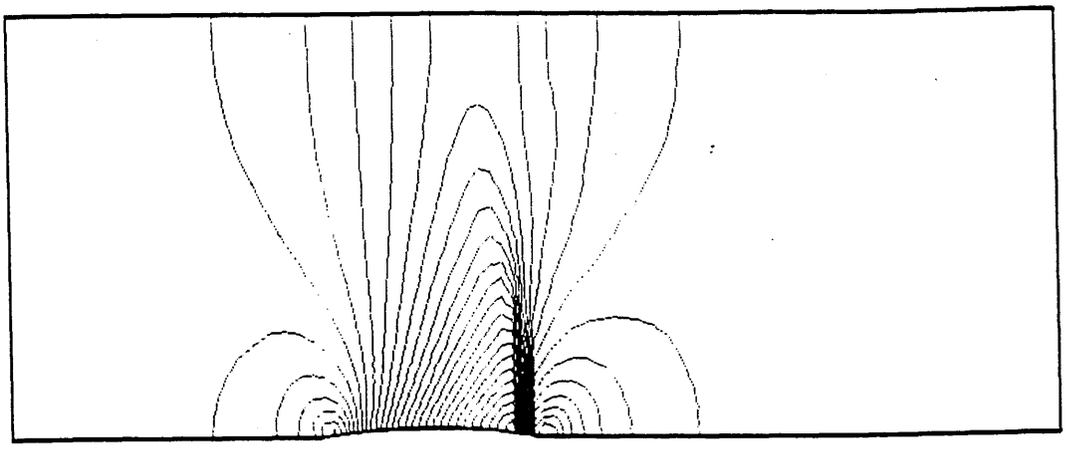

Fig. 4.14 The C_p contour of the solution using the high-order X scheme

schemes. First, the new scheme is very efficient for hyperbolic problems. It maintains a very compact form, and can be four times as fast as conventional schemes and takes only half the storage. Secondly, it possesses the right amount of dissipation to suppress the oscillations, and this dissipation is not problem dependent. Preliminary results have fully demonstrated its potential for wider applications in the solution of physical problems. Thirdly, a multigrid procedure similar to the Ni method [23] can be readily applied to the X scheme to speed up the iteration process further. Finally, its extension to three-dimensional problems is straightforward when still more savings in both CPU time and storage are expected than for the two-dimensional problems. However, further work is needed to combine a shock-fitting technique into the scheme. Furthermore, a better damping model may be possible. These are the subjects of future work.

CHAPTER 5

FLOW VISUALIZATION TECHNIQUES AND SIMULATION OF HYPERSONIC FLOW

5.1 Introduction

Finally we come to the point of simulating realistic three-dimensional hypersonic flow. The simulation is based on the assumptions made in Chapter 1, the governing equations given in Chapter 2, and the numerical approaches presented in Chapter 3. Some other aspects which are not fully covered in these chapters will be specified in the following sections.

The geometries around which flows are simulated are quite simple yet representative of future space vehicles. For example, the double ellipsoid is a representative model of the forebody of a space shuttle including a canopy. A successful simulation could provide reasonably accurate information on the aerodynamic loading and heating for designers. In that process, the simulation would be carried out in three stages, which are:

1. validation; The numerical "simulation", in principle, is not the physical process. Therefore it is subject to errors. The question that arises is to what extent these errors affect the solution. This is not an easy question to answer. Furthermore, up to now some fundamental problems have yet to be solved. For example, the existence, the uniqueness, and the convergence of the solution of a complex non-linear system

can be extremely difficult to prove. Thus numerical testing seems to be the only tool available to validate numerical algorithms in this case. Usually this is done by comparing the numerical solution of a simple problem (simple enough to have an analytical solution) to the exact solution, or by comparing the numerical solution with experiment results, etc.

2. flow visualization; This is particularly desirable for multi-dimensional flow problems, critically the three-dimensional cases. The massive amount of data is meaningless unless it is expressed in a comparative way. This is the aim of numerical flow visualization techniques. Some flow features can only be exposed by detailed flow pictures, for example vortices, shock waves, separation, etc.

3. interpretation of the results. The flow pictures developed enable understanding of the physical flow field. This is the stage of interpretation. Sometimes the pictures of different physical phenomena show similarities. In these cases, good physical insight may be required to provide the right answer. It is also possible that new flow phenomenon can be found in these pictures. The work is thus not only important but rewarding as well.

The next sections will discuss, respectively, flow visualization techniques, more aspects about the numerical procedure and detailed numerical results and discussions. Finally, some conclusions will be drawn.

5.2 Flow Visualization Techniques

5.2.1 Introduction

With recent increase in supercomputer performance and improved numerical algorithms, the generation of large three-dimensional computational fluid dynamics solutions is becoming commonplace. One of the major issues emerging from this new capability is the difficulty of displaying limited and appropriate data that will lead to a better understanding and evaluation of the flow being modelled. In three dimensions, flow phenomena such as flow separation, shocks, shear layers and vortices can often be difficult to identify and visualize. It is possible that more computer resources are expended on analyzing a solution and displaying it in a meaningful way than were needed to generate the solution in the first place [7].

Quantities describing a flow field can be either scalars or vectors. Scalar quantities such as pressure, density and Mach number, etc. are often displayed by profiles, contour lines and surfaces and variations of colour intensities. Flow directionality can be illustrated by displaying vector fields and vector traces. Selecting particles within the flow and tracing their paths is an especially effective way of observing the direction of the flow. Tracing these particle motions , then key information on separation, vortex generation and/or breakdown, etc. can be easily detected.

The following sections describe the authors's experience with the presentation of both scalar and vector fields.

5.2.2 Presentation of Scalar Fields

The typical type of display used for scalar fields is contouring. Contours are used to indicate values of the function, but they also highlight the gradient regions by their proximity to each other. Contours are always constructed in two dimensions because three-dimensional plots are very confusing and difficult to view. For three dimensional flows, contours are usually plotted in slices of solution planes.

A numerical solution only gives the values of physical variables on discrete points. Interpolation of the solution to the whole contour domain must be carried out first before the plotting of the contours. In this research, it has been found that the linear interpolation gives the most faithful representation of the original discrete solution and costs the minimum of computer resources. Because structured quadrilateral or hexahedral grids are employed in all the calculations, the interpolation can be easily implemented. For example, one quadrilateral can be divided into two triangles in the pattern shown in Fig. 5.1. The solutions (v_1, v_2, v_3) at the three vertices (x_1, y_1), (x_2, y_2), (x_3, y_3) of a triangle determine a unique interpolation

$$v = ax + by + c \tag{5.1}$$

with

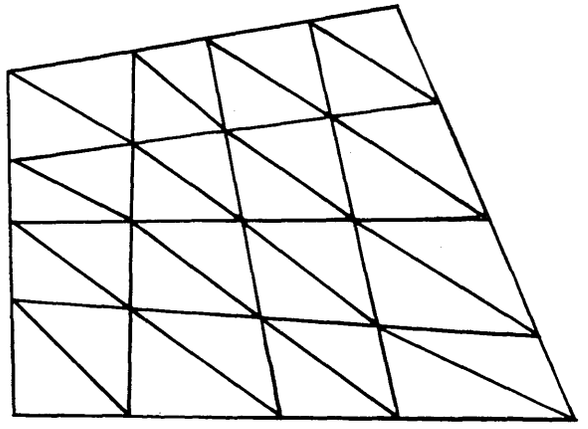

Fig. 5.1 A division pattern of the grid

$$a = \frac{\begin{vmatrix} v_1 & y_1 & 1 \\ v_2 & y_2 & 1 \\ v_3 & y_3 & 1 \end{vmatrix}}{\begin{vmatrix} x_1 & y_1 & 1 \\ x_2 & y_2 & 1 \\ x_3 & y_3 & 1 \end{vmatrix}} \qquad b = \frac{\begin{vmatrix} x_1 & v_1 & 1 \\ x_2 & v_2 & 1 \\ x_3 & v_3 & 1 \end{vmatrix}}{\begin{vmatrix} x_1 & y_1 & 1 \\ x_2 & y_2 & 1 \\ x_3 & y_3 & 1 \end{vmatrix}}$$

$$c = \frac{\begin{vmatrix} x_1 & y_1 & v_1 \\ x_2 & y_2 & v_2 \\ x_3 & y_3 & v_3 \end{vmatrix}}{\begin{vmatrix} x_1 & y_1 & 1 \\ x_2 & y_2 & 1 \\ x_3 & y_3 & 1 \end{vmatrix}}$$

Following the calculation, the contours are plotted on the area within the triangle. An alternative way is to use different colour to represent a different function value. In this approach, the boundaries of

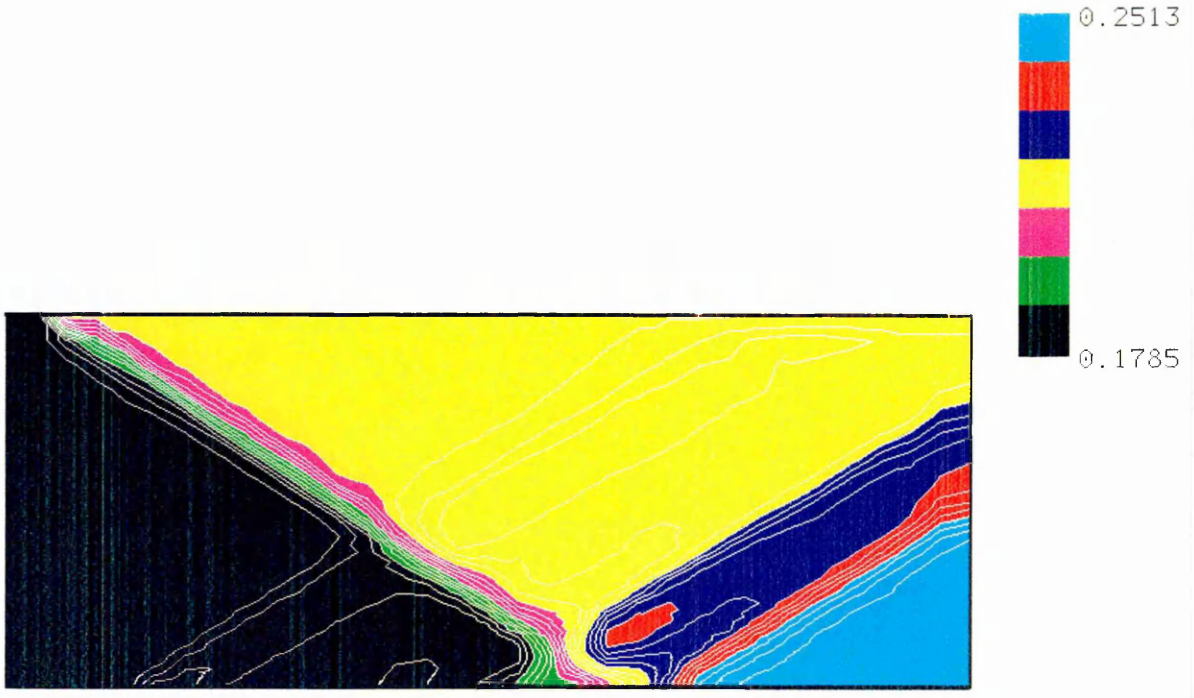

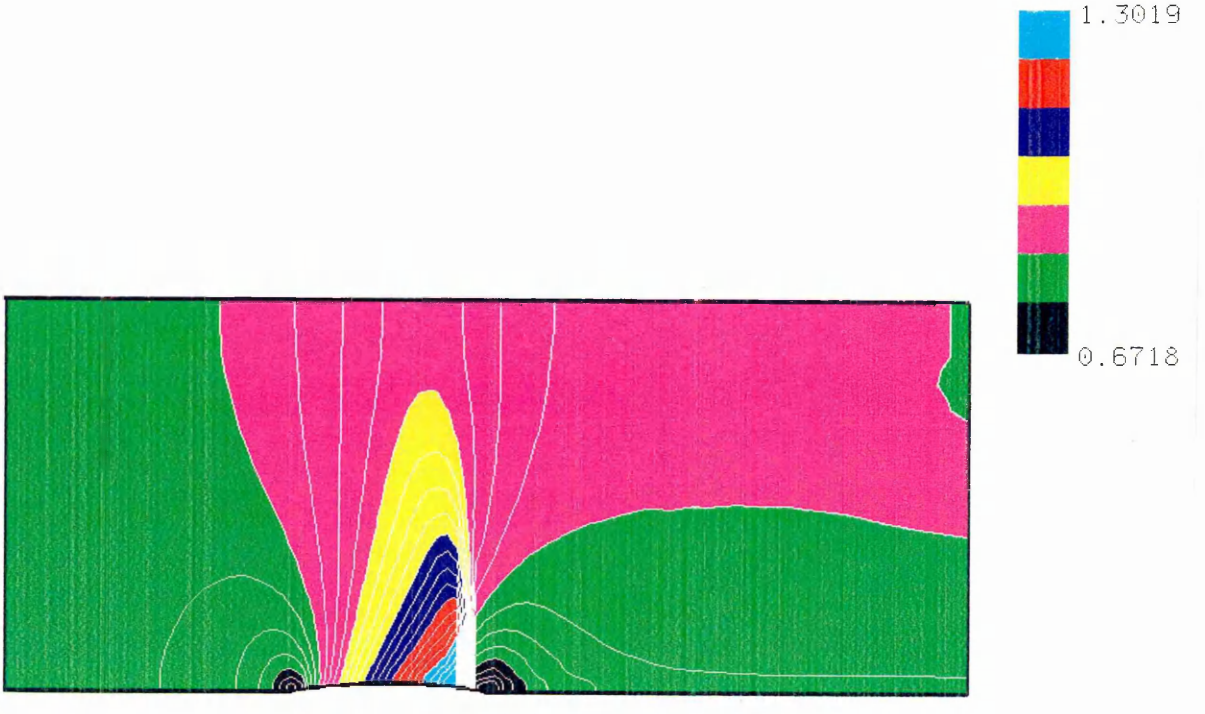

Fig. 5.2 Examples of contouring (above: a, below: b)

different-coloured areas need to be selected. This can be done in a similar fashion to contour line drawing.

Two examples are given in Fig.5.2. They demonstrate both the coloured-area filling and contour line drawing technique. Fig. 5.2a is the contour of the pressure field of the shock boundary layer interaction problem. The incident shock wave, the weak leading edge shock wave and the reflected shock wave are clearly illustrated. The expansion after the separation can be very easily detected. This contour representation thus gives a very clear picture of the interaction of the waves in the flow field. Fig. 5.2b is the Mach number contour of an inviscid transonic flow over a bump. It clearly shows that the flow accelerates on the bump from subsonic up to supersonic speed of maximum Mach number 1.301. Then a shock wave is generated through which the flow decelerates to a subsonic speed.

5.2.3 Presentation of Vector Fields

When displaying a vector field, both direction and magnitude must be presented. Velocity is a typical parameter in this category as shown in Fig. 5.3. This plot shows both the direction and magnitude of velocity for the hypersonic flow around a sphere cone. The position of the shock wave ahead of the blunt body is indicated clearly by the change of magnitude and direction of the velocity vector.

While plots of scalar variables or vector fields provide us a map of the fluid state, they often do not provide a clear picture of the structure of the flowfield, including flow separation and vortices. This is

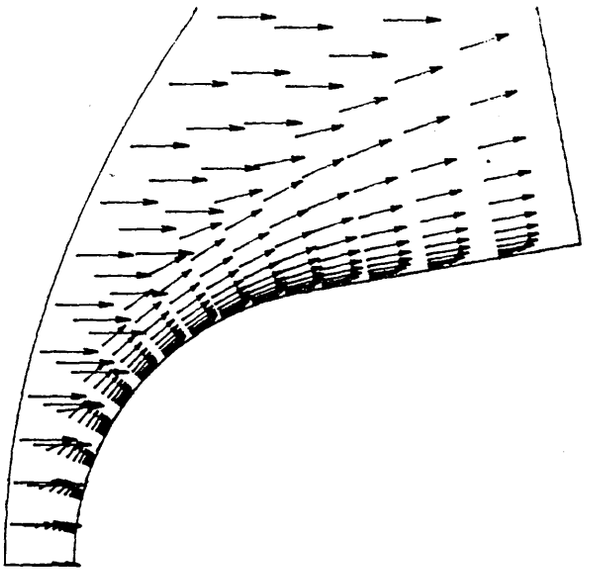

Fig. 5.3 Velocity field of the flow around a sphere cone

particularly true in three-dimensional flow simulation because only a two-dimensional projection of the vectors can be viewed at one time. In wind tunnel experiments, some key features of the flowfield can be beautifully illustrated by smoke or dye injection techniques, or oil flow patterns. In CFD, several analogous techniques can be employed to provide the equivalent "flow visualization" for computed results. These methods have proved invaluable. This is particularly true for particle tracing.

The technique of particle tracing involves following the local vector direction through the whole vector field. It indicates where the fluid is going similar to the flow visualization technique in wind tunnel experiments. If the particles are constrained to remain along the surface of a body, then the oil flow pattern is simulated. This

technique shows the direction of surface shear stress and the location of separation lines on the body. The basic idea of particle tracing is simple. However, the algorithm can be quite complex.

The algorithm in the context of a two-dimensional space is now presented. If a particle is started in the flow field at a certain point (x_0,y_0) within a triangular cell, interpolation is first used in the cell to determine the velocity vector **v** at the point by means of the formula defined in (5.1). Then the particle moves to a new position (X,Y) in speed **v** for a time step Δt

$$X = x_0 + \mathbf{v}\cdot i\Delta t \tag{5.2a}$$

$$Y = y_0 + \mathbf{v}\cdot j\Delta t \tag{5.2b}$$

The time step Δt is chosen according to both smoothness and efficiency. Smaller Δt gives a smoother trace but costs more computer time and vice versa. Searching is then started from the cell where the particle commences its motion. If the particle remains in the cell, the stage is complete. Otherwise searching continues in the first and then successive layer cells until the cell in which the particle is newly located is found. For a triangle whose vertices are (x_1,y_1), (x_2,y_2), (x_3,y_3), the necessary and sufficient conditions for a point (X,Y) to be within this triangle are

$$\left(\frac{Y-y_2}{X-x_2}-\frac{y_3-y_2}{x_3-x_2}\right)\times\left(\frac{y_1-y_2}{x_1-x_2}-\frac{y_3-y_2}{x_3-x_2}\right)\geq 0 \tag{5.3a}$$

$$\left(\frac{Y-y_1}{X-x_1}-\frac{y_2-y_1}{x_2-x_1}\right)\times\left(\frac{y_3-y_1}{x_3-x_1}-\frac{y_2-y_1}{x_2-x_1}\right)\geq 0 \tag{5.3b}$$

$$\left(\frac{Y-y_1}{X-x_1} - \frac{y_3-y_1}{x_3-x_1}\right)\times\left(\frac{y_2-y_1}{x_2-x_1} - \frac{y_3-y_1}{x_3-x_1}\right) \geq 0 \qquad (5.3c)$$

The interpolation scheme is employed again to decide the velocity of the particle once that cell is found. This process continues until the boundary or prescribed steps have been reached.

The extension of this algorithm to a three-dimensional space is straightforward. It should be pointed out that a quick searching procedure is extremely important. Otherwise the approach may be too time-consuming to be of any practical value.

Examples are given in section 5.4 to demonstrate the usefulness of these techniques.

5.3 Further Aspects about the Numerical Procedure

5.3.1 Approximate Factorization Technique

For a general three-dimensional flow problem, the governing equation employed is Eq.(2.29). The one-dimensional subset of (2.29) can be expressed as

$$\frac{\partial \bar{U}}{\partial t} + \frac{\partial \bar{E}}{\partial \xi} = \frac{\partial \bar{E}_v}{\partial \xi} \qquad (5.4)$$

A basic implicit scheme for (5.4) can be written in the form

$$\{\text{numerics}\}D = -\{\text{physics}\} \qquad (5.5)$$

where $D=\bar{U}^{n+1}-\bar{U}^{n}$, and {physics} is the numerical approximation of $\left\{\frac{\partial \bar{E}}{\partial \xi} - \frac{\partial \bar{E}_v}{\partial \xi}\right\}$. The discretisation of the {physics} part is done as follows

$$\{\text{physics}\} = \delta^{T}\bar{E} - \delta^{c}\bar{E}_{v} \tag{5.6}$$

where δ^{T} is a TVD difference operator such as the Osher-Chakravarthy, Yee or modified Yee TVD schemes, and δ^{c} is a central difference operator. If in (5.5)

$$\{\text{numerics}\} = \frac{\partial\{\text{physics}\}}{\partial \bar{U}} \tag{5.7}$$

then the scheme is called a Newtonian method. Usually the count of operations in the evaluation of {numerics} in (5.7) is so large that the method is impractical. Hence a much simpler implicit operator is chosen for efficiency. In our calculation, the following implicit operator is utilized

$$\{\text{numerics}\} = \left[\frac{I}{\Delta t} + \frac{1}{\Delta \xi}\left[\mathcal{H}_{i+1/2} - \mathcal{H}_{i-1/2}\right]\right] \tag{5.8a}$$

where

$$\mathcal{H}_{i+1/2} = \frac{1}{2}\left[\bar{A}_{i+1} - \mathcal{O}_{i+1/2}\right]^{n} \tag{5.8b}$$

The nonstandard notation

$$\mathcal{H}_{i+1/2}D = \left[\bar{A}_{i+1}D_{i+1} - \mathcal{O}_{i+1/2}D\right]^{n} \tag{5.8c}$$

is used together with

$$\mathcal{O}_{i+1/2} D = \mathrm{diag}[\psi(a^1_{i+1/2})](D_{i+1}-D_i) \tag{5.8d}$$

Scheme (5.5) with (5.8) can be written in the following form

$$\Theta_\xi D = -\Delta t\{\text{RHS of (5.6)}\} \tag{5.9}$$

where Θ_ξ is the following difference operator

$$\Theta_\xi = \left[I + \frac{\Delta t}{\Delta \xi}\left(\mathcal{H}_{i+1/2} - \mathcal{H}_{i-1/2}\right)\right] \tag{5.10}$$

This scheme is greatly simplified by ignoring the evaluation of the viscous flux Jacobian and the complex TVD flux Jacobians. According to the linear stability analysis, this scheme is stable providing Re_∞ is sufficiently high. Furthermore this procedure does not affect the final steady-state solution at all. The steady-state solution is second-order accurate and independent of the final time step used.

For the three-dimensional equation (2.29), an approximate factorization technique is adopted. The three-dimensional operator is split into three one-dimensional operators resulting in a very efficient solver. This approach is presented as follows:

$$\Theta_\xi D^{**} = \Delta t\{-\delta^T \bar{E} - \delta^T \bar{F} - \delta^T \bar{G} + \delta^c \bar{E}_v + \delta^c \bar{F}_v + \delta^c \bar{G}_v\} \tag{5.12a}$$

$$\Theta_\eta D^{*} = D^{**} \tag{5.12b}$$

$$\Theta_{\zeta} D = D^{*} \tag{5.12c}$$

where Θ_{η} and Θ_{ζ} are constructed in a similar fashion to Θ_{ξ} in (5.10)

5.3.2 Local Time Stepping

Because only steady state solution is concerned in the calculation, the time step Δt can change according to the space interval and the speed of the wave in the flow. This technique can be interpreted as an attempt to use a uniform Courant number throughout the flowfield. In any event, changing Δt can be effective for grid spacings that vary from very fine to very coarse — a situation usually encountered in aerodynamic simulations where grids contain a wide variety of length scales.

A purely geometric variation of Δt has been used in some calculations [25]. It has been found in this research, though, that a changing Δt according to both spacing and characteristic speed is more meaningful and successful. Therefore the time step is based on a prescribed CFL number for the whole flow domain, such as in the following

$$\Delta t = \frac{CFL}{\max(a_{\xi})+\max(a_{\eta})+\max(a_{\zeta})} \tag{5.13}$$

with $\Delta\xi=\Delta\eta=\Delta\zeta=1$. Here $\max(a_i)$ $(i=\xi,\eta,\zeta)$ are the maximum eigenvalues of the corresponding Jacobian matrix of the flux, and CFL is the prescribed CFL number.

5.3.3 Grid Sequencing Procedure

It is common knowledge that a solution can be easily built up in a coarse grid. There are two obvious reasons for this. First less calculations are required in a coarse grid. Second, error modes are driven out of the solution domain much more quickly in a coarse than in a fine grid. Therefore in the initial phase of a solution process, a good initial start may be obtained by solving the equations in a coarse grid, and then interpolating the solution into the fine grid. In addition to that, because a coarse grid tends to damp high frequency waves, using a grid sequencing procedure can improve the overall robustness of the code [25].

The procedure described above is implemented in the code. The finest grid is generated first. Then the coarsened grid is cut from each previous grid by halving the number of points in each coordinate direction. The flow field calculation is first started in the coarsest grid. After a finite number of iterations, the solution is then interpolated to the next finer grid and more iterations are conducted on this grid before the solution is further interpolated to an even finer grid. This process is carried out up to the finest grid. The finest grid is then iterated to convergence. It has been found that this procedure speeds up the iteration process by a factor of about 2-4.

5.3.4 Boundary Conditions

There are four kinds of boundary conditions which we are concerned with: inflow, outflow, symmetry and wall boundary conditions. These

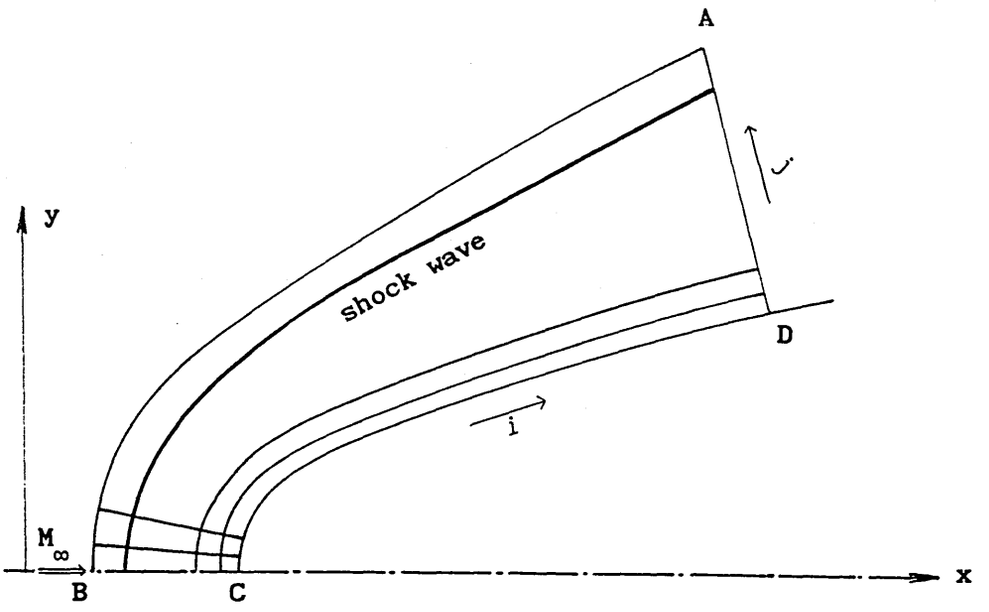

Fig. 5.4 Sketch for boundary conditions

conditions can be clearly shown by using a two-dimensional sketch in Fig.5.4.

In this figure, AB is the inflow boundary. Because the inflow is supersonic, the flow ahead of the shock wave is not disturbed by the flow in the downstream. Therefore the flow variables are fixed on the free stream values, i.e.,

$$p = \frac{1}{\gamma M_\infty^2} \qquad \rho = 1 \qquad u=1 \qquad v=0 \qquad T = 1 \tag{5.14}$$

BC is the symmetry boundary. On BC v=0, and all other variables have vanishing derivatives with respect to y, i.e.,

$$\frac{\partial f}{\partial y} = 0 \qquad (f=p,u,\rho,T \text{ etc.}) \tag{5.15}$$

Then a second order one-sided interpolation is used to get f on BC

$$f_{1,j} = (4f_{2,j} - f_{3,j})/3 \qquad (5.16)$$

Boundary CD is a solid wall. The slip and no-slip boundary conditions are used for inviscid and viscous flow calculations respectively.

For inviscid flow problems, a special principle is utilized. The principle is based on the assumption that the flow is stagnated isentropically in the normal direction of the wall. Let subscript 1 and 2 denote the solid wall and the first layer points from the wall. If the equation for the wall is

$$\eta(x,y)=0$$

then

$$\mathbf{n} = \frac{\partial \eta}{\partial x}\mathbf{i} + \frac{\partial \eta}{\partial y}\mathbf{j}$$

So the unit vector is

$$\mathbf{n}^{\circ} = \mathbf{n}/|\mathbf{n}| \qquad \text{with} \qquad |\mathbf{n}| = \left[\left(\frac{\partial \eta}{\partial x}\right)^2 + \left(\frac{\partial \eta}{\partial y}\right)^2\right]^{1/2}$$

The velocity component in direction **n** is

$$v_{n2} = \mathbf{v}_2 \cdot \mathbf{n}^{\circ} = \left(u_2 \frac{\partial \eta}{\partial x} + v_2 \frac{\partial \eta}{\partial y}\right)\frac{1}{|\mathbf{n}|}$$

The speed of sound is decided from

$$c_2 = \left(\frac{\gamma p_2}{\rho_2}\right)^{1/2}$$

So

$$M_{n2} = \frac{v_{n2}}{c_2}$$

The slip condition is actually $v_{n1} = 0$, or $M_{n1} = 0$. From the earlier stated principle, the following formulae are obtained

$$p_1 = p_2 \left[1 + \frac{\gamma-1}{2} M_{n2}^2\right]^{\gamma/(\gamma-1)}$$

$$\rho_1 = \rho_2 \left[1 + \frac{\gamma-1}{2} M_{n2}^2\right]^{1/(\gamma-1)}$$

The velocity on the wall is then obtained by extrapolation through the first and second layer points from the wall.

For viscous problems, $\frac{\partial p}{\partial n} = 0$ is employed provided Re_∞ is high. Then the temperature of the wall is specified. After that the density is calculated from the pressure and temperature. Finally u=v=0 is implied by the no-slip condition.

DA is the outflow boundary. Usually the flow through this boundary is supersonic. Thus extrapolation is used to obtain the solution on DA, i.e.,

$$f_{I,j} = 2f_{I-1,j} - f_{I-2,j} \qquad (5.17)$$

where $f=p, \rho, u, v, T$.

5.4 Numerical Simulation of Three-Dimensional Hypersonic Flow

For the purpose of universality, the 3D flow solver code is written in a general coordinate system employing the full Navier-Stokes equations. Therefore this code is expected to tackle any complex compressible laminar flow cases. A change can easily be made to solve inviscid flows by setting the slip boundary condition on the solid wall and $Re_\infty=\infty$.

5.4.1 Validation of the Method

The validation of the code in three dimensions has been carried out by solving two axisymmetric flow problems — one inviscid and one viscous. It has been firstly verified that the axisymmetric flow pattern is fully recovered. Then more detailed comparison on the accuracy of the solution is made to well documented numerical or experimental results.

The inviscid flow test case is the hypersonic flow around a sphere at Mach 8. The accurate numerical results of Lyubimov and Rusanov [20] are chosen for comparison. The computational grid includes 33 points in the mainstream direction, 33 points in the circumferential direction and 33 points in the wall-normal direction. The direction of the free stream is deliberately set to an angle with the geometric axis of symmetry in order to check the symmetric property of the flow. Fig. 5.5a shows the pressure contour and Fig 5.5b displays the Mach number contour on the plane of symmetry and the sphere surface viewed from different directions. It is clear that the solution has good symmetrical properties. The sonic line from the results of Lyubimov etc. is also

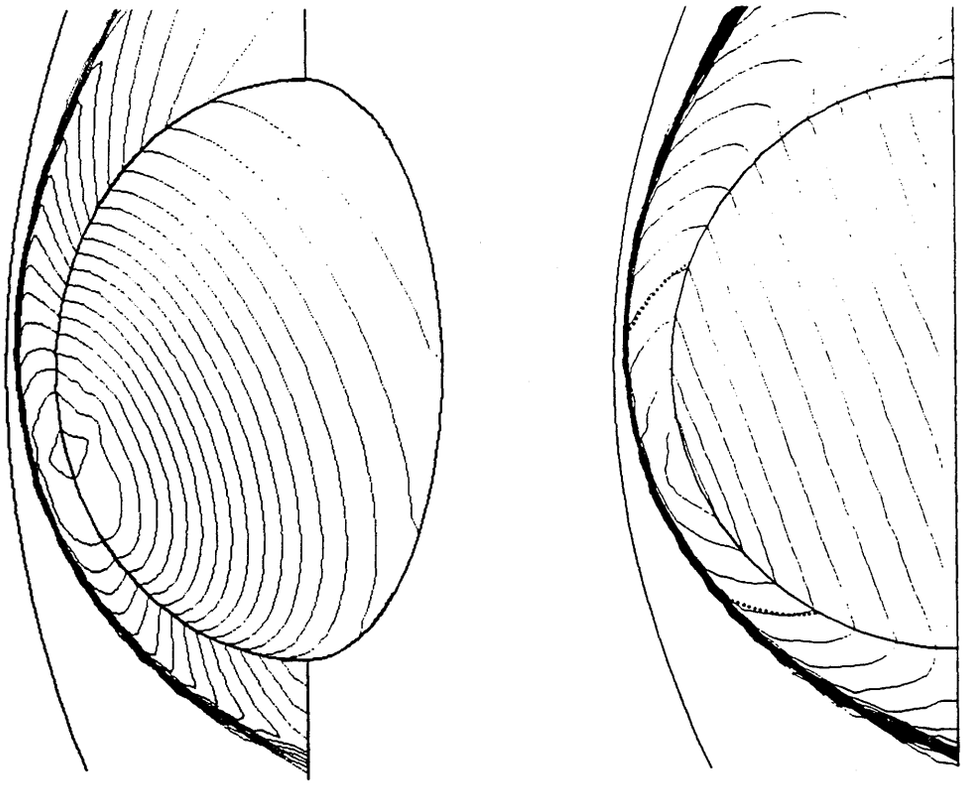

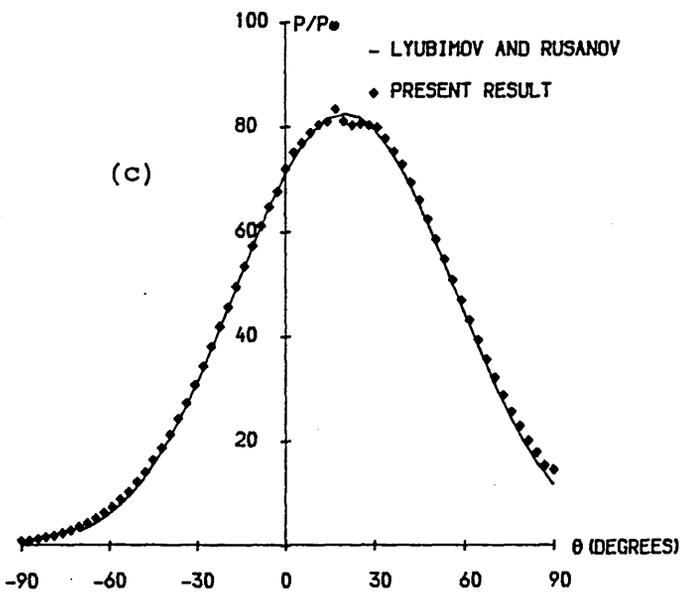

Fig. 5.5 Inviscid hypersonic flow around a sphere a) Cp contour, b) Mach contour ΔM=0.25 (· Lyubimov sonic line), c) surface pressure

plotted in Fig.5.5b. A very good agreement has been achieved. The pressure coefficient on the body surface is compared with the data from Lyubimov and Rusanov in Fig.5.5c. The agreement is indeed very good.

The second test case is the problem of the viscous hypersonic flow around a sphere cone with a cone half angle of 9.75° at $T_w/T_\infty = 4.4$, M_∞=5.92, $Re_\infty = 10^6$ and $T_\infty = 64.706$ K. The emphasis is placed on the prediction of the heat transfer rate on the wall indicated by the Stanton number which is defined by

$$St = \frac{\mu T_\infty}{(T_{0\infty} - T_w) Pr\ Re_\infty} \frac{\partial T}{\partial n} \qquad (5.18)$$

where subscript o denotes stagnation value; n is the wall normal direction. Results from Hsieh's calculation [18] are used for comparison. Fig.5.6a shows the pressure contour. It is seen that the flow symmetry is recovered very well. Fig. 5.6b is the plot of St on the wall. The present calculation is seen to have a very good agreement with the results given by Hsieh.

Confidence gained from these two test cases has resulted in the application of the flow solver code to a more realistic hypersonic flow problem.

5.4.2 Numerical Results and Discussion

As an application to realistic spacecraft body shapes, hypersonic flow around a double-ellipsoid at a high angle of attack has been

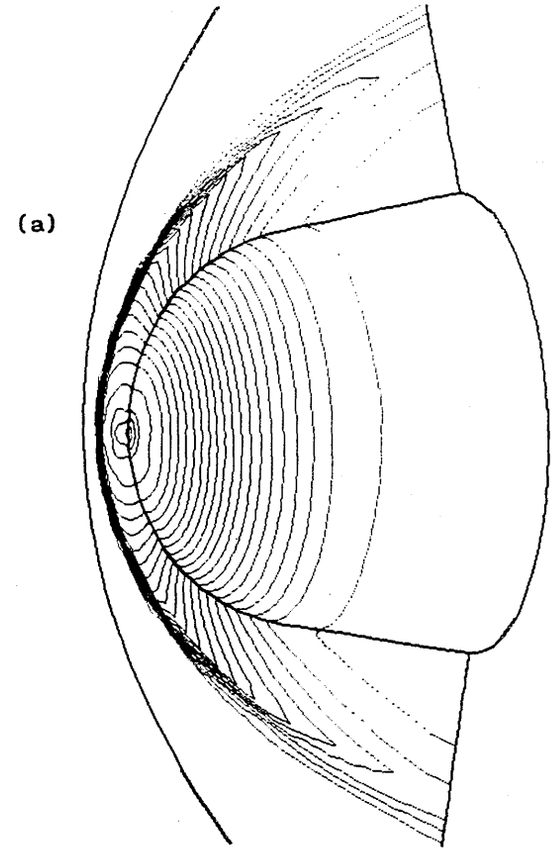

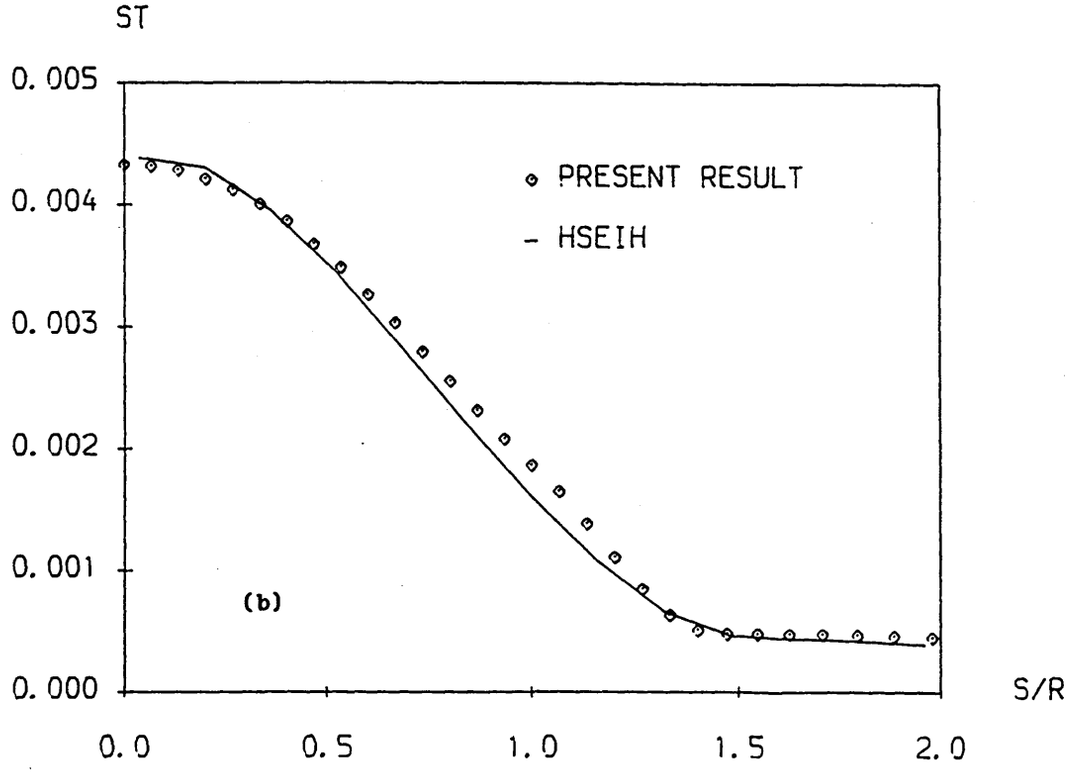

Fig. 5.6 Viscous hypersonic flow around a sphere cone

a) pressure contour, b) St number on the surface

simulated. The case is chosen from the Workshop on Hypersonic Flows for Reentry Problems co-organized by INRIA and GAMNI-SMAI, France [13]. Experimentation has been conducted to serve as a validation procedure [2]. Therefore the problem is expected to be an excellent test case for a flow solver or numerical algorithms.

The geometry of the body is a double ellipsoid extended by a truncated cylinder which is defined by

$$\left(\frac{x}{.06}\right)^2 + \left(\frac{y}{.025}\right)^2 + \left(\frac{z}{.015}\right)^2 = 1 \qquad \text{if} \quad x \le 0$$

$$\left(\frac{x}{.035}\right)^2 + \left(\frac{y}{.0175}\right)^2 + \left(\frac{z}{.025}\right)^2 = 1 \qquad \text{if} \quad x \le 0 \quad z \ge 0$$

$$\left(\frac{y}{.025}\right)^2 + \left(\frac{z}{.015}\right)^2 = 1 \qquad \text{if} \quad 0 \le x \le 0.03$$

$$\left(\frac{y}{.0175}\right)^2 + \left(\frac{z}{.025}\right)^2 = 1 \qquad \text{if} \quad z \ge 0 \qquad (5.19)$$

A body-fitted computational mesh is generated using an algebraic method. It consists of 49, 41 and 25 points in the mainstream, circumferential and wall-normal directions respectively. For accurate resolution of the physical field near the wall, the mesh is clustered in the vicinity of the body surface by means of the stretch function as defined in Eq.(3.65) in the wall-normal direction. Detailed flow conditions and solutions are now presented.

The flow conditions for this case are: free stream Mach number M_∞=8.15, angle of attack α=30°, the free stream temperature T_∞=56 K and the wall temperature T_w=288 K. Both inviscid and viscous flows have been

simulated. For the viscous flow solution, the Reynolds number is 1.67×10^{6}/m.

The meshes employed for both the inviscid and viscous flow problems are displayed in Fig. 5.7. Figs.5.8-5.10 display the Mach number, Cp and density contours on the plane of symmetry, the body surface and the plane X=0 respectively. It is obvious that the Cp contours of the inviscid and viscous flows are very similar. A very steep boundary layer appears for the viscous flow in both the Mach number and density contours. It is seen that the shock wave is well captured with at most one intermediate grid point in the windward direction. The streamlines of the inviscid flow and the oil flow pattern of the viscous flow on the body surface are presented in Fig. 5.11. The appropriate experimental oil flow pattern is also shown in the figure for comparison. The position of the calculated separation line agrees quite well with the experimental separation line. It is found, not surprisingly, that fundamental differences exist in the structure of the computed inviscid and viscous flow. No separation appears in the inviscid flow while a distinguishing separation line exists in the viscous flow. This phenomenon can be seen even more clearly in Fig.5.12, which shows the streamline on the cross section plane X=0. A large separation exists near the intersection of the two ellipsoids in the solution of viscous flow whereas no separation occurs in the inviscid flow.

Experimental data are available for the pressure coefficient and Stanton number on the wall in selected planes. Hence more detailed comparisons are now made between the calculation and the experimentation.

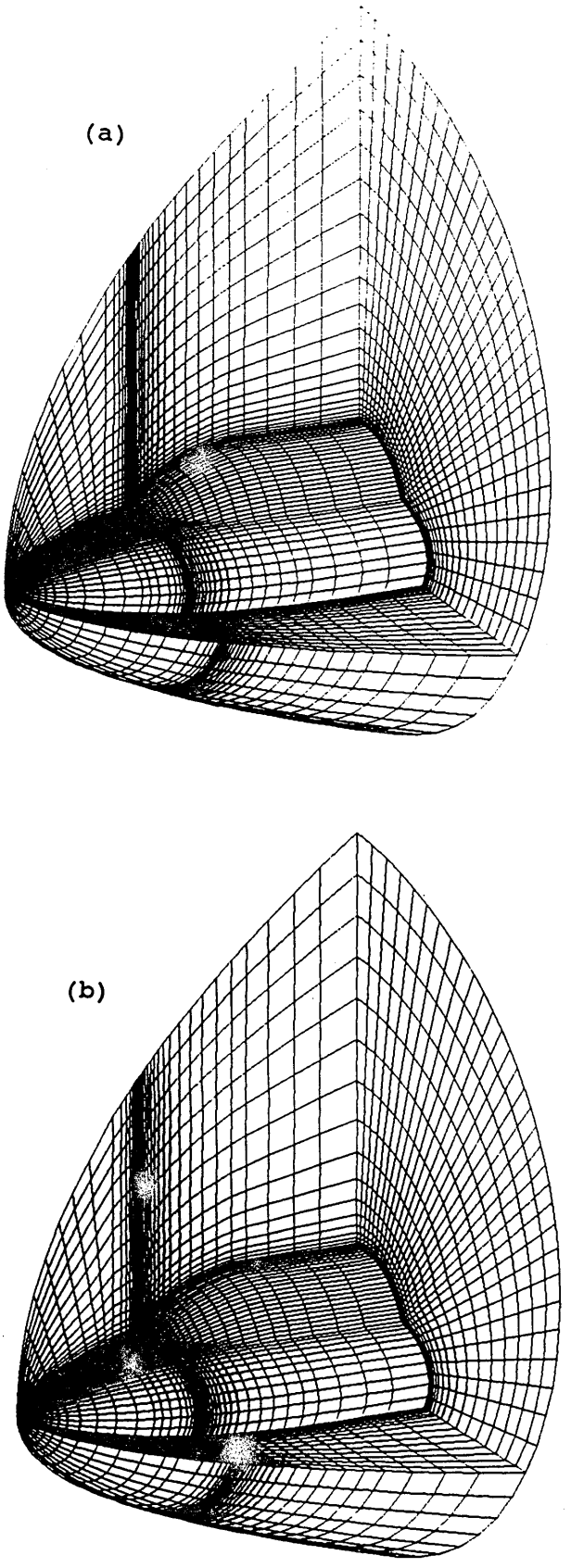

Fig. 5.7 Meshes (a. for inviscid flow, b. for viscous flow)

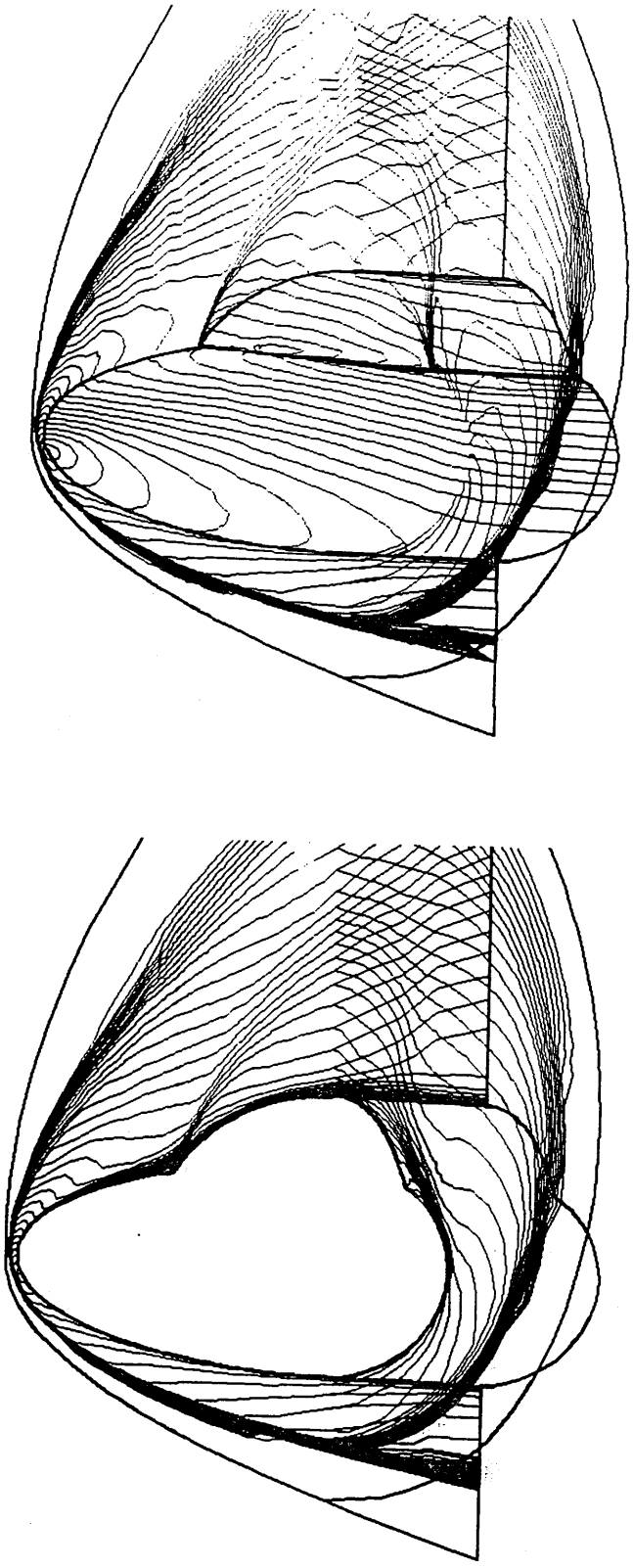

Fig. 5.8 Mach contour (above: inviscid, below: viscous)

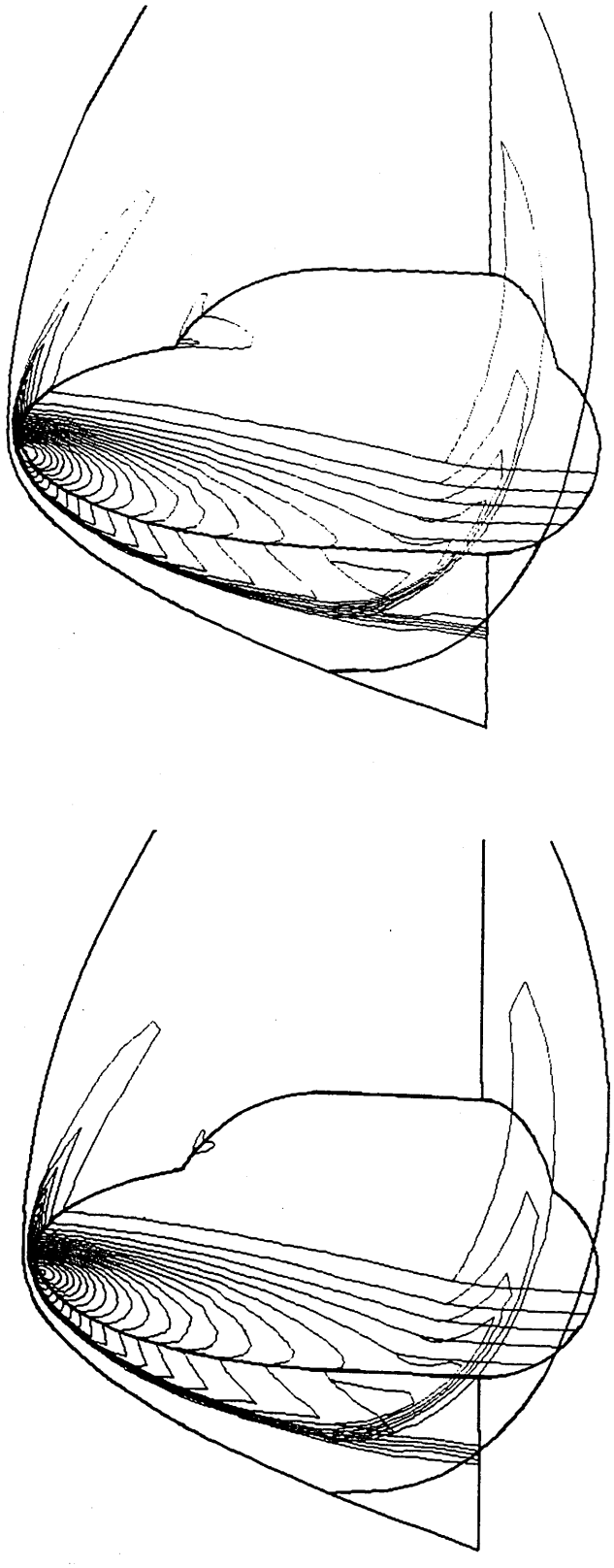

Fig. 5.9 Pressure contour (above: inviscid, below: viscous)

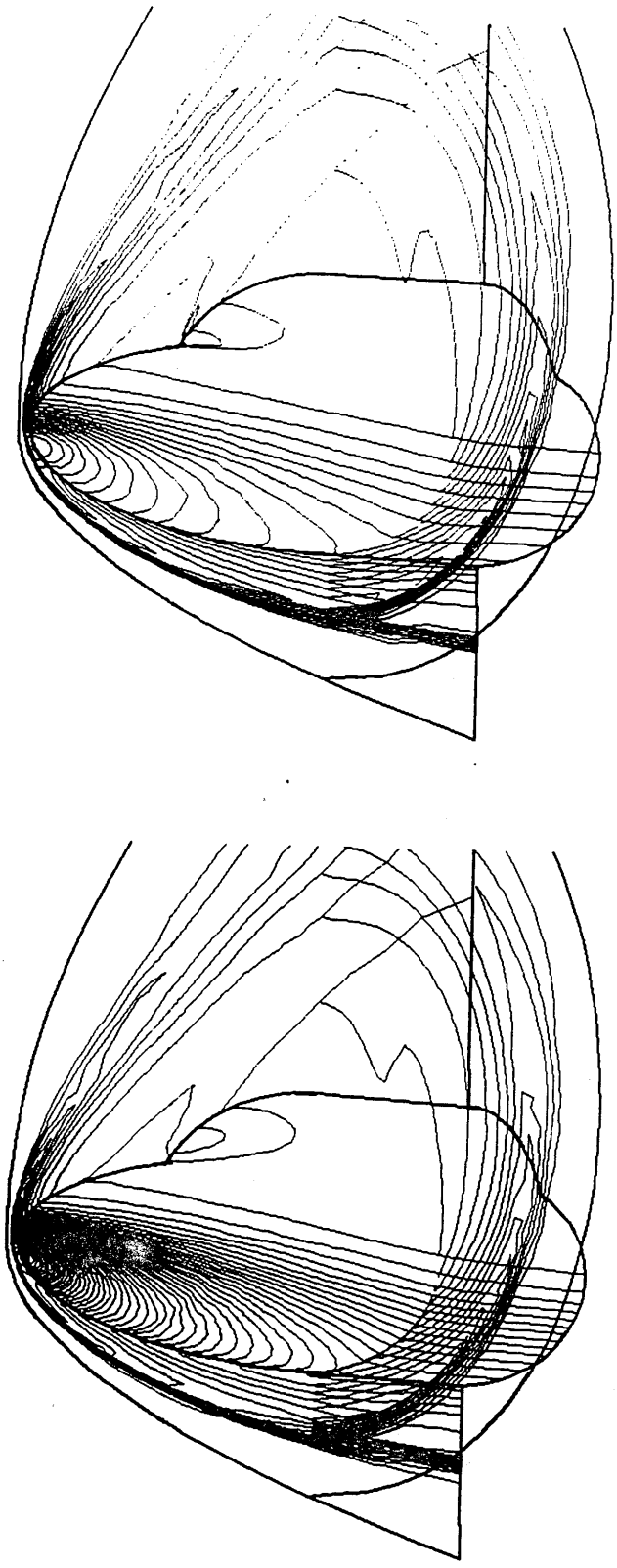

Fig. 5.10 Density contour (above: inviscid, below: viscous)

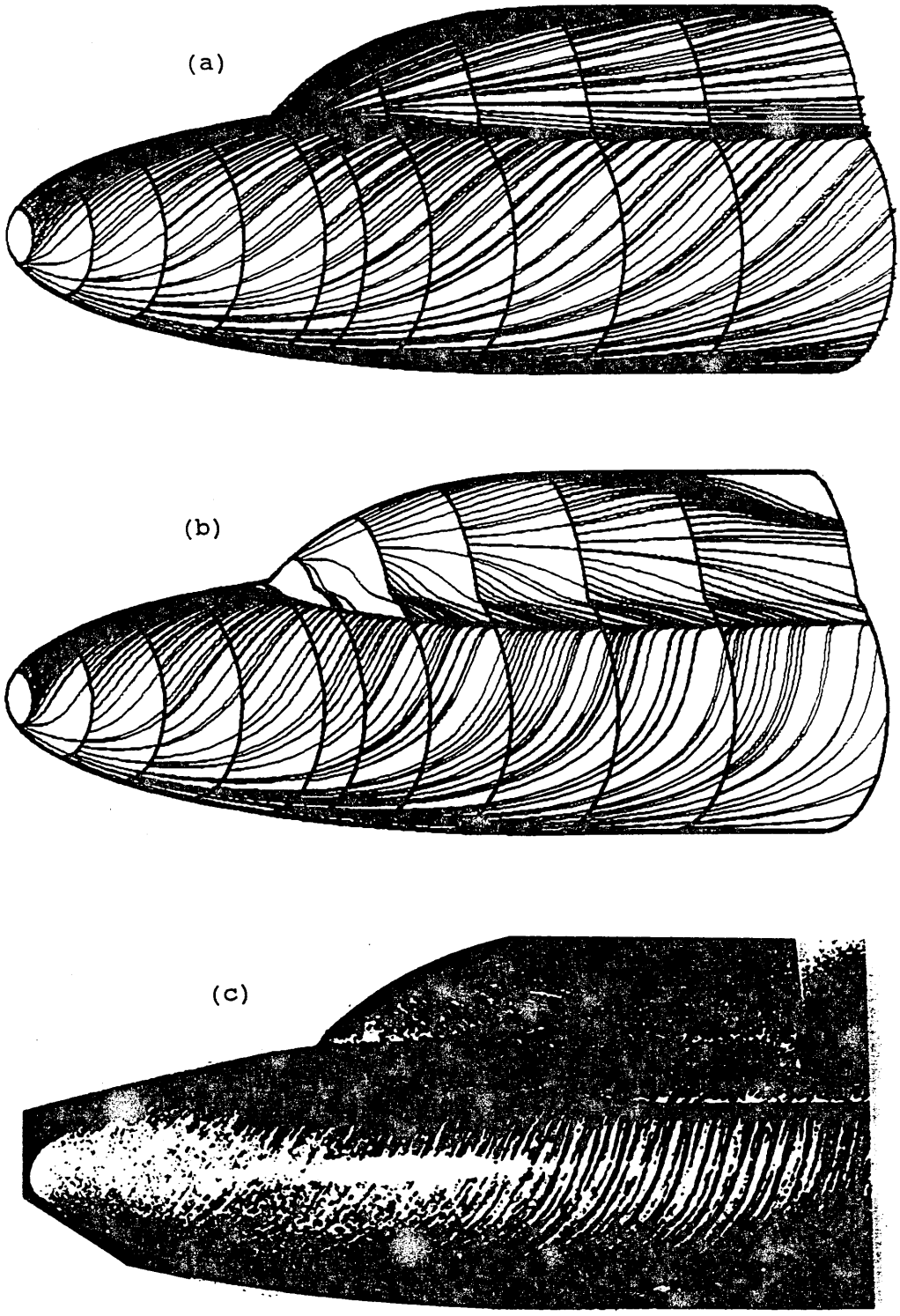

Fig. 5.11 Oil flow pattern

a) inviscid, b) viscous, c) experiment

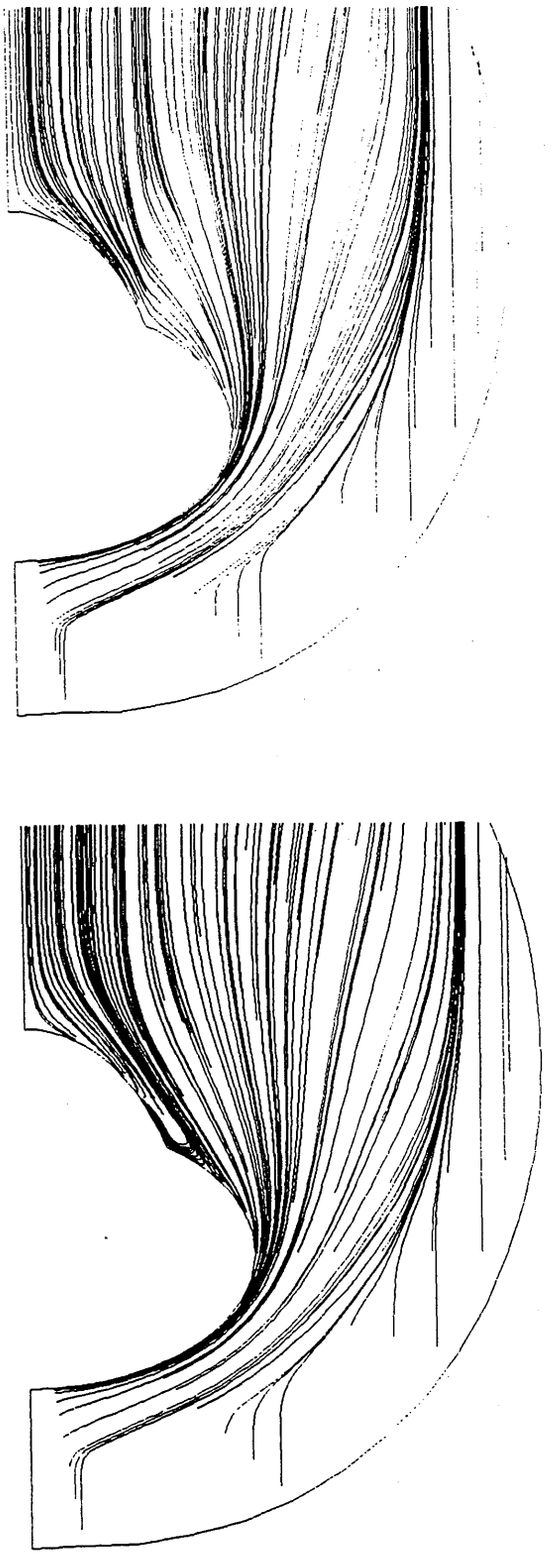

Fig. 5.12 Streamlines on plane X=0 (above: inviscid, below: viscous)

Figs. 5.13a and 5.13b show Cp on the plane of symmetry and the plane X=0. It is obvious that the inviscid solution agrees very well with the viscous solution except in the separation domain near the intersection of the two ellipsoids where viscous effects dominate the flow property. A strong shock wave appears in the inviscid flow solution while there is only a slight rise in pressure in the viscous flow solution. The numerical results for Cp are in excellent agreement with the experimental results, which is demonstrated in both Figs. 5.13a and 5.13b. Fig. 5.14 displays the calculated Stanton number on the plane of symmetry and the plane X=0. Experimental results on the windward side of the wall are also plotted. The comparison of Stanton number on the leeward side is made in Fig. 5.15. The computed and experimental results agree very well indeed. In the simulation of hypersonic flow, the heat transfer rate is usually very difficult to predict correctly especially in the viscous separated flow domain. It is found that the numerical simulation has excellent agreement with the experiment even on the leeward side. To verify that this result is not a coincidence, the temperature and velocity profiles on the plane of symmetry are plotted in Fig. 5.16. From this figure it is convincing that sufficient grid points exist in the viscous regions to expect good resolution, and that these regions are simulated very satisfactorily.

No experimental data on the skin friction coefficient is available. However, for convenience of comparison with other calculation, the Cf on the plane of symmetry is plotted in Fig. 5.17. The separation and reattachment point can be easily determined from this figure.

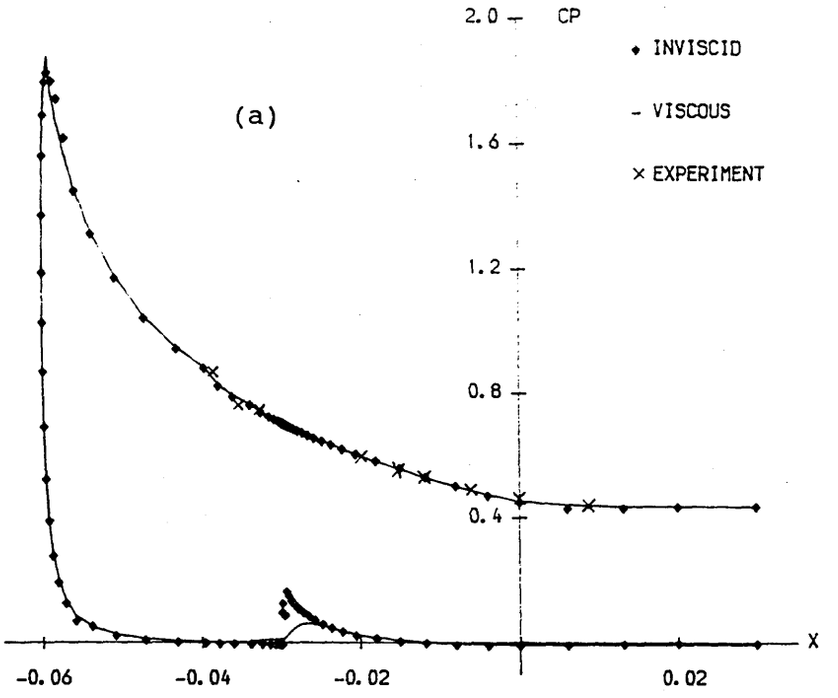

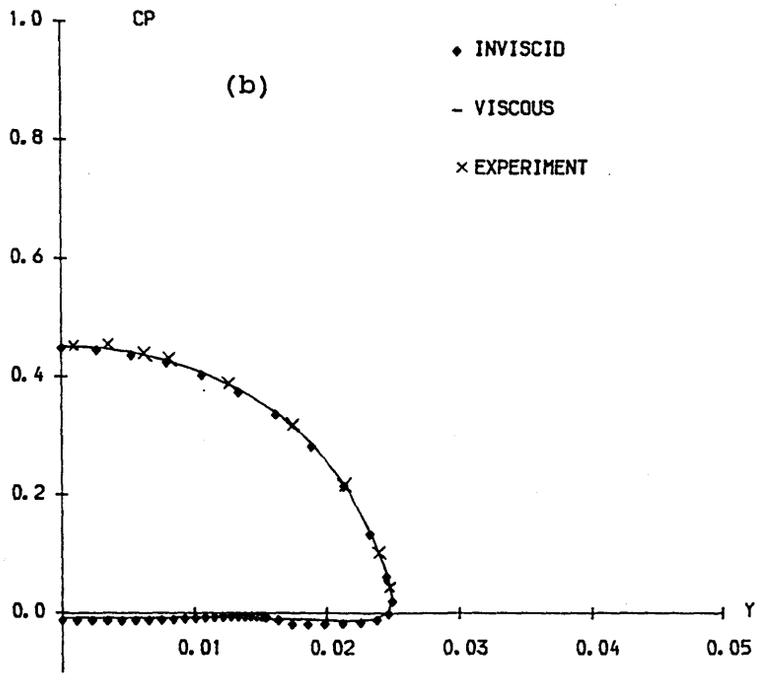

Fig. 5.13 Cp on the surface

a) Cp on the plane of symmetry, b) Cp on plane X=0

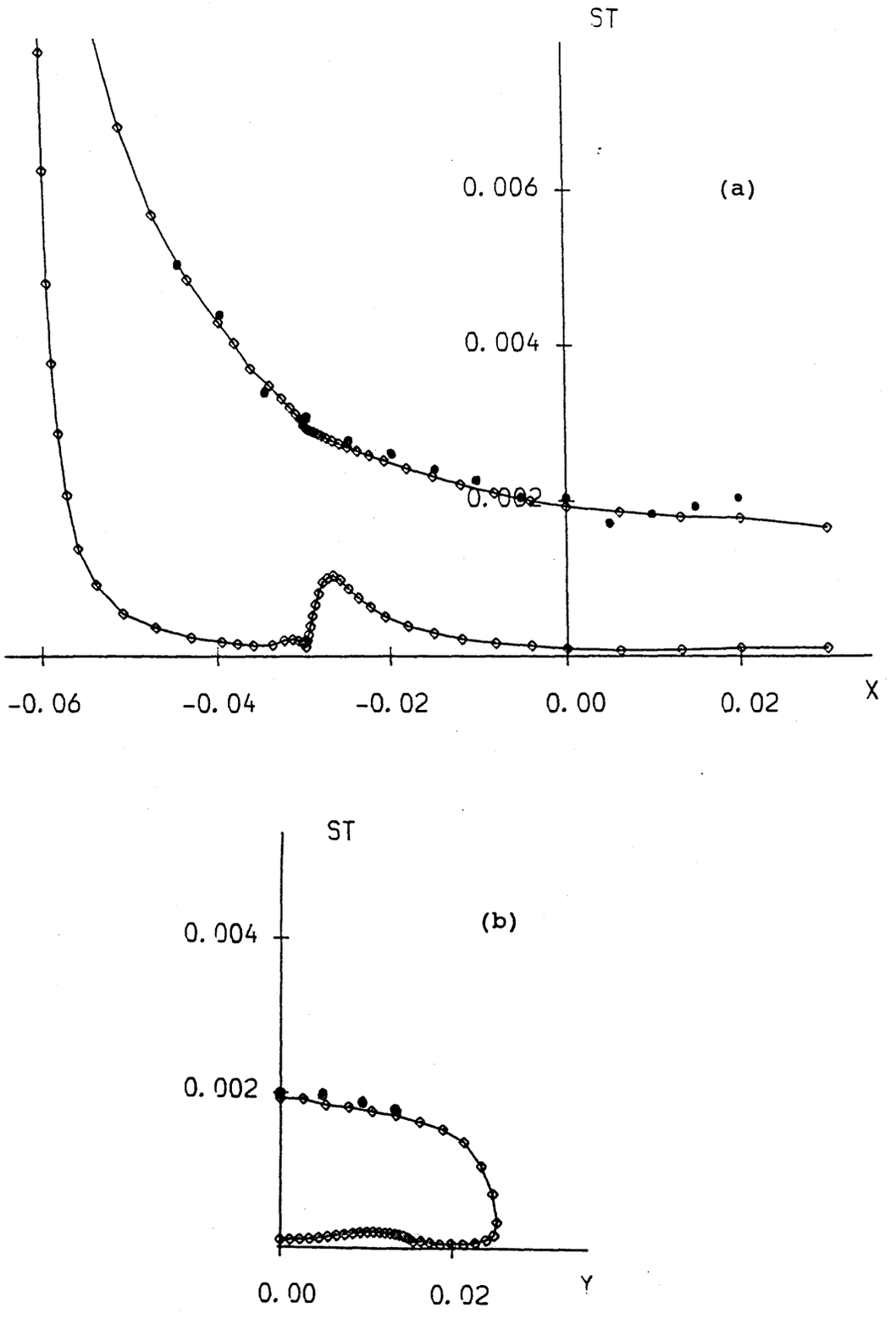

Fig. 5.14 St number on the surface (· experiment, —○— present)

a) St on the plane of symmetry, b) St on plane X=0

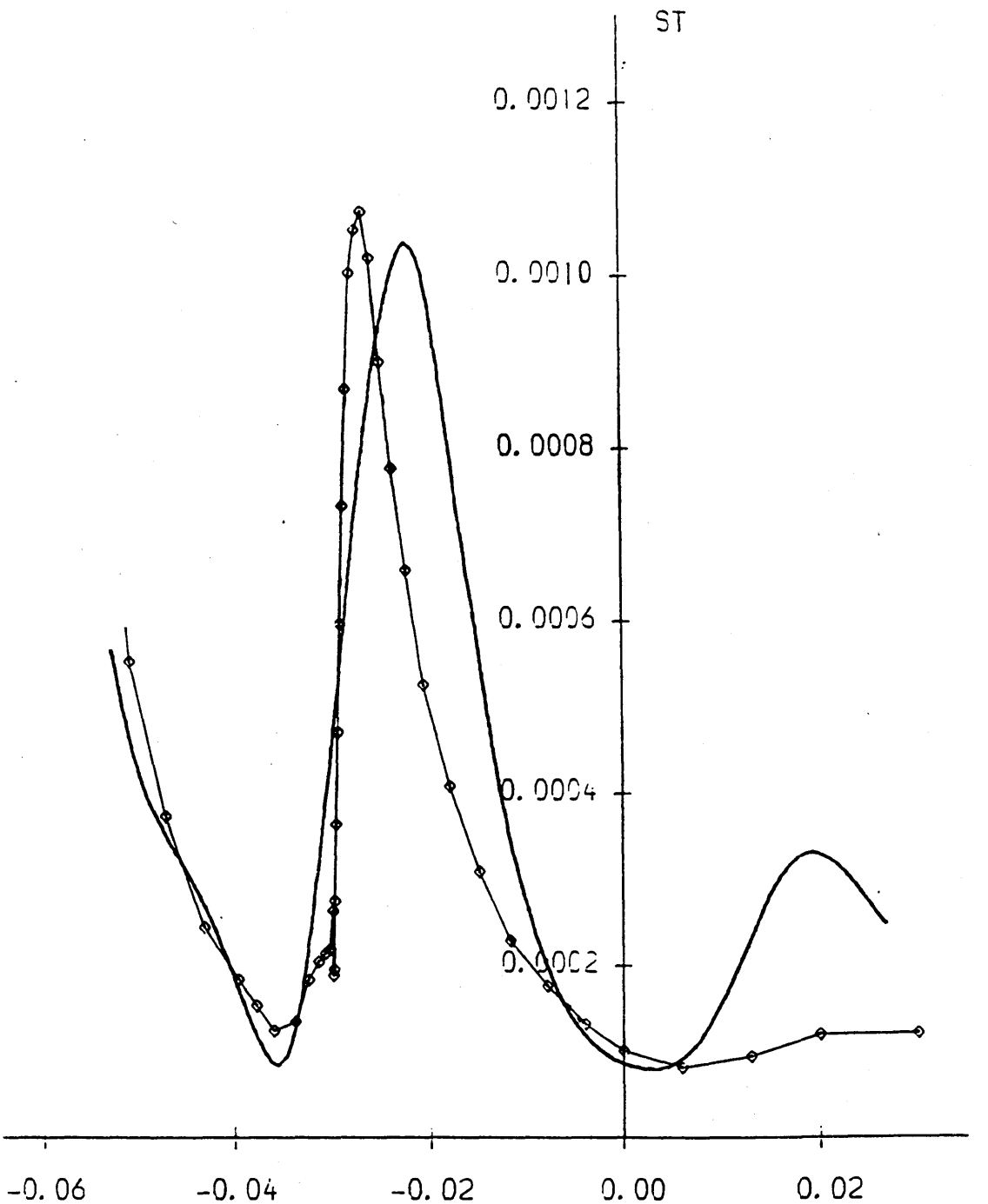

Fig. 5.15 St number on the leeward direction

(– experiment –∘– present)

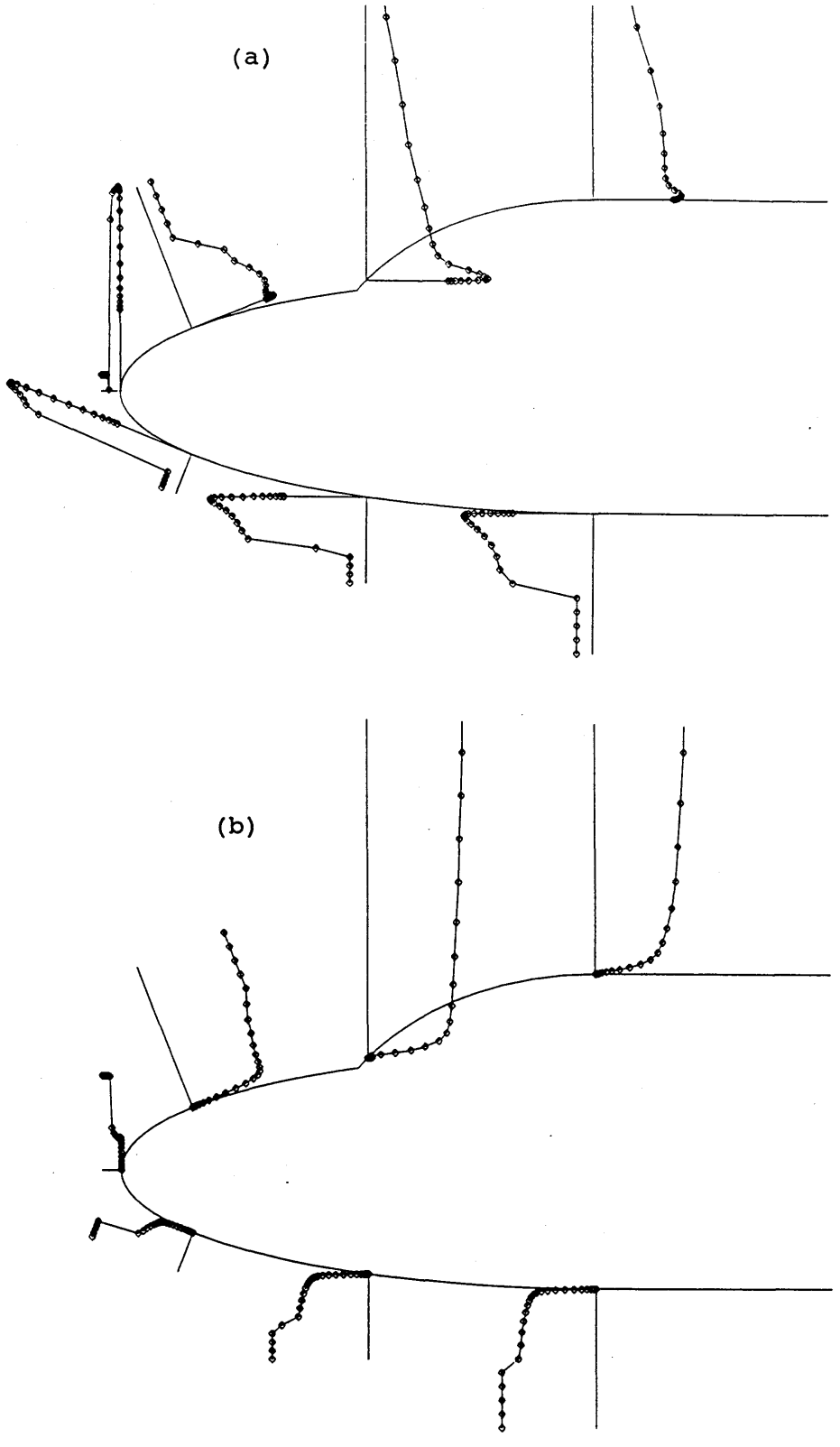

Fig. 5.16 Temperature and velocity profile on the plane of symmetry

a) temperature profile, b) velocity profile

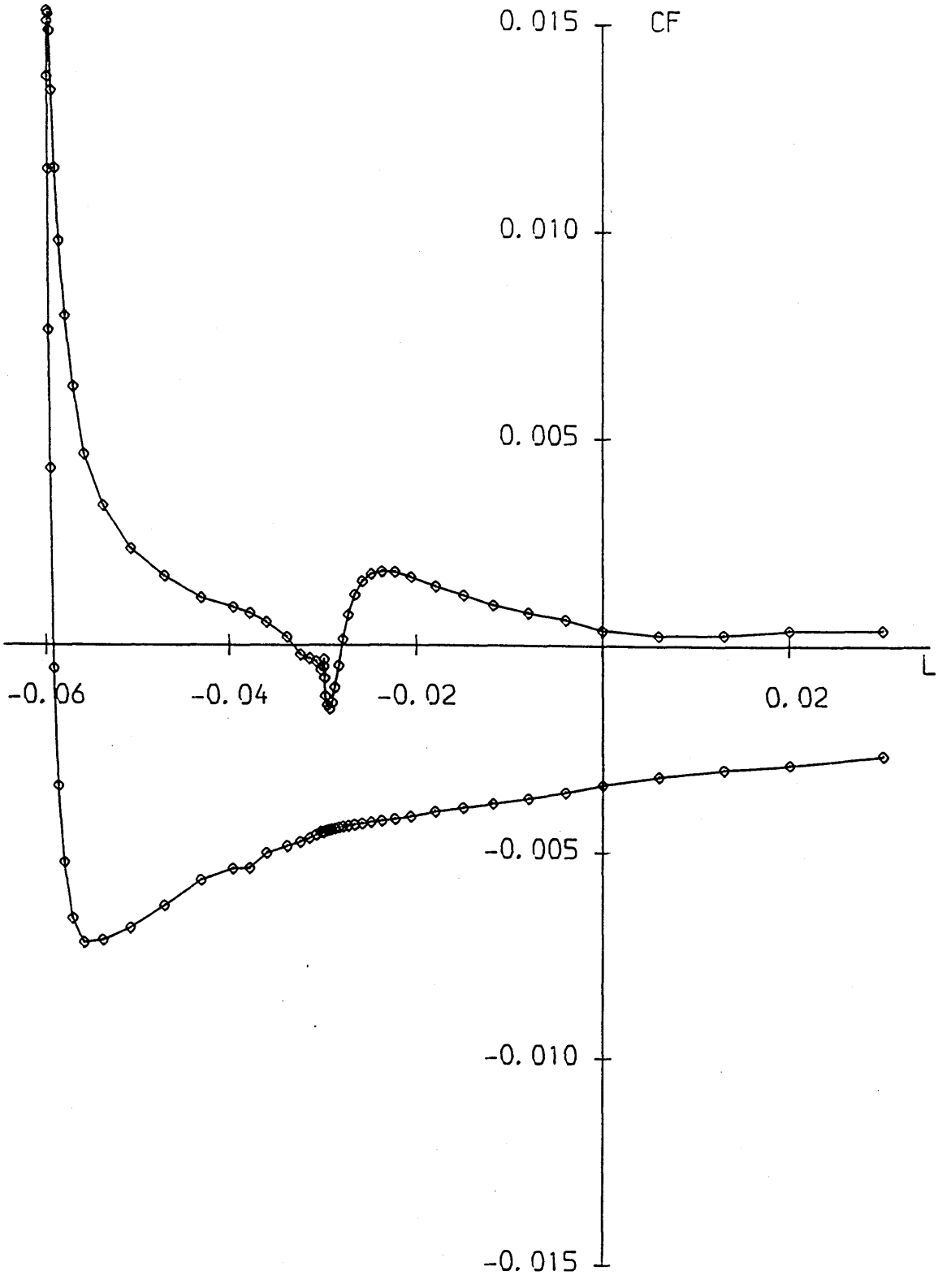

Fig. 5.17 Computed Cf on the plane of symmetry

5.5 Conclusions

In this chapter, several aspects on the simulation of three-dimensional hypersonic flow have been explored, particularly of the flow visualization techniques and the numerical procedure. Several conclusions arising from this study are drawn in the following:

1. The present numerical procedure, involving TVD schemes combined with Roe's Riemann solver, is an excellent tool in the simulation of three-dimensional hypersonic flow with very strong shock waves and severe viscous shear layers. Shock waves and shear layers are captured with high resolution. Therefore, reasonably accurate simulation of hypersonic flows can be expected even on coarse grids. This point has been fully demonstrated by the solution of the hypersonic flow around a double ellipsoid.

2. Flow visualization techniques are demanding in the solution of realistic three-dimensional flow problems. Because of the huge amount of data emanating from the solution process, the presentation of the numerical results is as important as the numerical simulation itself. The understanding of the flow structure hinges on the quality of flow pictures provided by the visualization procedure.

3. There are fundamental differences between the solutions of inviscid and viscous flow. These differences indicate that the Euler equations are not suitable for the simulation of hypersonic flow over shapes at a high angle of attack because the viscous effects emerge as large domains of separation. In that situation, the Navier-Stokes equations

appear to be the correct mathematical models for this flow field.

CHAPTER 6

CONCLUDING REMARKS AND FUTURE RESEARCH

6.1 Concluding Remarks

In this research, two main topics have been pursued. One is the development and evaluation of numerical algorithms. The other is the numerical simulation of three-dimensional hypersonic flows. More specifically, detailed investigation into the performance of the high-resolution TVD schemes with application to both inviscid and viscous flows are conducted. Confidence gained in this study resulted in their applications in the solution of three-dimensional inviscid and viscous hypersonic flows. In parallel to that, efforts to improve efficiency lead to the development of a very fast, robust explicit numerical scheme. Several conclusions resulting from the research are listed as follows:

1) TVD schemes are excellent shock-capturing approaches in both inviscid and viscous flow simulations for both one-dimensional and multi-dimensional flow problems. If they are combined with Roe's approximate Riemann solver, shock waves are usually resolved with one or, in some cases, even no intermediate grid point, thus improving the accuracy of the overall solution by a large margin. Their application to three-dimensional general coordinates does not seem to degrade the quality of the captured shock.

2) When TVD schemes are employed to solve Navier-Stokes equations at high Reynolds number, care needs be exercised to ensure that the

numerical dissipation is well below the physical dissipation. Otherwise the numerical solution may be meaningless. Two very popular TVD schemes — the Osher-Chakravarthy TVD and the Yee TVD scheme — are explored in detail. It is found, through both numerical analysis and experiments, that the former in comparison with the latter can be viewed as an *upwind-biased* second-order scheme. As a result of this feature, the former possesses much lower numerical dissipation. A modified form of the Yee TVD scheme, which is then an upwind-biased second-order scheme, is proposed to tackle viscous flows at high Reynolds number. Very favourable numerical results have been obtained.

3) When an accurate and robust numerical algorithm such as a high-resolution TVD scheme combined with Roe's approximate Riemann solver is chosen to solve practical problems, a coarse grid may be used to achieve at minimum reasonably good and at best excellent results. This has been fully demonstrated in the case of the hypersonic viscous flow around a double-ellipsoid shape at high angle of attack representing a fore body with a canopy of a re-entry space-plane. It is however also shown that there needs to be sufficient grid points (at least 10 to the author's experience) within the viscous shear or boundary layers for a successful simulation. The reasons behind this are believed to be two fold. First, TVD schemes have high-resolution properties which extend to three-dimensional viscous flows. Secondly, Roe's approximate Riemann solver takes into account all the different waves, and faithfully reflects physical interactions of waves in the fluid motion.

4) It has been found that the three-dimensional approximate factorization technique, the grid sequencing procedure, and the local

time-stepping approach are very effective ways to simplify the solution process or speed up the convergence of the solution to the steady state. At intermediate or high Reynolds number, the expensive viscous Jacobian matrices can be completely ignored from the implicit operator, resulting in a very efficient algorithm. This method does not affect the stability properties of the scheme or the final solution.

5) Numerical flow visualization techniques are extremely important for multi-dimensional flow simulations, especially for three-dimensional flow problems. Illustrations of iso-contours, velocity field plots, particle tracing and oil-flow patterns are key items for the understanding of the physical phenomena. Good flow pictures give clear indications of detailed flow behaviour and even lead to new findings in some complicated configurations. They can also play a role in locating possible errors in the simulations themselves.

6) The efficient, robust newly developed X scheme developed in this thesis has shown great promise in its preliminary investigation. Compared with the conventional first-order scheme which is called the + scheme for comparative reasons, the first-order X scheme can be four-times faster and in some cases more accurate. The high-order X scheme has almost the same high resolution as TVD schemes, and costs much less computer resources for equivalent accuracy. Because the X scheme is explicit, it can be readily vectorized. Hence even more saving in CPU time is expected. The drawback of the X scheme is its non-conservative property. Therefore some kind of shock-tracking technique should be introduced if it is used to solve hypersonic flow problems with strong shock waves.

6.2 Prospect of Future Research

The research work carried out so far is by no means complete, even in the aspect of the simulation of hypersonic flows. However, this research has certainly laid a solid foundation for more future research in both the development of numerical algorithms and simulations of realistic flows. Some areas of likely concentration for future research, I believe, can be identified. These include:

1) The improvement and application of the high-order X scheme to systems of hyperbolic conservation laws is expected to provide one of the most profitable research directions. Effort will be made to express the X scheme in conservation form. If it fails, then some kind of front tracking techniques needs to be introduced into the method to tackle problems with strong discontinuities such as shock waves, etc. The application of the X scheme to three-dimensional flow simulations is expected to have even more advantages. Obviously, its application to viscous flow problems is another interesting research topic.

2) The time-marching general 3D Navier-Stokes approach is still quite expensive. Ways to improve convergence and to reduce CPU time have to be pursued for its routine application. For example, a multi-grid approach may be utilized to speed up convergence rate; a vectorization technique may be applied to the code to reduce the CPU time to convergence. Another way to improve efficiency is expected through the use of a time-marching procedure only in subsonic flow region and a space-marching procedure in the supersonic flow domain. This necessitates the so-called parabolized Navier-Stokes method to be adopted in the code.

3) To attack flow problems at very high Reynolds number, appropriate turbulence models must be introduced into the code. This demands the development of more advanced usable yet effective turbulence models.

4) The simulation of hypersonic flows at very high Mach number requires the introduction of real gas effects and realistic chemical reaction models. Because of that, the governing equations would have stronger non-linear interactions. The resultant non-linear system would thus have increased stiffness. Therefore new numerical algorithms may be needed to solve the system of equations.

5) Mesh generation techniques for complex three-dimensional geometries is another important branch of research. Multi-zone techniques, adaptive mesh redistribution and refinement, and unstructured triangular grid generation, etc. can be deciding factors to obtain adequate resolutions of all the important features of really complex flows. They all offer opportunities for future research to be done.

Nearly three years work in CFD has been a great experience to me, unlike any other one in my life. This is particularly true since I am in a country where I have never been before and speak a totally different language from my mother tongue. In the process of this research, I have had moments of difficulty, frustration, and disappointment as well as moments of excitement, self-achievement and personal reward. I believe that is a common character of any research work. I feel it is fortunate for me to have reached the current state. If anyone finds information of value in this thesis, I would be satisfied.

APPENDIX A

The Jacobian Matrix of the Inviscid Flux

The inviscid Jacobian matrix M can be expressed in the following form (see Chapter 2):

$$M = k_1 A + k_2 B + k_3 C =$$

$$\begin{bmatrix} 0 & k_1 & k_2 & k_3 & 0 \\ k_1\iota - u\vartheta & \vartheta - k_1(\gamma-2)u & k_1 v - k_2(\gamma-1)u & k_1 w - k_3(\gamma-1)u & k_1(\gamma-1) \\ k_2\iota - v\vartheta & k_1 v - k_2(\gamma-1)u & \vartheta - k_2(\gamma-2)v & k_2 w - k_3(\gamma-1)v & k_2(\gamma-1) \\ k_3\iota - w\vartheta & k_1 w - k_3(\gamma-1)u & k_2 w - k_3(\gamma-1)v & \vartheta - k_3(\gamma-2)w & k_3(\gamma-1) \\ -\vartheta(\gamma E_t \rho^{-1} - 2\iota) & k_1(\gamma E_t \rho^{-1} - \iota) - (\gamma-1)u\vartheta & k_2(\gamma E_t \rho^{-1} - \iota) - (\gamma-1)v\vartheta & k_3(\gamma E_t \rho^{-1} - \iota) - (\gamma-1)w\vartheta & \gamma\vartheta \end{bmatrix}$$

where

$$\vartheta = k_1 u + k_2 v + k_3 w$$

$$\iota = (\gamma-1)\left[\frac{u^2 + v^2 + w^2}{2}\right]$$

M can be expressed as

$$M = R\Lambda R^{-1}$$

with

$$\Lambda = \begin{bmatrix} \vartheta & & & & & \\ & \vartheta & & & & \\ & & \vartheta & & & \\ & & & \vartheta+ka & & \\ & & & & \vartheta-ka & \end{bmatrix}$$

where

$$k = \sqrt{k_1^2 + k_2^2 + k_3^2}\ , \quad a = \left[\gamma\frac{p}{\rho}\right]^{1/2} \text{ and}$$

$$R = \begin{bmatrix} \tilde{k}_1 & \tilde{k}_2 \\ \tilde{k}_1 u & \tilde{k}_2 v - \tilde{k}_3 \rho \\ \tilde{k}_1 v + \tilde{k}_3 \rho & \tilde{k}_2 v \\ \tilde{k}_1 w - \tilde{k}_2 \rho & \tilde{k}_2 w + \tilde{k}_1 \rho \\ [\tilde{k}_1 \iota/(\gamma-1)+\rho(\tilde{k}_3 v-\tilde{k}_2 w)] & [\tilde{k}_2 \iota/(\gamma-1)+\rho(\tilde{k}_1 w-\tilde{k}_3 u)] \end{bmatrix}$$

$$\begin{bmatrix} \tilde{k}_3 & \alpha & \alpha \\ \tilde{k}_3 u + \tilde{k}_2 \rho & \alpha(u+\tilde{k}_1 a) & \alpha(u-\tilde{k}_1 a) \\ \tilde{k}_3 v - \tilde{k}_1 \rho & \alpha(v+\tilde{k}_2 a) & \alpha(v-\tilde{k}_2 a) \\ \tilde{k}_3 w & \alpha(w+\tilde{k}_3 a) & \alpha(w-\tilde{k}_3 a) \\ [\tilde{k}_3 \iota/(\gamma-1)+\rho(\tilde{k}_2 u-\tilde{k}_1 v)] & \alpha[(\iota+a^2)/(\gamma-1)+\tilde{\vartheta} a] & \alpha[(\iota+a^2)/(\gamma-1)-\tilde{\vartheta} a] \end{bmatrix}$$

where

$$\alpha = \frac{1}{2a^2}, \quad \tilde{k}_1 = \frac{k_1}{k}, \quad \tilde{k}_2 = \frac{k_2}{k}, \quad \tilde{k}_3 = \frac{k_3}{k}, \quad \tilde{\vartheta} = \frac{\vartheta}{k}$$

and

$$
R^{-1} = \begin{bmatrix}
\tilde{k}_1(1-\iota/a^2)-(\tilde{k}_3 v-\tilde{k}_2 w)/\rho & \tilde{k}_1(\gamma-1)u/a^2 \\
\tilde{k}_2(1-\iota/a^2)-(\tilde{k}_1 w-\tilde{k}_3 u)/\rho & \tilde{k}_2(\gamma-1)u/a^2-\tilde{k}_3/\rho \\
\tilde{k}_3(1-\iota/a^2)-(\tilde{k}_2 u-\tilde{k}_1 v)/\rho & \tilde{k}_3(\gamma-1)u/a^2+\tilde{k}_2/\rho \\
(\iota-\tilde{\vartheta}a) & -[(\gamma-1)u-\tilde{k}_1 a] \\
(\iota+\tilde{\vartheta}a) & -[(\gamma-1)u+\tilde{k}_1 a]
\end{bmatrix}
$$

$$
\begin{bmatrix}
\tilde{k}_1(\gamma-1)v/a^2+\tilde{k}_3/\rho & \tilde{k}_1(\gamma-1)w/a^2-\tilde{k}_2/\rho & -\tilde{k}_1(\gamma-1)/a^2 \\
\tilde{k}_2(\gamma-1)v/a^2 & \tilde{k}_2(\gamma-1)w/a^2+\tilde{k}_1/\rho & -\tilde{k}_2(\gamma-1)/a^2 \\
\tilde{k}_3(\gamma-1)v/a^2-\tilde{k}_1/\rho & \tilde{k}_3(\gamma-1)w/a^2 & -\tilde{k}_3(\gamma-1)/a^2 \\
-[(\gamma-1)v-\tilde{k}_2 a] & -[(\gamma-1)w-\tilde{k}_3 a] & (\gamma-1) \\
-[(\gamma-1)v+\tilde{k}_2 a] & -[(\gamma-1)w+\tilde{k}_3 a] & (\gamma-1)
\end{bmatrix}
$$

APPENDIX B

Grid Generation Technique by Solving the Laplace Equation

Thompson et al. [36] have worked extensively on using elliptic partial differential equations (PDE) to generate grids. Source terms are introduced to control the distribution of the grid lines. In this research, an alternative method is suggested to control the distribution of the grid points, which is in some way more straightforward.

Let Cartesian coordinates (x,y) denote the physical space and (ξ,η) denote the computational space. An intermediate space is introduced which is denoted by $(\bar{\xi},\bar{\eta})$. Assume that the physical space is related to the intermediate space $(\bar{\xi},\bar{\eta})$ by the Laplace equation

$$\begin{aligned} \bar{\xi}_{xx} + \bar{\xi}_{yy} &= 0 \\ \bar{\eta}_{xx} + \bar{\eta}_{yy} &= 0. \end{aligned} \tag{B.1}$$

The computational space (ξ,η) relates to the space $(\bar{\xi},\bar{\eta})$ by a stretch function which controls the grid point distribution in the physical domain. For example, if we require that the grid points are clustered at $\eta=\eta_0$, the following function can be used

$$\begin{aligned} \bar{\eta} &= f(\eta) = e^{D(\eta-\eta_0)} - e^{-D(\eta-\eta_0)} \\ \xi &= \bar{\xi} \end{aligned} \tag{B.2}$$

where D is a parameter which controls the degree of the clustering of

the grid points to $\eta = \eta_0$. Eqs. (B.1) and (B.2) are now transformed to the computational space by interchanging the roles of the independent and dependent variables. This yields the following equations

$$\begin{aligned} \alpha x_{\xi\xi} - 2\beta x_{\xi\eta} + \gamma x_{\eta\eta} - \gamma x_{\eta} D \tanh[D(\eta-\eta_0)] = 0 \\ \alpha y_{\xi\xi} - 2\beta y_{\xi\eta} + \gamma y_{\eta\eta} - \gamma y_{\eta} D \tanh[D(\eta-\eta_0)] = 0 \end{aligned} \tag{B.3}$$

where

$$\begin{aligned} \alpha &= x_{\eta}^2 + y_{\eta}^2 \\ \beta &= x_{\xi}x_{\eta} + y_{\xi}y_{\eta} \\ \gamma &= x_{\xi}^2 + y_{\xi}^2 \end{aligned}$$

Eq. B.3 can be solved using available finite difference method subject to appropriate boundary conditions. In practice, orthogonal mesh is preferred especially on the boundary. We thus consider a boundary determined by the following equation

$$\Gamma(x,y) = 0 \tag{B.4}$$

On the computational space, this boundary is represented by a coordinate line

$$\eta(x,y) = 0$$

If coordinate line ξ is vertical to η on the boundary, the following equation must be satisfied

$$(\eta_x \mathbf{i} + \eta_y \mathbf{j}) \cdot (\xi_x \mathbf{i} + \xi_y \mathbf{j}) = 0$$

or

$$\xi_x \eta_x + \xi_y \eta_y = 0 \tag{B.5}$$

But

$$(\Gamma_x, \Gamma_y) \propto (\eta_x, \eta_y) \quad \text{and} \quad \xi_x = \frac{y_\eta}{J}, \quad \xi_y = \frac{-x_\eta}{J}$$

where J is the Jacobian matrix of the transformation. Hence

$$\Gamma_x y_\eta - \Gamma_y x_\eta = 0 \tag{B.6}$$

Eqs. (B.4) and (B.6) can be used to decide the distribution of grid points on the boundary.

APPENDIX C

Stability Analysis

In the research included in this thesis, the viscous flux Jacobian matrices are dropped from the implicit operator. It will be shown here that at high Reynolds number, this procedure would not affect the stability condition of the original scheme by the study of the one-dimensional linear Burgers' equation.

First the linear wave equation in one dimension is considered, i.e.,

$$\frac{\partial u}{\partial t} + a\frac{\partial u}{\partial x} = 0. \qquad (a>0) \tag{C.1}$$

The following implicit scheme is employed to tackle (C.1)

$$\frac{u_j^{n+1}-u_j^n}{\Delta t} + a\frac{u_{j+1}^{n+1}-u_{j-1}^{n+1}}{2\Delta x} = 0 \tag{C.2}$$

Eq. (C.2) can be written in Δ form as

$$(D_j + \frac{\nu}{2}D_{j+1} - \frac{\nu}{2}D_{j-1}) = -\frac{\nu}{2}(u_{j+1}^n - u_{j-1}^n) \tag{C.3}$$

where $D_j = u_j^{n+1} - u_j^n$ and $\nu = \frac{a\Delta t}{\Delta x}$.

Scheme (C.3) is unconditionally stable and is second-order accurate in space.

Consider the first-order upwind scheme

$$\frac{u_j^{n+1}-u_j^n}{\Delta t} + a\frac{u_j^{n+1}-u_{j-1}^{n+1}}{\Delta x} = 0$$

or

$$(1+\nu)D_j - \nu D_{j-1} = -\nu(u_j^n - u_{j-1}^n) \qquad (C.4)$$

This scheme is also unconditionally stable. However the steady-state solution of (C.4) is only first-order accurate in space. If we use the following hybrid scheme

$$(1+\nu)D_j - \nu D_{j-1} = -\frac{\nu}{2}(u_{j+1}^n - u_{j-1}^n) \qquad (C.5)$$

then the steady-state solution would be second-order accurate in space. The amplification factor of (C.5) is found to be

$$G = \frac{(1+\nu) - \nu\cos\beta}{(1+\nu) - \nu\cos\beta + i\nu\sin\beta} \qquad (C.6)$$

It is obvious that $|G| \leq 1$. So scheme (C.5) is also unconditionally stable.

Now if we solve

$$\frac{\partial u}{\partial t} + a\frac{\partial u}{\partial x} = \frac{1}{Re}\frac{\partial^2 u}{\partial x^2} \qquad (C.7)$$

then the following scheme is used

$$(1+\nu)D_j - \nu D_{j-1} = -\frac{\nu}{2}(u^n_{j+1} - u^n_{j-1}) + \frac{\Delta t}{Re\Delta x^2}(u^n_{j+1} - 2u^n_j + u^n_{j-1}) \qquad (C.8)$$

The amplification factor of (C.8) is

$$G = \frac{(1+\nu) - \nu\cos\beta - 2\Delta t(1-\cos\beta)/(Re\Delta x^2)}{(1+\nu) - \nu\cos\beta + i\nu\sin\beta} \qquad (C.9)$$

Eq. (C.9) can be written as

$$G = \frac{1+\nu(1-\cos\beta)[1-2/(aRe\Delta x)]}{(1+\nu) - \nu\cos\beta + i\nu\sin\beta} \qquad (C.10)$$

Because $\nu > 0$, so if

$$\left|1+\nu(1-\cos\beta)\left[1-\frac{2}{aRe\Delta x}\right]\right| \le 1+\nu(1-\cos\beta) \quad \text{or}$$

$$-1-\nu(1-\cos\beta) \le 1+\nu(1-\cos\beta)\left[1-\frac{2}{aRe\Delta x}\right] \le 1+\nu(1-\cos\beta) \qquad (C.11)$$

scheme (C.8) is stable. If the following inequalities

$$1 - \frac{2}{aRe\Delta x} \le 1 \quad \text{and} \quad \frac{2}{aRe\Delta x} \le 1 + \frac{1}{\nu(1-\cos\beta)} \qquad (C.12)$$

are satisfied, (C.11) is true. If

$$\frac{1}{aRe\Delta x} \le 1 + \frac{1}{2\nu} \qquad (C.13)$$

is correct, then (C.12) is true. That means

$$\Delta t(1-aRe\Delta x) \le \frac{Re\Delta x^2}{2} \qquad (C.14)$$

If $Re \geq \frac{1}{a\Delta x}$, (C.14) is always true.

If $Re < \frac{1}{a\Delta x}$, for (C.14) to be satisfied, we should have

$$\Delta t \leq \frac{Re\Delta x^2/2}{1-aRe\Delta x}$$

Thus it has been proved that whenever $Re \geq \frac{1}{a\Delta x}$, scheme (C.8) is unconditionally stable.

REFERENCES AND BIBLIOGRAPHY

References

1. W.K. Anderson, J.L. Thomas and B. van Leer, "A Comparison of Finite Volume Flux Vector Splittings for the Euler Equations," AIAA Paper No.85-0122.

2. D. Aymer, T. Alziary, G Carlomagno and L. De Luca, "Experimental Study of Flow over a Double Ellipsoid," in Proceedings, Workshop on Hypersonic Flows for Reentry Problems, Antibes (France), January 1990.

3. R.M. Beam and R.F. Warming, "An Implicit Factored Scheme for the Compressible Navier-Stokes Equations," *AIAA J.* **16**, 393 (1978).

4. D.L. Book, J.P. Boris and K. Hain, "Flux-Corrected Transport II: Generalizations of the Method," *J. Comput. Phys.* **18**, 248 (1975).

5. J.P. Boris and D.L. Book, "Flux-Corrected Transport I: SHASTA, A Fluid Transport Algorithm That Works," *J. Comput. Phys.* **11**, 38 (1973).

6. J.P. Boris, "New Directions in Computational Fluid Dynamics," *Ann. Rev. Fluid Mech.* **21**, 345 (1989).

7. P.G. Buning and J.L. Steger, "Graphics and Flow Visualization in Computational Fluid Dynamics," AIAA Paper No.85-1507.

8. S.R. Chakravarthy and S. Osher, "A New Class of High Accuracy TVD Schemes for Hyperbolic Conservation Laws," AIAA Paper No. 85-0363.

9. S.R. Chakravarthy, "Euler Equations—Implicit Schemes and Boundary Conditions," *AIAA J.* **21**, 699 (1983).

10. S.R. Chakravarthy, "High Resolution Upwind Formulations for Hyperbolic Conservation Laws," Lecture Notes for Computational Fluid

Dynamics, von-Karman Institute for Fluid Dynamics, March 1988.

11. S.H Chang and M-S Liou, "A Comparison of ENO and TVD Schemes," AIAA Paper No.88-3707-CP.

12. S.F. Davis, "TVD Finite Difference Schemes and Artificial Viscosity," ICASE Report No.84-20, June 1984 (unpublished).

13. J-A Desideri and J. Périaux, Workshop on Hypersonic Flows for Reentry Problems, INRIA and GAMNI-SMAI, France, 1990.

14. S.K. Godunov, "Finite Difference Method for Numerical Computation of Discontinuous Solutions of the Equation of Fluid Dynamics," *Mat. Sbornik.* **47**, 271 (1959).

15. J.B. Goodman and R.J. LeVeque, "On the Accuracy of Stable Schemes for 2D Scalar Conservation Laws," *Math. Comput.* **45**, 15 (1985).

16. A. Harten, "High Resolution Schemes for Hyperbolic Conservation Laws," *J. Comput. Phys.* **49**, 357 (1983).

17. A. Harten, B. Engquist, S. Osher and S. Chakravarthy, "Uniformly High Order Accurate Essentially Non-Oscillatory Schemes III," *J. Comput. Phys.* **71**, 231 (1987).

18. T. Hsieh, "Calculation of Viscous Hypersonic Flow over a Severely Indented Nosetip," *AIAA J.* **22**, 935 (1984).

19. A. Jameson, "Successes and Challenges in Computational Aerodynamics," AIAA Paper No.87-1184.

20. A.N. Lyubimov and V.V. Rusanov, "Gas Flows Past Blunt Bodies," NASA-TT-F715, February 1973.

21. R.W. MacCormack, "A Numerical Method for Solving the Equation of Compressible Viscous Flow," *AIAA J.* **20**, 1275 (1982).

22. K.W. Morton and M.F. Paisley, "A Finite Volume Scheme with Shock Fitting for the Steady Euler Equations," *J. Comput. Phys.* **80**, 168 (1989).

23. R.H. Ni, "A Multiple Grid Scheme for Solving the Euler Equations," *AIAA J.* **20**, 1565 (1982).

24. S. Osher, "Riemann Solvers, the Entropy Condition and Difference Approximation," *SIAM J. Numer. Anal.* **21**, 217 (1984).

25. T.H. Pulliam, and J.L. Steger, "Recent Improvements in Efficiency, Accuracy, and Convergence for Implicit Approximate Factorization Algorithms," AIAA Paper No. 85-0360.

26. S. Riedelbauch, W. Wetzel, W. Kordulla and H. Oertel, "On the Numerical Simulation of Three-dimensional Hypersonic Flow," Aerodynamics of Hypersonic Lifting Vehicles, AGARD-CP-428, Paper 19, 1987.

27. Y. Rizk, D. Chaussee and J. Steger, "Numerical Simulation of the Hypersonic Flow around Lifting Vehicles," Aerodynamics of Hypersonic Lifting Vehicles, AGARD-CP-428, Paper 16, 1987.

28. P.L. Roe, "Approximate Riemann Solvers, Parameter Vectors, and Difference Schemes," *J. Comput. Phys.* **43**, 357 (1983).

29. P.L. Roe, "Generalized Formulation of TVD Lax-Wendroff Schemes," ICASE Report No.84-53, October 1984 (unpublished).

30. P.L. Roe, "Some Contributions to the Modelling of Discontinuous Flows," Lectures in Applied Mathematics, Vol. 22 (Amer. Math. Soc., Providence, R.I., 1985).

31. S. Spekreijse, "Multigrid Solution of Monotone Second-Order Discretization of Hypersonic Conservation Laws," *Math. Comput.* **49**, 135 (1987).

32. J.L. Steger and R.F. Warming, "Flux Vector Splitting of the Inviscid

Gasdynamics Equations with Application to Finite Difference Methods," *J. Comput. Phys.* **40**, 263 (1981).

33. P.K. Sweby, "High Resolution Schemes Using Flux Limiters for Hyperbolic Conservation Laws," *SIAM J. Numer. Anal.* **21**, 995 (1984).

34. Y. Takakura, T. Ishiguro, and S. Ogawa, "On the Recent Difference Schemes for the Three-Dimensional Euler Equations," in Proceedings of AIAA Eighth Computational Fluid Dynamics Conference, Honolulu, Hawaii, 1987, AIAA Paper No.87-1151.

35. J.L. Thomas and R.W. Walters, "Upwind Relaxation Algorithms for the Navier-Stokes Equations," AIAA Paper No.85-1501.

36. J.F. Thompson, C.F. Frank and C.W. Mastin, "Automatic Numerical Generation of Body-Fitted Curvilinear Coordinate System for Field Containing any Number of Arbitrary Two-Dimensional Bodies," *J. Comput. Phys.* **15**, 299 (1974).

37. B. van Leer, J.L. Thomas, P.L. Roe and R.W. Newsome, "A Comparison of Numerical Flux Formulas for the Euler and Navier-Stokes Equations," AIAA Paper No.87-1104.

38. B. van Leer, "Towards the Ultimate Conservative Difference Scheme II. Monotonicity and Conservation Combined in a Second-Order Scheme," *J. Comput. Phys.* **14**, 361 (1974).

39. B. van Leer, "Towards the Ultimate Conservative Difference Scheme IV. A New Approach of Numerical Convection," *J. Comput. Phys.* **23**, 276 (1977).

40. B. van Leer, "Flux-vector Splitting for the Euler Equations," *Lecture Notes in Physics*, vol. 170, p.507.

41. M. Vinokur, "An Analysis of Finite-Difference and Finite-Volume Formulation of Conservation Laws," *J. Comput. Phys.* **81**, 1 (1989).

42. J.C.T. Wang and G.F. Widhopf, "A High-Resolution TVD Finite Volume

Scheme for the Euler Equations in Conservation Form," *J. Comput. Phys.* **84**, 145 (1989).

43. Z.J. Wang and B.E. Richards, "High Resolution Schemes for Steady Flow Computation," to appear in *J. Comput. Phys.*, 1990.

44. Z.J. Wang and B.E. Richards, "High Resolution Schemes for Steady Inviscid and Viscous Flow," in Proceedings of the International Conference on Numerical Methods in Engineering: Theory and Applications, Swansea, January 1990.

45. Z.J. Wang and B.E. Richards, "High Resolution Schemes for Hypersonic Flow," in Proceedings, Workshop on Hypersonic Flows for Reentry Problems, Antibes (France), January 1990.

46. T.C. Wey and C.P. Li, "Comparison of Flux-vector and Flux-difference Splitting techniques for Hypersonic Flow," AIAA Paper No.88-3648.

47. H.C. Yee, "Construction of Explicit and Implicit Symmetric TVD Schemes and Their Applications," *J. Comput. Phys.* **68**, 151 (1987).

48. H.C. Yee, R.F. Warming, and A. Harten, "Implicit Total Variation Diminishing (TVD) Schemes for Steady-State Calculations," *J. Comput. Phys.* **57**, 327 (1985).

49. H.C. Yee, "Upwind and Symmetric Shock-Capturing Schemes," NASA Technical Memorandum 89464, May 1987.

BIBLIOGRAPHY

D.A. Anderson, J.C. Tannehill and R.H. Pletcher, Computational Fluid Dynamics and Heat Transfer, Hemisphere Publishing Corporation, U.S.A., 1984.

R.N. Cox and L.F. Crabtree, Elements of Hypersonic Aerodynamics, Academic Press Inc., New York, 1965.

D.C. Jiang, "Prediction of Shock/Turbulent Boundary Layer Separated

Flows Using the Navier-Stokes Equations," Ph.D. thesis, Department of Aerospace Engineering, University of Glasgow, 1986.

N. Qin, "Towards Numerical Simulation of Hypersonic Flow around Space-Plane Shapes," Ph.D. thesis, Department of Aerospace Engineering, University of Glasgow, 1987.

A. Rizzi and B. Engquist, "Selected Topics in the Theory and Practice of Computation Fluid Dynamics," *J. Comput. Phys.* **72**, 1 (1987).

G.A. Sod, Numerical Methods in Fluid Dynamics, the Press Syndicate of the University of Cambridge, Cambridge, 1985.

GLASGOW UNIVERSITY LIBRARY